Univerzita Karlova v Praze
Matematicko-fyzikální fakulta

DIPLOMOVÁ PRÁCE

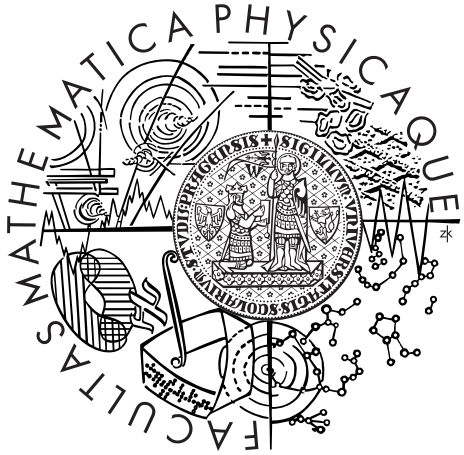

Lukáš Beran

Studium fyzikálních vlastností Heuslerových slitin

Fyzikální ústav Univerzity Karlovy

Vedoucí diplomové práce: RNDr. Martin Veis, Ph. D.
Studijní program: Fyzika
Studijní obor: Optika a Optoelektronika

Praha 2015

Charles University in Prague
Faculty of Mathematics and Physics

MASTER THESIS

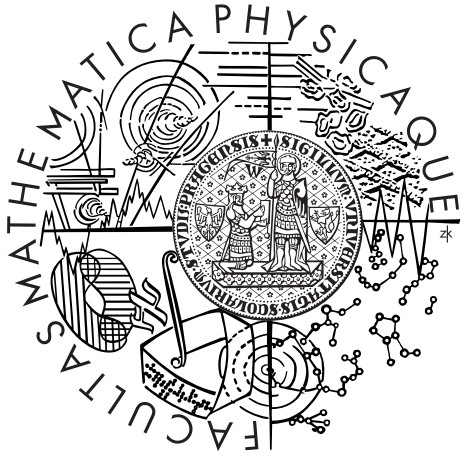

Lukáš Beran

Study of physical properties of Heusler alloys

Institute of Physics of Charles University

Supervisor of the master thesis: RNDr. Martin Veis, Ph. D.
Study programme: Physics
Specialization: Optics and Opto-electronics

Prague 2015

Dedication.

First and foremost I would like to give thanks to my supervisor RNDr. Martin Veis, Ph.D. for all of his help and leadership, not only during the work on my thesis, but for the support he has given me for my entire stay at Charles University.

I would also like to take the time to thank all those who helped make this work possible, namely P. Cejpek, who helped me with structure analysis and X-ray measurements, O. Heczko who provided samples, VSM measurements and invaluable advice, as well as, J. Hamrle who prepared samples and D. Legut for *ab initio* calculations.

I also have to thank Aj and Max for their ever lasting friendship and support they have given me for many years. And last but not least I cannot thank my family and girlfriend Lucie enough for their never-ending support and understanding.

I declare that I carried out this master thesis independently, and only with the cited sources, literature and other professional sources.

I understand that my work relates to the rights and obligations under the Act No. 121/2000 Coll., the Copyright Act, as amended, in particular the fact that the Charles University in Prague has the right to conclude a license agreement on the use of this work as a school work pursuant to Section 60 paragraph 1 of the Copyright Act.

In ..... date ..... signature of the author

Název práce: Studium fyzikálních vlastností Heuslerových slitin

Autor: Lukáš Beran

Katedra: Fyzikální ústav UK

Vedoucí diplomové práce: RNDr. Martin Veis, Ph. D., Fyzikální ústav UK

Abstrakt: Diplomová práce je věnována systematickému studiu strukturních transformací Heuslerových slitin pomocí spektroskopické elipsometrie a magnetooptické speltroskopie. Strukturní transformace v těchto slitinách jsou vyvolány rozdílnými mikroskopickými mechanismy. Experimentální data získaná v této práci byla konfrontována s výsledky teoretických modelů. To umožnilo diskutovat získané výsledky a navrhnout jejich vysvětlení. V případě slitin Co-Fe-Si byla pozorována změna optických i magneooptických vlastností v závislosti koncetraci železa. Toto bylo vysvětleno zmenšováním zakázaného pásu minoritních spinů se vzrůstajícím podílem Fe. Teplotní závislost optických a magnetooptických vlastností slitiny Ni-Mn-Ga jasně prokázala existenci tzv. Martensitické transformace z kubické do tetragonální fáze. Studium slitin Rh-Mn-Co-Sn neprokázalo jasnou závislost fyzikálních vlastností na koncetraci Rh a Mn. To bylo vysvětleno značným pnutím ve vzorcích, které zkreslilo měřená data.

Klíčová slova: Heuslerova slitina, spektroskopická elipsometrie, magnetooptická spektroskopie

Title: Study of physical properties of Heusler alloys

Author: Lukáš Beran

Department: Institute of Physics of Charles University

Supervisor: RNDr. Martin Veis, Ph. D., Institute of Physics of Charles University

Abstract: This diploma thesis is devoted to systematic study of structural transformations of Heusler alloys by means of spectroscopic ellipsometry and magneto-optical spectroscopy. Structural transformations in these alloys are induced by different microscopic mechanisms. Obtained experimental results were confronted with theoretical calculations. This allowed the discussion of obtained results and suggestion of their interpretation. In the case of Co-Fe-Si alloys, changes in optical and magneto-optical properties with change of Co-Fe ratio were observer. This was explained by lowering of the gap for minority spins with increasing Fe concentrations. Temperature dependent optical and magneto-optical properties of Ni-Mn-Ga alloy showed the presence of so-called Martensitic transformation from cubic to tetragonal phase. A study of Mn-Rh-Co-Sn alloys did not show a clear dependence of physical properties upon the concentration of Rh and Mn. This was explained by strong strain inside the samples, which distorted obtained results.

Keywords: Heusler alloys, spectroscopic ellipsometry, magneto-optical spectroscopy

Contents

Introduction

The aim of this thesis is devoted to systematic experimental studies of structural transformations in various Heusler alloys by combination of spectroscopic ellipsometry and magneto-optical spectroscopy. Heusler alloys are exceptionally tunable materials which structural, magnetic, electronic and optical properties are strongly coupled. Their structure can be modified by change of the composition or temperature, which results in visible changes in their physical properties. Since they are suitable candidates for applications in novel spintronic, thermoelectrical or electronic devices, systematic studies of structural transformations in various Heusler alloys are required to optimize their physical properties for certain applications. Magneto-optical methods are widely used to sense magnetic properties of materials down to nanometer scale. Moreover, the spectral dependence of magneto-optical effects can be used to get important information about electronic structure of the material in magnetic field. Combined with spectroscopic ellipsometry, magneto-optical spectroscopy can provide spectral dependence of permittivity tensor of studied material. The spectra of particular tensor elements carry are directly related to electronic transitions in matter. Systematic magneto-optical studies of Heusler alloys undergoing structural transformations can therefore provide missing information, which cannot be obtained by another conventionally used characterization techniques.

This thesis is divided into seven chapters with corresponding sections. In the first chapter a brief introduction into the physics of Heusler alloys is given. Different physical properties and their changes with structure of these alloys are described.

The second chapter is devoted to the description of the light interaction with matter. Optical properties of matter are described within the framework of permittivity tensor and different phenomenological models describing its spectral dependence and originating from different microscopic mechanisms are introduced. At the end of this chapter a polarization of light is briefly explained and magneto-optical quantities are defined.

Mathematical apparatus, which is necessary for the description of light polarization changes after the propagation through optical systems or interaction with samples, is established in the third chapter. Fourth and fifth chapter are describing the theory of light propagation in optically anisotropic magnetic multilayers. This theory is necessary for theoretical calculations, which are confronted with experimental results. Experimental apparatuses of magneto-optical spectroscopy and spectroscopic ellipsometry, which were used to get experimental data presented in this thesis, are described in detail in chapter six.

Chapter seven presents all obtained results of this thesis. The results were obtained on three different Heusler alloys, namely Co-Fe-Si, Ni-Mn-Ga, and Rh-Mn-Co-Sn. Each of these alloys undergoes a structural transformation induced by different mechanism. Experimental data are confronted with theoretical calculations and the result is discussed in context of electronic structure and magnetic properties of studied material. A picture of changes in electronic structure due to the transformation is suggested.

Finally, the results of this thesis are concluded in Conclusions.

1. Heusler alloys

The First Heusler alloy was discovered in 1903 by German chemist Friedrich Heusler. It was an alloy consisting of Cu, Mn and Al. This alloy was ferromagnetic despite that none of its components are magnetic[1]. It was discovered later, that not only this alloy, but also a whole collection of similar alloys have the same behaviour. Nowadays, there are over a thousand known Heusler alloys. These materials with 1:1:1 or 2:1:1 stoichiometry are formed from various combinations of elements. Elements forming Heulser alloys are shown in Fig. 1.1.

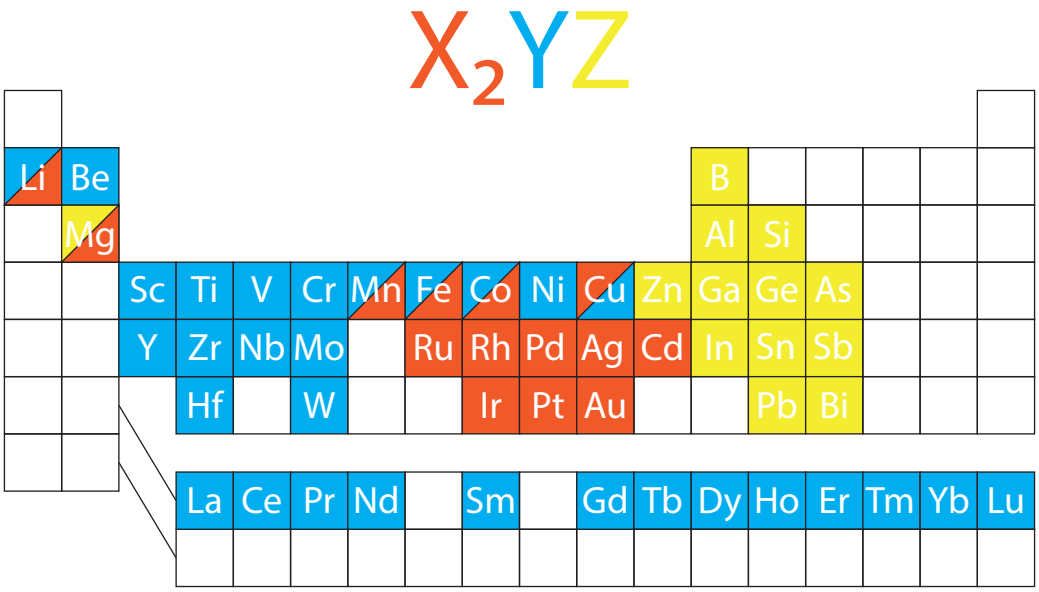

Figure 1.1: Elements forming Heusler alloys.

The origin of ferromagnetic behaviour was unexplained for a relatively long time. In 1929 X-ray measurements revealed that the elements of Cu_2MnAl are ordered in an fcc super lattice. In the mean time many other alloys with room temperature ferromagnetic behaviour were reported. Deeper structure investigations revealed that Heusler alloys are formed from two ordered binary B2 compounds XY and XZ. Both compounds may have CsCl crystal structure (for an instance CoMn and CoAl yield Co_2MnAl). That reveals possibility of forming a new Heusler alloy if B2 structure exists. It was also discovered, that one of four sublattices can be unoccupied. These alloys are so-called Half- or Semi-Heuslers. Afterwards studies revealed, that most of the Heusler alloys behave ferromagnetic in stoichiometric composition. Crystal structure, composition and heat treatment are the most significant aspects, that determine magnetic properties of the alloy. Another very interesting effect that was observed is magnetoelasticity of Ni_2MnGa. In summary Heusler alloys have both experimental and theoretical interest due to their well defined structure and ability to design their physical properties just by using proper elements and stoichiometry.

Very simple picture of Heusler alloy properties can be predicted by number of their valence electrons[2]. For example, superconductivity was observed in alloys with 27 valence electrons, which were also non-magnetic. Heusler alloys do not have to be only metals, but also over 250 semiconducting compounds were

reported[3]. A band gap ranging from 0 eV to 4 eV can be obtained simply by changing their chemical composition. There is also possibility to obtain both p and n types for same element composition. Moreover, novel physical phenomena like topological edge states, superconductivity, half-metallic ferromagnetism, etc. were observed in this class of compounds[4, 5]. Most importantly, various combinations of these phenomena were also observed.

1.1 Structure

Heusler compounds are defined as ternary intermetallic compounds. At stoichiometric composition, Full-Heuslers (X_2YZ) and Half-Heuslers (XYZ) crystallize in $L2_1$ and C1b structure respectively. The unit cell contains four independent fcc sublattices with positions (0,0,0) and $(\frac{1}{2}, \frac{1}{2}, \frac{1}{2})$ for X, $(\frac{1}{4}, \frac{1}{4}, \frac{1}{4})$ for Y and $(\frac{3}{4}, \frac{3}{4}, \frac{3}{4})$ for Z atoms, where second of X sublattices is vacant in Half-Heuslers (Fig. 1.2). The X and Y atoms have a distinct cationic character, whereas Z can be seen as the anionic counterpart. The nomenclature in literature varies a lot and thus all three possible permutations can be found. However the most common is ordering by electronegativity.

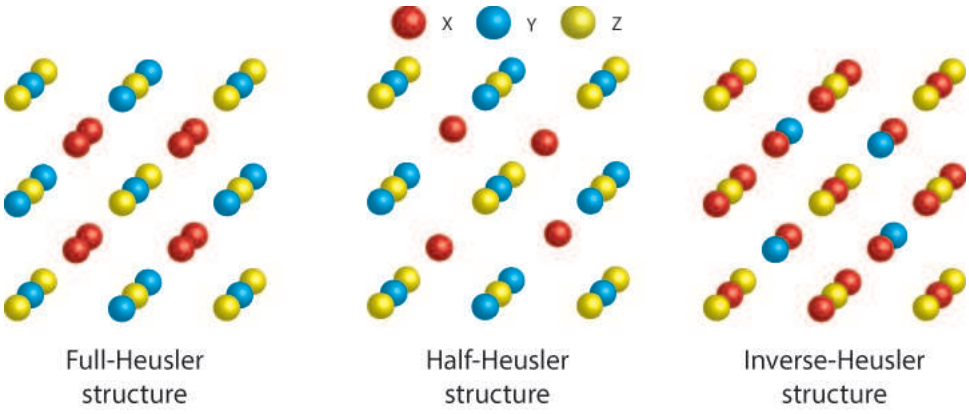

Figure 1.2: Structures of Heusler alloys.

We can imagine Half-Heusler structure as a ZnS-sublattice in which the octahedral sites are occupied. This description is favourable because of covalent bonding interaction between two of the contained elements, which plays major role in the electronic properties of the material. Some elements tend to form NaCl-type sublattice instead.

There are also reports of third type of Heusler structure[6]. This type is called Inverse-Heusler and occurs when atomic number of Y element is higher than the one of X from the same period. It can be formed occasionally when transition metals from different periods are involved. In all cases, the element X is more electropositive than Y. As with Full-Heuslers, XZ elements form a rock salt lattice to achieve an octahedral coordination for X. The remaining X and Y atoms fill the tetrahedral holes with fourfold symmetry. There are still four fcc sublattices, however the X atoms do not form a simple cubic lattice as before. More precise description of atomic positions can be found at [7, 8, 9]. Basic schemes of Heusler structures are shown in Fig. 1.2. The prototype of this structure is $CuHg_2Ti$.

This structure is also often observed at Mn_2-based compounds and at quaternary Heusler alloys (XY)X'Z.

1.2 Structural disorder

From description above, it is obvious that atomic arrangement is vital for properties of Heusler alloys. Therefore various lattice defects greatly influence physical attributes of final compound. On the other hand this phenomena can be also used to achieve various properties. High purity of alloys is also very important to obtain required properties. Only slight concentration of impurities can dramatically change electronic structure, which changes the behaviour of the alloy itself.

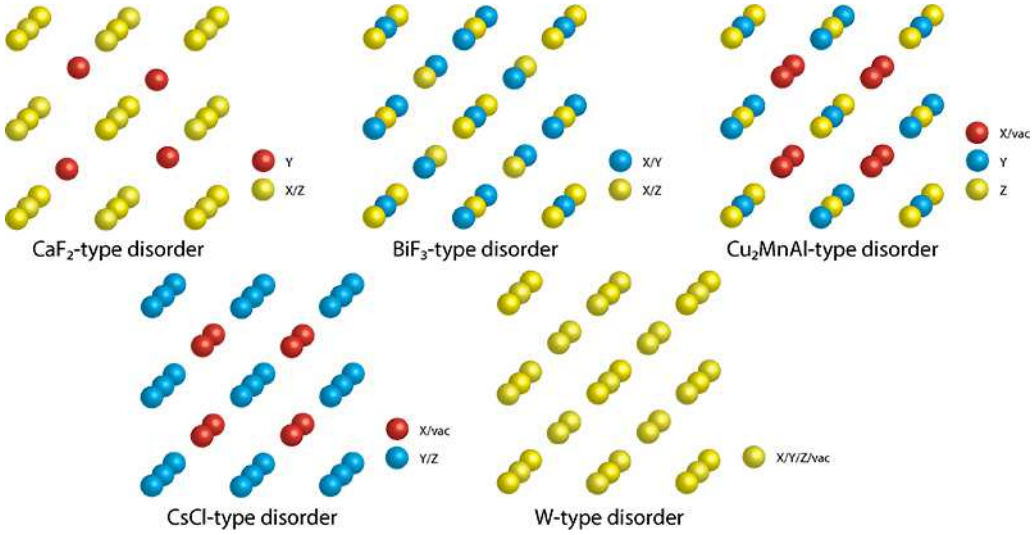

Figure 1.3: Types of disorder in Half-Heusler alloys.

Overview of possible Half-Heusler disorder types are shown in Fig. 1.3 and their detailed description can be found in [10]. We are mostly concerned about types of disorder, when atoms of different elements swap their positions between each other, because these effects cause change in electronic structure of the alloy. Amount of disorder has the highest influence on the size of the band gap. It was observed that band gap is closing with increasing amount of atomic disorder, and eventually closes completely. The easiest method to obtain amount of disorders in alloy is X-ray diffraction (XRD) and anomalous X-ray diffraction (AXRD). Some kinds of disorder can be observed as various reflections in powder XRD pattern.

In case of Full-Heuslers, disorder mostly affects magnetic and transport properties caused by change of spin stiffness[11]. Types of disorder for Full-Heusler alloys are depicted in Fig. 1.4.

Therefore it is vital to examine these disorders to be able to characterize exact properties of compound.

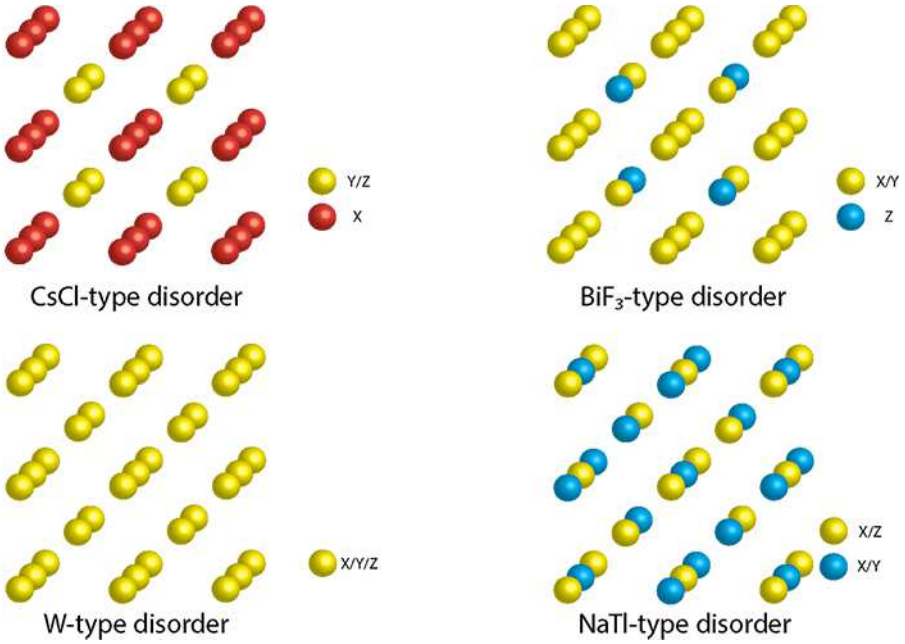

Figure 1.4: Types of disorder in Full-Heusler alloys.

1.3 Magnetic properties

Very interesting magnetic properties were observed in Heusler alloys. Even magnetic phenomena like localized magnetism, antiferromagnetism, helimagnetism, Pauli paramagnetism or heavy-fermionic behaviour were observed. Since a lot of magnetic Heusler alloys contain non-magnetic elements, great interest was paid to study the origin of their magnetism.

1.3.1 Ferromagnets

Most of Heusler alloys exhibit ferromagnetic behaviour. Particularly, in the case of Mn at Y positions alloys, there is usually magnetic moment of 4 μ_B observed. Despite their metallic character, these compounds have localized magnetic properties and therefore they are ideal for studies, how atomic disorder and electron densities affect magnetic properties. As was already mentioned above, the first reported magnetic Heusler alloy Cu_2MnAl contained non-magnetic elements. Other ferromagnetic alloys were for example MnNiSb and Co_2MnSn. Half-Heuslers contains only one magnetic lattice, which means that only eight atoms may carry magnetic moment. Situation in Full-Heuslers is much more complicated since X atoms sit in tetrahedral formation, which allows their magnetic interaction and formation of the second delocalized magnetic lattice.

The origin of ferromagnetism in Heusler alloys was unknown for a very long time. It was finally explained after the discovery of their electronic structure. In alloys containing Mn as Y element, it was observed that the magnetic moment is localized around Mn atoms. That comes from the fact, that the large exchange splitting of the Mn d states implies, that Mn atom's d states support only one spin direction. In the ferromagnetic state the spin-up d electrons of the Mn atom hybridize with those of the X atoms forming a common d band, but spin-down d electrons are almost completely excluded from the Mn sites. This phenomenon

can be well observed in calculated density of states (DOS) of Co_2MnAl shown in Fig. 1.5. It was proposed by Kübler et al.[12] that in Full-Heusler alloys, X atoms primary determine the lattice constant, while Z atoms mediate the interaction between the Mn *d* state. However, experiments demonstrated that both X and Z atoms play similar role in establishing the magnetic properties.

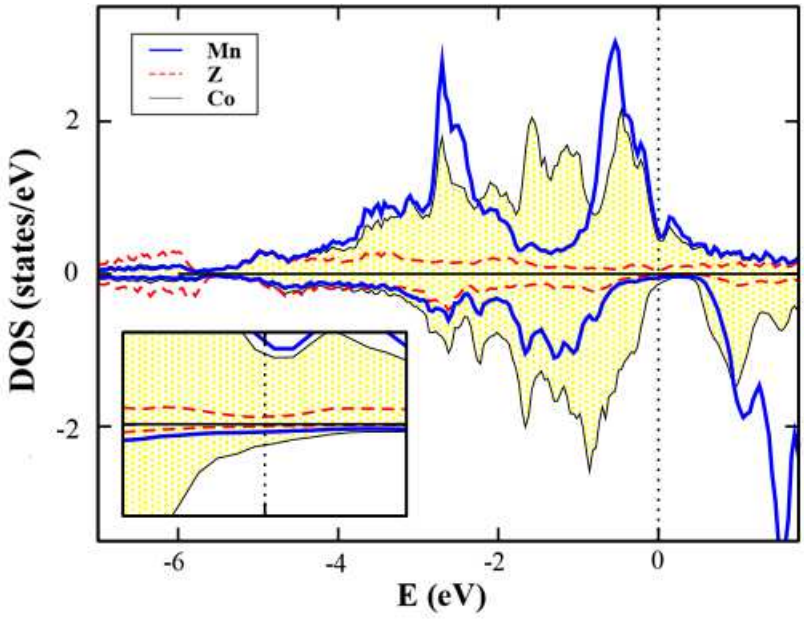

Figure 1.5: Calculated DOS of Co_2MnAl alloy[13].

1.4 Half-metallic ferromagnetism

A route of Half-metallic ferromagnetism (HMF) began with studies of MnPtSn in 80s of the last century due to fast development in the area of fast non-volatile mass storage memory devices in the field of magneto-optics. This compound showed magneto-optical Kerr rotation of 1.27° with Curie temperature above room temperature. This result motivated the investigation of the electronic structures of isoelectronic Heusler compounds MnNiSb, MnPdSb and MnPtSb, which led to the prediction of MnNiSb as the first material being a half-metallic ferromagnet. These results were first published by Groot and coworkers [14, 18] and confirmed by many other authors [19, 20, 21].

Positron-annihilation experiments and inverse photoemission confirmed 100% spin polarization for bulk MnNiSb. Unfortunately surface properties are usually different from bulk due to impurities and manganese segregations in combination with high affinity to oxygen. These observations undergo the importance of the crystal structure with respect to its properties. This is most significant in case of thin films, because there is usually strain induced by the lattice mismatch. This can also cause a large disagreement of experimental data with theoretical calculations.

The explanation of the half-metallic ferromagnetism was introduced on the basis of the band structure calculations of NiMnSb and PtMnSb Half-Heusler compounds by Groot et al.[14]. In these alloys, band structure for each spin

is qualitatively different. Major spin band is metallic, whereas the Fermi level falls into the gap of the minor spin band (Fig 1.6). Co_2MnZ, (Z=Si, Ge) were reported by Ishida et al. to have such behaviour[15]. Since then, a number of further systems were predicted to be half-metallic. Some of them are binary magnetic oxides (CrO_2), colossal megnetoresistance materials (LSMO) and zinc-blende compounds MnAs and CrAs.

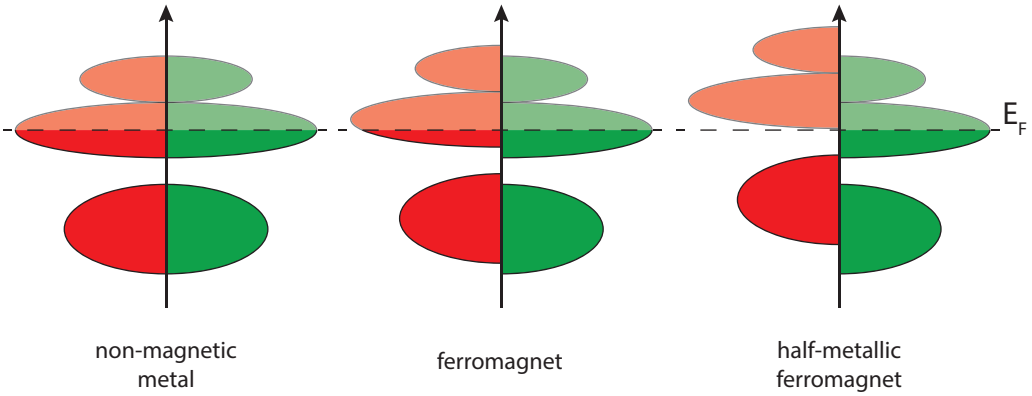

Figure 1.6: Scheme of DOSs of materials with different magnetic properties.

Formally, the complete spin polarization of charge carriers in a HMF materials is only reached in the limiting case of zero temperature and vanishing spin-orbit interaction. Heusler alloys usually contain *3d* elements which do not show spin-orbit coupling[16]. Presence of spin-orbit coupling allows transitions between up and down spins, which breaks half-metallicity. Therefore they are great candidates to exhibit half-metallic ferromagnetism.

1.4.1 Origin of the half-metallic gap

The origin of this phenomenon is strictly connected to symmetry of the system. In case of Half-Heusler alloys, it comes from vacant site at the position $(\frac{1}{2}\frac{1}{2}\frac{1}{2})$ that reduces its cubic $L2_1$ structure to $C1_b$ tetrahedral crystal structure. Thus the gap originates from the strong hybridization between d states of the higher valent and the lower valent transition metal atoms. If we look at example alloy with Mn at Y position, Z atoms are six nearest neighbours of every Mn atom. An interaction between Mn p orbitals of Z atoms results in the splitting of Mn-*3d* states into a lower lying triplet of t_{2g} states and a higher laying doublet of e_g states. In the majority band the Mn *3d* states are shifted to lower energies and form a common *3d* band with X *3d* states, while in the minority band the Mn *3d* states are shifted to higher energies and are unoccupied. The results in the gap splitting at Fermi energy separating occupied d bonding states from unoccupied d antibonding states(see Fig. 1.7).

1.4.2 Full-Heusler HMF

Shortly after the discovery of MnNiSb, another group of compounds showing HMF was found. First representatives were predicted from *ab initio* calculations by Kübler et al.[19]. Density of states of ferromagnetic Co_2MnSn and Co_2MnAl nearly vanishes for one spin orientation at the Fermi energy resulting in high

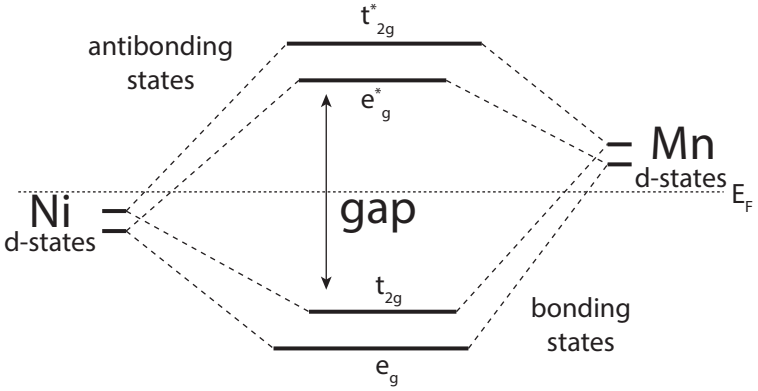

Figure 1.7: The formation of molecular orbitals between d states of Ni and Mn.

spin polarization. Afterwards, many Co_2-based Heusler compounds with HMF behaviour were found. First compound that was successfully applied in spintronics was $Co_2Cr_{0.6}Fe_{0.4}Al$ (CCFA)[17]. The idea behind this material was the combination of a large band gap in the minority DOS with large DOS (van Hove singularity) in the majority states. The appearance of van Hove singularity at or close to the Fermi energy is an important requirement for a stable half-metallic ferromagnet insensitive to the disorder. Band structure calculations revealed, that to obtain the Fermi energy right in the middle of minority band, there has to be 27.8 or 28.5 valence electrons. That gives us half-metallic ferromagnetism stable against temperature fluctuations. Such non-integer value can be achieved by quaternary alloys of the type $Co_2Y_{1-x}Y'_xZ$ or $Co_2YZ_{1-x}Z'_x$.

After rather disappointing results in the era of giant magnetoresistance (GMR) multilayers, CCFA brought great interest to study of Heusler alloys. CCFA was also successfully applied in tunnelling magnetoresistance (TMR) devices. Further attempts to grow thin layers of CCFA were rather unsuccessful. Films showed decrease of magnetic moment and high presence of disorder. Especially in Cr-Al-containing compounds is their sensitivity against oxygen what triggers disorder and phase separation effects.

In the search for higher magnetic moment, it was discovered that Co_2CrAl is a half-metallic ferromagnet with magnetic moment of 3 μ_B. However, the substitution of chrome to iron results in a loss of HMF for higher concentrations of chrome. Such behaviour was explained by the shift of Van Hove singularity relative to the Fermi energy.

Although the family of X_2YZ Heusler compounds is very large, there are only few compounds exhibiting half-metallic ferromagnetism, that are not based on cobalt as X element. Therefore Co and Mn based compounds are mostly investigated, especially due to their high Curie temperatures.

Heusler compound with the highest magnetic moment found so far is Co_2FeSi with magnetic moment of 6 μ_B. Therefore this compound was further investigated. There were attempts to enhance its properties by including Mn. All $Co_2Mn_{1-x}Fe_xSi$ exhibit half-metallic ferromagnetic behaviour. Many theoretical calculations were done on this series to further explain the origin of HMF [22, 23].

1.5 Other magnetic behaviours

Antiferromagnetic ordering exists in some of Heusler alloys, particularly in the ones, where *3d* magnetic moment is carried only by Y atoms (mostly Mn). Antiferromagnetic behaviour was more frequently observed at Full-Heuslers than at Half-Heuslers. It is particularly due to larger distances between Mn atoms, which allow X and Z elements to shield their interactions.

Ferrimagnetic behaviour is very rare in Heusler alloys. For example, it was observed in CoMnSb[24].

1.6 Magneto-optical effects in Heusler compounds

A very important aspect of Heusler compounds is their magento-optical (MO) behaviour. That means various changes in the polarization state of light upon the interaction with material possessing a net magnetic moment, mainly rotation of linear polarization (Faraday, Kerr rotation) and the complementary differential absorption of left and right circularly polarized light (molecular circular dichroism - MCD). There are also several studies of MO effects quadratic in magnetization[14, 25].

Huge magneto-optical effect was observed on MnPtSb and MnNiSb alloys, where measured MO Kerr Rotation achieved the value of -1.27 ° at RT and 5° at 80K. Therefore it was called "giant".

However its explanation was not that easy. There were several models proposed, mostly including change of half-metallic character due to spin-orbital interaction or semi-relativistic effects. As before, the final explanation came from electronic structures of these alloys. Antonov et al. found and explained anomalies in Kerr spectra of MnNiSb and MnPtSb that appeared as energy shifts caused by spin-orbital interaction[26, 27]. Among others, some Full-Heusler alloys were also reported to have huge magneto-optical effect. For example Co_2FeAl and Co_2FeGa.

Another interesting study of magneto-optical properties of Heusler alloys were done by Kumar et al.[28]. They observed change of Kerr spectra caused by impurities and dislocations in their compounds.

1.7 Martensitic transformation

It was observed, that some of Heusler alloys undergo martensitic transformation from high-symmetry austensite cubic phase to low-symmetry martensite orthogonal phase. In magnetic alloys, there was also magnetoelastic effect observed in the martensite state. This effect is also called magnetic shape memory effect (MSM). This especially occurs when Mn is present as Y element. In these alloys, external magnetic field induce strain, which may eventually result in a swapping of direction of magnetization easy axis. That causes up to 12% reversal deformation of crystal. In despite of intensive research, it is not quite explained, what mechanism is behind this transformation. The transformation is often accompanied by gradual softening of acoustic phonon branch. This softening is most likely related to nesting of Fermi surface. On the other hand, some observa-

tions lead to conclusion that transformation is related to band Jahn-Teller effect and the martensitic transformation is stabilized by ferromagnetic interaction. For details about martensitic transformation see [29].

1.8 Heusler alloys spintronic applications

It is not that long ago when applications of novel spintonic concepts in consumer electronics was unthinkable. However after the discovery of GMR effect in magnetic multilayers by Fert and Grünberg, no one doubted that this situation is going to change. Nowadays, spintronic devices are part of the daily life.

1.8.1 Magnetoresistive devices

First spintronic magnetoresistive devices were based on GMR effect. GMR effect was observed on spin valve (two magnetic layers sandwich with very thin non-magnetic metallic spacer). In the case of parallel magnetization alignment of both magnetic layers, the resistance of the device is low, whereas a high resistance state is present, if the alignment is antiparallel. One of the most common GMR structure is Fe-Cr-Fe system[30]. In magnetoresistive reading head, magnetization of the first layer is pinned by anti-ferromagnetic neighbouring layer and the second ferromagnetic layer is used to read the magnetization direction from nearby domain. That allowed reading data from magnetic media with much smaller domains than before. This led to dramatic increase of data storage density. Later, GMR structures were overcome by tunnelling magnetoresistance devices. These devices use dielectric spacer instead of metallic one. Therefore electrons have to tunnel between the layers and the structure becomes more sensitive to much smaller magnetic fields. A scheme of such structure is displayed in Fig. 1.8. Especially Co_2-based Heusler alloys were used in development in this area[31]. An efficiency of TMR device is described by TMR ratio of a junction defined as

$$\frac{\Delta R}{R_{TMR}} = \frac{2P_1P_2}{1 + P_1P_2}, \tag{1.1}$$

where P_1 and P_2 are polarizations of the first and the second electrodes respectively. Spin polarization is defined via

$$P = \frac{N_\uparrow - N_\downarrow}{N_\uparrow + N_\downarrow}, \tag{1.2}$$

where $N_\downarrow$ and $N_\uparrow$ are densities of the majority and the minority electrons at the Fermi energy level. The highest TMR 1800% ratio measured by Fert et al.[32] corresponds to an electrode spin polarisation of at least 95%, but unfortunately only at 4K. These values were measured on tunnel junction with manganite electrode. That is why prediction of half-ferromagnetic MnNiSb stimulated great research interest, aiming at the utilization of Heusler compounds in magnetic tunnel junctions (MTJs). Despite almost 100% spin polarization on bulk sample, layered structure showed only values about 60% at 1.6 K. First integrated epitaxial MnNiSb thin film in MTJ yielded a low TRM effect of 9% at RT and 18% at 4.2 K, which corresponds to only 25% spin polarization. These low values

were explained by presence of atomic disorder. Therefore more advanced growth methods such as molecular beam epitaxy (MBE) has to be used to obtain high quality films. Discovery of CCFA led to huge improvements of TMR ratios. For example TMR ratio of nearly 600% was observed in Co_2MnSi with an AlO_x tunnel barrier at low temperature[33]. However this compound still exhibited strong temperature dependence. Breakthrough at this problematic came with discovery of Co_2FeSi, the half-metallic Heusler compound with the highest magnetic moment and Curie temperature of 1100 K. These properties were even enhanced by doping with Al or Mn. Many other alloys were studied and research in this area is still going on. Lately, huge improvement was also obtained by using of MgO tunnelling barriers instead of AlO_x ones[34, 35].

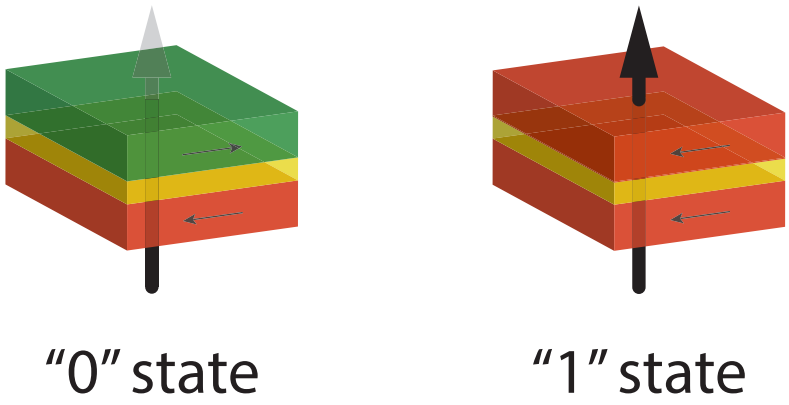

Figure 1.8: Scheme of TMR structure.

In addition to TMR device, current-perpendicular-to-plane (cpp) GMR devices with Heusler electrodes recently emerged in the field of spintronics[36]. These devices have huge advantage in being insensitive to electronic state at the interfaces, where half-metallicity is often damaged. Another advantage is in spacer, which can be made from similar Heusler alloy, that causes considerably smaller disorder in grown films. It has been already demonstrated that ccp-GMR devices are compatible with ultra-high density storage media[37]. However, they are still not superior to TMR heads. From an applications point of view, a stable cpp-GMR effect $\geq 30\%$ at room temperature is perfectly suitable to manufacture high performance devices.

1.8.2 Spin torque devices

Phenomena employed in GMR and TMR devices can also be used in opposite way. That means, by spin-polarized electric current, we can change the magnetic state of nanostructure. This so-called spin-transfer torque (STT) in one of the most promising phenomena today to satisfy an increasing demand for faster, smaller and non-volatile electronics.

This effect is possible due to the exchange interaction between the spin of the incoming conduction electrons and the spin of the electrons responsible for the local magnetization. A scheme of such device is shown in Fig. 1.9. First ferromagnetic layer with pinned magnetization is used to spin-polarize the current through the device. These spins may be repolarized into a new direction when

they encounter another ferromagnetic layer. In the current repolarization the local magnetic moment experiences a torque associated with the change in angular momentum that occurs due to the rotation of the electron spins. This STT can pump enough energy into nanomagnet to accomplish complete switch of magnetization.

From an applications point of view, thermal stability is crucial. Due to the decreasing of size of the device, superparamagnetic limit [38] is usually overcome by use of materials with the easy magnetization axis pointing perpendicular to the film surface (PMA). Low saturation magnetization as well as high spin polarization is also crucial for outcome of the device. One of the most studied materials in this area is $Mn_{3-x}Ga$. This material shows one of the highest PMA with spin polarization about 88% and Curie temperature higher than 770 K[39].

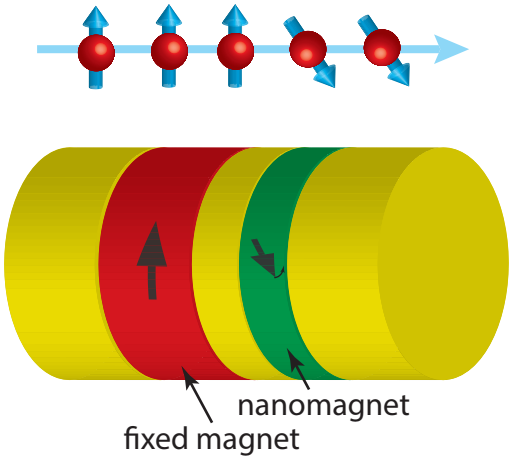

Figure 1.9: Scheme of STT device.

1.8.3 Spin injection

Another demand of spintronics is use of spin polarized current in different materials, which are unable polarize spins by themselves. That would allow many technological applications such as manipulation of classical information carried by spin, initialization, readout of a spin quibits and coherent manipulation of spin in the proposed spin field effect transistor. Such applications need injection of spin current especially into degenerate semiconductors like GaAs.

It had been already demonstrated, that it is possible to grow GaAs on Heusler alloys (Co_2MnGe)[40] with only small elongation of the lattice constant compared to the bulk value. The problem is with the interface between the semiconductor and ferromagnetic metal, because strong reduction of magnetic moment may occur there. Great improvement in this area was, once again achieved after the discovery of CCFA. Thin films of CCFA were grown on GaAs by MBE[41]. Studies of this interface showed that initial monolayers grow in A2-type structure, which causes loss of half-metallicity, because it allows formation of CrAl/As bondings[42].

One of the best values achieved so far were on Co-Mn-Ga alloy on InGaAs, which showed spin polarization in semiconductor about 13% at 5 K[43]. An injected spin polarization of 27% at 2 K was reported on the system Co_2MnGe/GaAs[44],

contrast to the value of 40% reached with a Fe injector.

1.8.4 Shape-memory materials

Ni_2MnGa is nowadays one of the most intensively investigated material owing to its shape memory behaviour. It has application potential in devices, in which strain states are controlled by the application of external magnetic field and vice versa. This material exhibits various structural transformations in wide temperature range, which highly depend on actual stoichiometry of alloy. From applications point of view, the most interesting one is the martensitic transformation. This is, as was mentioned above, structural transformation from high-symmetry austenite cubic phase to low-symmetry martensite phase. The martensite phase is mostly monoclinic, but due to small deviation it is usually referred as pseudo-tetragonal. The cubic unit cell is contracted along one direction (mostly c-axis) and extended along two other directions. Since this transformation is diffusionless, large stresses have to be stored and accommodated in the martensite microstructure. As consequence, the minimization of the strain energy leads to the formation of number of crystallographic domains, known as variants. In pure tetragonal case there are three variants that differ by direction of c-axis. A contact of two variants is called twin plane (see Fig. 1.10). In ferromagnetic shape memory alloys, such as Ni_2MnGa, a magnetic field can move these twin planes. Variants, in which the easy-axis of magnetization is aligned in parallel to the external field, grow preferentially at expense of variants with different orientation, resulting in macroscopic strains of up to 15%[45].

Presence of strong magnetoelastic coupling on the mesoscopic length-scale is essential to obtain good twin boundary motion in moderate magnetic fields (about 1 T). This is fulfilled in Ni-Mn-Ga shape memory alloys, in which the magnetocrystalline anisotropy energy and the magnetization are sufficiently high in the martensite phase. On microscopic length-scale strong magnetic coupling leads to large strains. Related alloys such as Ni-Mn-Sn and Ni-Mn-In showed lower saturation magnetization in austenite phase than in martensite phase. Therefore a magnetic field applied to the martensite phase can shift the transition to sufficiently low temperatures and stabilize the austenite phase, giving rise to a field induced reverse martensitic transformation (FIRMT)[46].

Another interesting feature is the tunability of both Curie temperatures (T_C) and temperature of martensitic transformation (T_M) by alloying in the Ni-Mn-Ga based system. It is possible to almost independently move temperature of martensitic transformation and Curie temperature. By that, we can obtain compound that perfectly fit our application's need. One can look at few examples with $Ni_{2+x}Mn_{1-x}Ga$. In small region around $x = 0.2$, T_M and T_C are really close to each other. That brings possibilities to induce additional properties like giant magnetocaloric effect, magnetostriction, and magnetoresistance, which are important for magnetic refrigeration or magnetostrictive transducers [47, 48]. If x increases over 0.3, T_M moves over T_C. That allows construction of high temperature shape memory alloys.

A ternary phase diagram of the Ni-Mn-Ga system was mapped to obtain proper relations between T_C and T_M [49]. That brought the finding, that lower percentage of Ga in alloy gives higher transformation temperatures. For example

$Ni_{43}Mn_{48}Ga_{10}$ has transformation well above room temperature at about 400 K.

Properties described above were obtained on monocrystals only. Such crystals also showed their full shape recovery about 10^8 mechanical cycles[50]. However polycrystalline samples lose all abilities connected with twin boundary movement due to boundaries of grains.

Additionally, few compositions show inverse magnetocaloric effect, which leads to cooling of the sample. However this effect was so far reported only in small magnetic fields and in higher fields samples exhibit standard magnetocaloric effect[48].

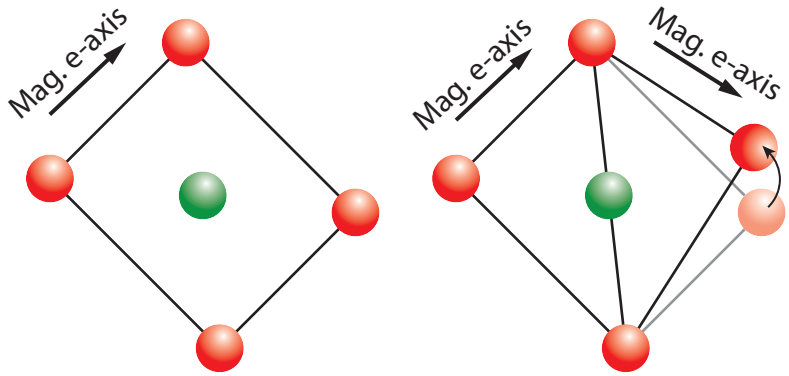

Figure 1.10: Scheme of twinning.

1.8.5 Other physical phenomena

We could continue with the list of interesting physical properties of various Heuler alloys for another fifty pages or even more. An interested reader can find more in proper literature [51]. We will end this chapter with just a short note that there are various, mostly ternary, compounds investigated for their superconducting or thermoelectric properties. Great discoveries were also achieved in the field of topological insulators, nanostructures and photovoltaics. Graphical overview of studied physical phenomena is shown in Fig. 1.11.

1.9 Outlook

We have shown there are many structural transformations occurring in Heusler alloys. These transformations are mostly connected with dramatic change of their physical properties. Therefore it is vital to study these transformations and understand the underlying physics. For the same reason it is really important to characterize amount of disorder in studied alloys. Magneto-optics is great tool for study of such transformations, because it is very sensitive to magnetism and a lot of information about electronic structure can be derived from its spectrally dependent measurements. Even more detailed pictures of the electronic structure can be obtained when it is combined with spectroscopic ellipsometry.

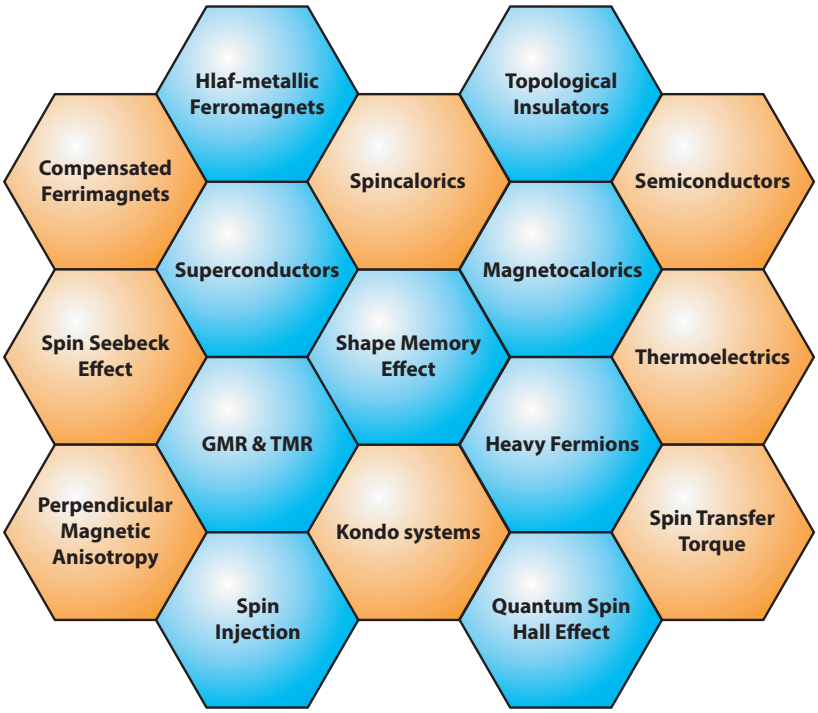

Figure 1.11: Overview of the different properties of Heusler compounds.

2. Description of light and matter

2.1 Tensor of permittivity

To introduce easy description of interaction of light with matter we start from Maxwell's equations.

$$\nabla \cdot \vec{D} = \rho, \tag{2.1}$$
$$\nabla \cdot \vec{B} = 0, \tag{2.2}$$
$$\nabla \times \vec{E} = -\frac{\partial \vec{B}}{\partial t}, \tag{2.3}$$
$$\nabla \times \vec{H} = \frac{\partial \vec{D}}{\partial t} + \vec{J}, \tag{2.4}$$

where $\vec{D} = \varepsilon_0 \vec{E} + \vec{P}$ and $\vec{H} = \frac{\vec{B}}{\mu_0} - \vec{M}$. One can see that whole interaction with matter is hidden in the vector of magnetization $\vec{M}$ and polarization $\vec{P}$. However this description is still quite complicated. Since we work with low intensities, we can consider only a linear response of material. Therefore we can write

$$\vec{D} = \varepsilon_0 \vec{E} + \hat{\chi}\vec{E} = \hat{\varepsilon}\vec{E}, \tag{2.5}$$
$$\vec{H} = \frac{\vec{B}}{\hat{\mu}}, \tag{2.6}$$

where we introduced tensors of permittivity $\hat{\varepsilon}$ and permeability $\hat{\mu}$. In magneto-optics we have to consider presence of magnetic field in our system. Its presence breaks symmetry of the system, therefore we must treat this system as anisotropic. In such situation we cannot separate permittivity into Cartesian components, but we have to deal with it in its full tensor form. To see sufficiency of this description in our cause, we can look at wave equation and write down its form for homogeneous linear medium without charge or current densities (derivation in [52])

$$\left(\Delta - \hat{\mu}\hat{\varepsilon}\frac{\partial}{\partial t}\right)\vec{E} = 0. \tag{2.7}$$

Here, one can see that the only parameter present in the equation is the term $\hat{\mu}\hat{\varepsilon}$. Since we work in area of optical frequencies we can assume that $\hat{\mu} = \mu_0$. In that case permittivity tensor fully describes the interaction of light with matter.

We mentioned above that we already consider linear homogeneous medium, so permittivity tensor is not function of time and space. Time invariation reduces number of independent components to six. Permittivity tensor in the matrix notation with use of this symmetry has the form

$$\hat{\varepsilon} = \begin{pmatrix} \varepsilon_{11} & \varepsilon_{12} & \varepsilon_{13} \\ -\varepsilon_{12} & \varepsilon_{22} & \varepsilon_{23} \\ -\varepsilon_{13} & -\varepsilon_{23} & \varepsilon_{33} \end{pmatrix}. \tag{2.8}$$

transverse	polar	longitudinal
$\begin{pmatrix} \varepsilon_1 & 0 & 0 \\ 0 & \varepsilon_1 & \varepsilon_4 \\ 0 & \varepsilon_4 & \varepsilon_1 \end{pmatrix}$	$\begin{pmatrix} \varepsilon_1 & \varepsilon_2 & 0 \\ \varepsilon_2 & \varepsilon_1 & 0 \\ 0 & 0 & \varepsilon_1 \end{pmatrix}$	$\begin{pmatrix} \varepsilon_1 & 0 & \varepsilon_3 \\ 0 & \varepsilon_1 & 0 \\ \varepsilon_3 & 0 & \varepsilon_1 \end{pmatrix}$

Table 2.1: Simplified form of the permittivity tensor for different magneto-optical configurations.

Since we consider only effects linear in magnetization, we can use approximation that all diagonal elements are the same. In that case we rewrite the permittivity tensor in form

$$\hat{\varepsilon} = \begin{pmatrix} \varepsilon_1 & \varepsilon_2 & \varepsilon_3 \\ \varepsilon_2 & \varepsilon_1 & \varepsilon_4 \\ \varepsilon_3 & \varepsilon_4 & \varepsilon_1 \end{pmatrix}. \tag{2.9}$$

That leaves us with just four independent components. If there is no magnetic field present, permittivity tensor reduces itself just to scalar variable. In our situation, we can write it as product of ε_1 and unit matrix. This parameter is usually obtained from ellipsometry. Off-diagonal elements are proportional to magnetization in the sample. In proper choice of coordinate system, each element depends only on one component of magnetization vector. We can use this property to obtain just one element during the measurement. Magneto-optical configurations where magnetic field vector is pointing along Cartesian axes are usually called polar, longitudinal and transverse. Their schemes are shown in Fig. 2.1. In these configurations permittivity tensor reduces to forms listed in table (2.1).

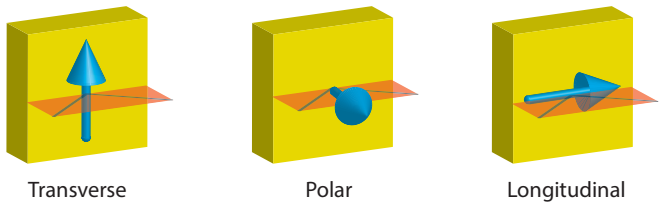

Figure 2.1: Schemes of magneto-optical configurations.

2.2 Phenomenological models

Spectral dependence of optical properties of matter raises from different microscopic mechanism which involve electronic transition, interactions with phonons, excitons, etc. In the first approximation one can use macroscopic phenomenological models.

2.2.1 Lorentz model

In Lorentz model, we start with basic classical concept of an atom, that contains a nucleus and one electron. Atomic nucleus is way heavier than electron,

therefore we can position the centre of our coordinate system into centre of it and neglect its movement. Interaction between these two bodies can be described by spring-like force. This assumption can be done when electron is at or near minima of potential. In that case only constant and linear term in the Taylor expansion of driving force in the equation of motion are relevant. The damping term comes from internal collisions in the solid and radiation emitted by electron. Light in this system is introduced via vector of its electric intensity. We will work with plane wave described by

$$\vec{E}(\omega, t) = \Re\{\vec{E}_0 e^{i\omega t}\}. \tag{2.10}$$

Electric field forces to displacing an electron in the atom and therefore induces a dipole momentum. This gives rise the macroscopic polarization, which is defined as

$$\vec{P} = -Nq\vec{y}, \tag{2.11}$$

where q is unit charge, N number of protons in atomic nucleus and $\vec{y}$ is displacement of electron form equilibrium. At last we define plasma frequency that will simplify further notations

$$\omega_p^2 = \frac{Nq^2}{m\varepsilon_0}. \tag{2.12}$$

All this substituted into the equation of motion yields

$$\frac{\mathrm{d}^2 P}{\mathrm{d}t^2} + \gamma \frac{\mathrm{d}P}{\mathrm{d}t} + \omega_0^2 P = \varepsilon_0 \omega_p^2 E, \tag{2.13}$$

where γ is parameter describing dumping of electron's motion. We can search solution of this equation in the form

$$P(\omega, t) = \Re\{P(\omega) e^{i\omega t}\}. \tag{2.14}$$

Inserting of this solution into equation (2.13) yields

$$P(\omega) = \frac{\varepsilon_0 \omega_p^2}{(\omega_0^2 - \omega^2) + i\gamma\omega} E_0. \tag{2.15}$$

If we compare this with material relation for macroscopic polarization

$$\vec{P} = \varepsilon_0 \left(\frac{\varepsilon_1}{\varepsilon_0} - 1 \right) \vec{E}_0, \tag{2.16}$$

we obtain the dependence of permittivity on the frequency of the electric field in form

$$\frac{\varepsilon_1}{\varepsilon_0} = \varepsilon_r = 1 + \frac{\omega_p^2}{(\omega_0^2 - \omega^2)} + i\omega\gamma. \tag{2.17}$$

As can bee seen from Eq. (2.17), ε_1 is a complex number. Therefore it is convenient to separate it into its real and imaginary parts via

$$\varepsilon_r = \Re\{\varepsilon_r\} - i\Im\{\varepsilon_r\}. \tag{2.18}$$

Frequency dependences of these terms can be written as

$$\Re\{\varepsilon_r(\omega)\} - 1 = \frac{\omega_p^2(\omega_0^2 - \omega^2)}{(\omega_0^2 - \omega^2)^2 + \omega^2\gamma^2}, \tag{2.19}$$

$$\Im\{\varepsilon_r(\omega)\} = \frac{\omega_p^2\gamma\omega}{(\omega_0^2 - \omega^2)^2 + \omega^2\gamma^2}. \tag{2.20}$$

One can see that frequency dependence of $\Im\{\varepsilon_r\}$ has Lorentzian shape. Both dependencies are displayed in Fig. 2.2.

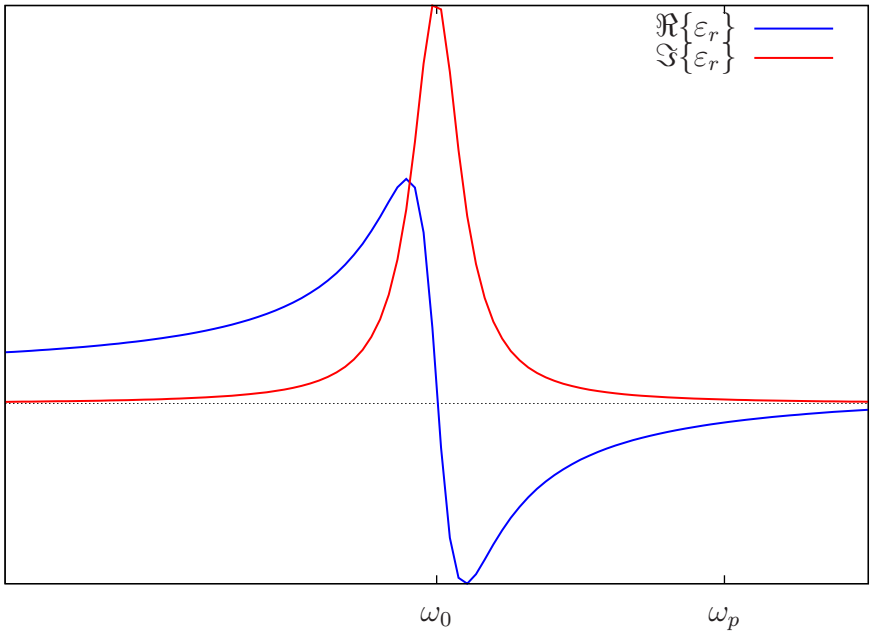

Figure 2.2: Spectral dependence of permittivity given by the Lorentz model.

2.2.2 Drude model

So far we considered electrons bounded to atomic nuclei. However in metals there are free electrons, whose interaction cannot be explained by the Lorentz model. For these, we need to use Drude model. The only change is in the spring-like force, which is in this case equal to zero. That means there is no bonding between nucleus and electron and electron can freely move through crystal. Nevertheless, there is still a damping term, mostly due to the collisions within the electron cloud and with nuclei.

Solution of alternated equation (2.13) gives

$$\varepsilon_r = 1 - \frac{\omega_p^2}{\omega^2 - i\omega\gamma}. \tag{2.21}$$

Spectral dependences of optical properties given by this model are displayed in Fig. 2.3.

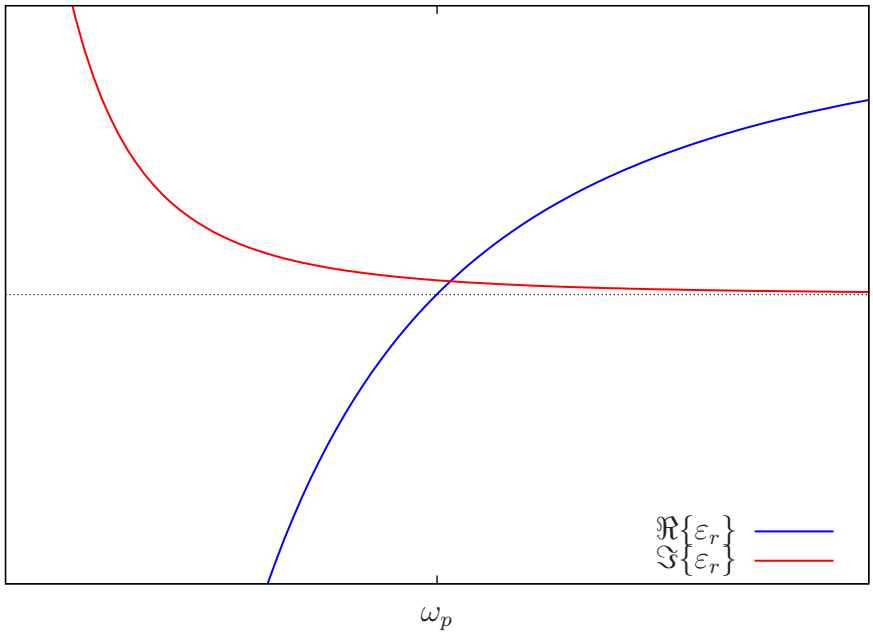

Figure 2.3: Spectral dependence of permittivity given by Drude model.

2.3 Polarization of light

A solution of the wave equation (2.7) can be written in form of plane wave

$$\vec{E} = \vec{E_0} e^{i(\omega t - \vec{k}\cdot\vec{r})}, \tag{2.22}$$

where ω is angular frequency and $\vec{k}$ is wave vector. Wave vector is defined as

$$\vec{k} = \vec{s} n \frac{2\pi}{\lambda}, \tag{2.23}$$

where $\vec{s}$ is a unit vector in the direction of propagation of light, λ is a wavelength and n is a refractive index. We could do the same for magnetic field, but since they are bound together, owing to the Maxwell's equations, by

$$\vec{B} = \frac{1}{c}(\vec{s} \times \vec{E}), \tag{2.24}$$

we can work only with electric field.

To simplify notation, we usually do not write the real part operator. Another option is to add complex conjugated term. One can see that the propagation of light can be fully described by its oscillating part and polarization. From now on, we will work with plane wave propagating along z axis. Therefore z component of the vector of electric field equals to zero. Therefore we can describe polarization by two component vector

$$\vec{E} = \begin{pmatrix} E_{0x} e^{i\phi_x} \\ E_{0y} e^{i\phi_y} \end{pmatrix} = \begin{pmatrix} E_{0x} \\ E_{0y} e^{i\Delta\phi} \end{pmatrix}, \tag{2.25}$$

where ϕ_x and ϕ_y are phases of x and y components of the vector of electric field respectively and $\Delta\phi$ is a phase shift defined as $\Delta\phi = \phi_y - \phi_x$. In second step

we moved the beginning of time which allowed us to add same phase to both components. Thanks to that we achieved form with only amplitudes of the field components and their phase shift. Now we can split this equation in two

$$E_x = E_{0x}, \tag{2.26}$$
$$E_y = E_{0y} e^{i\phi_y}. \tag{2.27}$$

Now we will skip few steps that contain subtracting, squaring and adding of these two equations[52] and move to product of these operations

$$\left(\frac{E_x}{E_{0x}}\right) + \left(\frac{E_y}{E_{0y}}\right) - 2\frac{E_x E_y}{E_{0x} E_{0y}} \cos\Delta\phi = \sin^2\Delta\phi. \tag{2.28}$$

This equation is also equation of ellipse. What is shows is that at any instant of time the locus of points described by the propagation of E_x and E_y will trace out ellipse. If we look at propagation through system, the end point of the electric field vector follows spiral trajectory, as it is shown in Fig. 2.4.

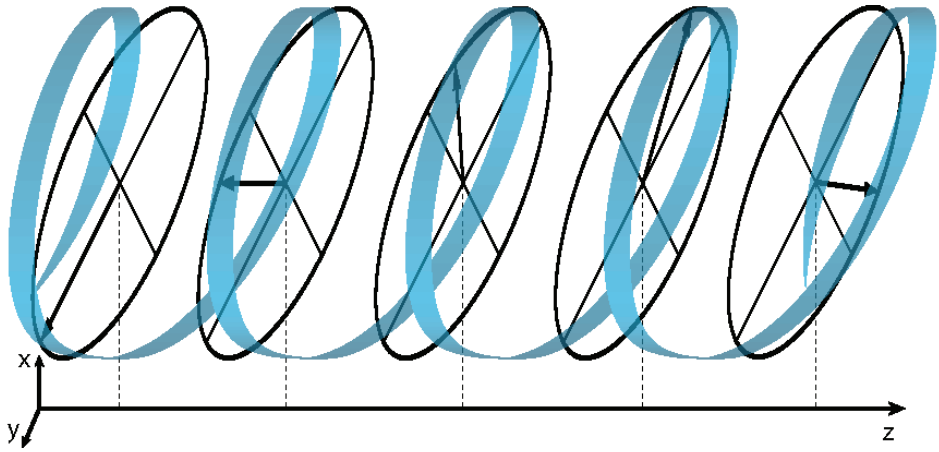

Figure 2.4: Trajectory of the electric field moving through space.

Therefore any polarization of light can be well described by an ellispe. The ellipse is parametrized by four parameters. Since we can free the time origin , we need only three parameters. The use of amplitudes and phase difference is not the most convenient one so we better use main semi-axis, azimuth ψ and ellipticity χ. Their definition is showed in Fig. 2.5. Intervals of parameters are

$$a \in [0, \infty], \tag{2.29}$$
$$\psi \in \left[-\frac{\pi}{2}, \frac{\pi}{2}\right], \tag{2.30}$$
$$\phi \in \left[-\frac{\pi}{2}, \frac{\pi}{2}\right], \tag{2.31}$$

and values of these parameters can be calculated via

$$\tan(2\psi) = 2\frac{E_{0x} E_{0y} \cos\Delta\phi}{E_{0x}^2 + E_{0y}^2}, \tag{2.32}$$
$$\tan(\phi) = \pm\frac{b}{a}. \tag{2.33}$$

The ellipticity can acquire also negative values, because it contains information about circularity of light. We choose notation, where negative values represent left-handed direction of rotation. A zero value represents linearly polarized light.

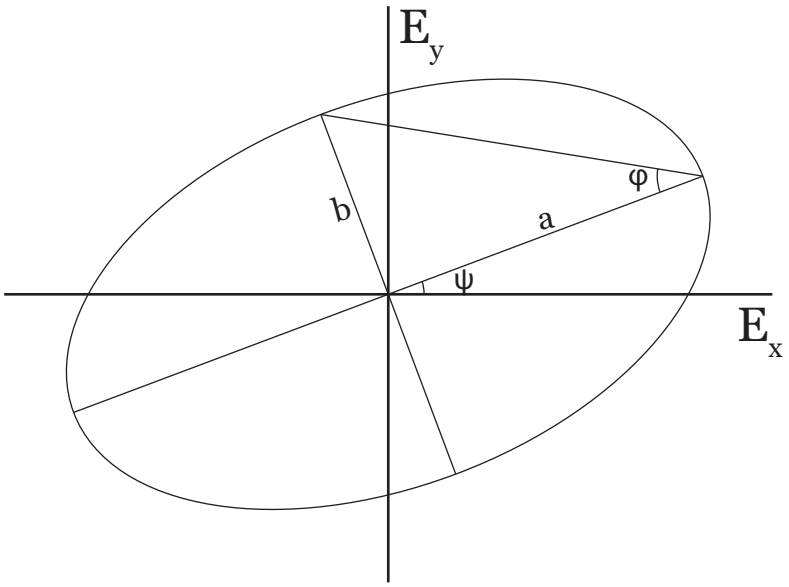

Figure 2.5: Definition of angles describing polarization of light.

Next significant situation is when $\Delta\phi$ is equal to $\pm\frac{\pi}{2}$ and $E_x = E_y$. In this case, the light is circularly polarized. The vector of electric field is making precession movement, while his end creates a circle in space. Depending on the sign of phase shift, we can have left-handed circularly polarized light (LHCP) or right-handed polarized light (RHCP). Any other option is generally called elliptic polarized light.

3. Mathematical apparatus

3.1 Jones formalism

For future description of optical and magneto-optical experiments, we have to introduce formalism that is used for description of light polarization and its changes during the propagation through optical systems. There are many formalisms available, but for our case, Jones formalism is sufficient and easy to use.

3.1.1 Jones vector

At the beginning, we have to define a Jones vector, that characterizes polarization we will be working with. We choose z direction as a direction of propagation. We start with vector of electric field

$$\vec{E} = \begin{pmatrix} E_x \\ E_y \end{pmatrix}, \tag{3.1}$$

where E_x and E_y are components of the electric field vector along Cartesian axes. If we consider the plane weve solution of the wave equation, we can rewrite this vector in the form

$$\vec{E} = \begin{pmatrix} E_{x0}(z)e^{i(\omega t - kz + \phi_x)} \\ E_{y0}(z)e^{i(\omega t - kz + \phi_y)} \end{pmatrix} = e^{i(\omega t - kz)} \begin{pmatrix} E_{x0}e^{i\phi_x} \\ E_{y0}e^{i\phi_y} \end{pmatrix}. \tag{3.2}$$

In the next step, we omit the oscillating factor, because it is same for both components. Since it has no influence on the polarization state that we are interested in, we will no further use it. It is also usual to normalize this vector. In the last step we will introduce a phase difference, which is defined as before as $\Delta\phi = \phi_y - \phi_x$ and in the meaning of previous treatments, we write Jones vector in the final form

$$J = \begin{pmatrix} E_{x0} \\ E_{y0}e^{i\Delta\phi} \end{pmatrix}, \tag{3.3}$$

which represents Jones vector in base of linearly polarized light in directions of coordinate axes. With this choice of base, it is easy to see, that linearly polarized light with plane of polarization parallel to x axis is described by Jones vector

$$J = \begin{pmatrix} 1 \\ 0 \end{pmatrix}. \tag{3.4}$$

Our second choice of base could be RHCP and LHCP light. We will not show the proof, that these states are orthogonal. In this base Jones vector of our linearly polarized light looks like

$$J = \frac{1}{\sqrt{2}} \begin{pmatrix} 1 \\ \pm 1 \end{pmatrix}, \tag{3.5}$$

depending on the order of chosen base vectors. Any two orthogonal polarization states can be used as a base. Transformation between these bases is bound by

standard operation of linear algebra, that are well described in [54]. We introduce only basic relation

$$J' = \mathbb{A}J, \tag{3.6}$$

where $\mathbb{A}$ is transfer matrix between bases. The most favourable base is usually the one made of eigenmodes of studied system, because matrix describing relation between the beginning and end states is diagonal.

3.1.2 Jones matrix

Now we need to describe the interaction of light with system. From linear algebra we know, that relation between two n-dimensional vectors is described by $n \times n$ matrix. In our case it is just 2×2 matrix which in general form can be written as

$$\mathbb{M} = \begin{pmatrix} A & B \\ C & D \end{pmatrix}, \tag{3.7}$$

where A, B, C and D are complex numbers. As with vectors, final form of matrix describing some optical element is bound to base, we are working in. We can obtain Jones matrix in new base via

$$\mathbb{M}' = \mathbb{A}\mathbb{M}\mathbb{A}^{-1}, \tag{3.8}$$

where $\mathbb{A}$ is transformation matrix between bases.

Now we can derive new Jones vector of light that propagates through the system described by Jones matrix $\mathbb{M}$ by using

$$J_f = \mathbb{M}J_i, \tag{3.9}$$

where J_i is initial and J_f final state.

List of the most important Jones matrices is listed in table (3.1). All of them are in bases of linearly and circularly polarized light.

Every element can also be easily rotated by rotating of its coordinate system. Transformation matrix for rotation by angle α is

$$\mathbb{R}(\alpha) = \begin{pmatrix} \cos\alpha & \sin\alpha \\ -\sin\alpha & \cos\alpha \end{pmatrix}, \tag{3.10}$$

and it works same way as transformation between bases mentioned above.

3.1.3 Propagation through optical element

Now with full formalism, we can look how to describe propagation of light through system that contains more of than just one optical element. We have shown, that propagation through system is described by equation (3.9). Now, we will work with the system that contains of n sub-systems with different optical properties, each of them described by his own Jones matrix $\mathbb{M}_i$. We can simply use equation (3.9), but matrix $\mathbb{M}$ needs to describe whole system. Such matrix

	linear base	circular base
polarizer at angle α	$\begin{pmatrix} \cos^2\alpha & \sin\alpha\cos\alpha \\ \sin\alpha\cos\alpha & \sin^2\alpha \end{pmatrix}$	$\frac{1}{2}\begin{pmatrix} 1 & e^{2i\alpha} \\ e^{-2i\alpha} & 1 \end{pmatrix}$
$\delta-$ phaseplate at x axis	$\begin{pmatrix} e^{i\frac{\delta}{2}} & o \\ 0 & e^{-i\frac{\delta}{2}} \end{pmatrix}$	$\frac{1}{2}\begin{pmatrix} \cos\frac{\delta}{2} & i\sin\frac{\delta}{2} \\ i\sin\frac{\delta}{2} & \cos\frac{\delta}{2} \end{pmatrix}$
Polarization rotator by θ	$\begin{pmatrix} \cos\theta & -\sin\theta \\ \sin\theta & \cos\theta \end{pmatrix}$	$\frac{1}{2}\begin{pmatrix} e^{i\theta} & 0 \\ 0 & e^{-i\theta} \end{pmatrix}$

Table 3.1: Jones matrices of optical elements.

can be derived by multiplication of matrices of each sub-system in right order. That can be written as

$$\mathbb{M} = \mathbb{M}_n \dots \mathbb{M}_1. \tag{3.11}$$

It is important to notice that the first matrix is in the right side of the equation. To clarify our results we will show an example of two rotators, first rotating by angle α, second by angle β. One would expect the resulting rotation by angle $\alpha+\beta$ but let's have a look what we get from Jones formalism.

As described above, the matrix of whole system is derived by multiplication of matrices of two rotators

$$\begin{aligned} \mathbb{M} &= \begin{pmatrix} \cos\alpha & \sin\alpha \\ -\sin\alpha & \cos\alpha \end{pmatrix}\begin{pmatrix} \cos\beta & \sin\beta \\ -\sin\beta & \cos\beta \end{pmatrix} = & (3.12)\\ &= \begin{pmatrix} \cos\alpha\cos\beta - \sin\alpha\sin\beta & \cos\alpha\sin\beta + \sin\alpha\cos\beta \\ -\sin\alpha\cos\beta - \cos\alpha\sin\beta & -\sin\alpha\sin\beta + \cos\alpha\cos\beta \end{pmatrix} = & (3.13)\\ &= \begin{pmatrix} \cos\alpha+\beta & \sin\alpha+\beta \\ -\sin\alpha+\beta & \cos\alpha+\beta \end{pmatrix}. & (3.14) \end{aligned}$$

In last step, formulas for $\cos(\alpha+\beta)$ and $\sin(\alpha+\beta)$ were used. This result is the rotation by $\alpha+\beta$ indeed.

It is vital to always work with matrices in the same base. Otherwise, we would obtain false results. When we use transformation between bases, it does not matter, if we transform each used matrix or transform their final multiplication.

3.1.4 Interaction with sample

In general term, we do not know how sample interacts with light. Therefore we begin with general form of Jones matrix

$$\mathbb{S}_R = \begin{pmatrix} r_{ss} & r_{sp} \\ r_{ps} & r_{pp} \end{pmatrix}, \tag{3.15}$$

$$\mathbb{S}_T = \begin{pmatrix} t_{ss} & t_{sp} \\ t_{ps} & t_{pp} \end{pmatrix}. \tag{3.16}$$

These matrices describe the most general anisotropic material. You can see that we listed matrices for both reflection and transmission. We will need them both

later. We choose coordinate system with p direction perpendicular and s parallel to the plane of incidence. The choice of letters for each component is also not random, because they do correspond to Fresnel coefficients of reflection and transmission[52].

For medium in magnetic field it must be fulfilled

$$\begin{aligned} \mathbb{R}(-\alpha)\mathbb{S}_R\mathbb{R}(\alpha) &= \mathbb{S}_R, & (3.17)\\ \mathbb{R}(-\alpha)\mathbb{S}_T\mathbb{R}(\alpha) &= \mathbb{S}_T, & (3.18)\\ & & (3.19) \end{aligned}$$

where $\mathbb{R}(\alpha)$ is matrix of rotation by arbitrary angle α along the magnetization vector. This relation corresponds to rotation invariance and provide important relations between the two diagonal and the two off-diagonal elements of the reflection and transmission matrices. For example for the polar configuration at normal incidence we can further derive relations

$$\begin{aligned} r_{ps} &= r_{sp}, & (3.20)\\ t_{ps} &= -t_{sp}, & (3.21)\\ r_{pp} &= -r_{ss}, & (3.22)\\ t_{pp} &= t_{ss}, & (3.23) \end{aligned}$$

and also conditions containing vector of magnetization looks like

$$\begin{aligned} r_{sp}(-\vec{M}) &= -r_{sp}(\vec{M}), & (3.24)\\ r_{ss}(-\vec{M}) &= r_{ss}(\vec{M}), & (3.25)\\ t_{sp}(-\vec{M}) &= -t_{sp}(\vec{M}), & (3.26)\\ t_{ss}(-\vec{M}) &= t_{ss}(\vec{M}). & (3.27) \end{aligned}$$

Magneto-optical quantities can be derived from these coefficients. We start with definition of magneto-optical angles[55]

$$\begin{aligned} -\frac{r_{ps}}{r_{ss}} &= \Theta_{Ks} \approx \theta_{Ks} - i\epsilon_{Ks}, & (3.28)\\ \frac{t_{ps}}{t_{ss}} &= \Theta_{Fs} \approx \theta_{Fs} - i\epsilon_{Fs}, & (3.29)\\ \frac{r_{sp}}{r_{pp}} &= \Theta_{Kp} \approx \theta_{Kp} - i\epsilon_{Kp}, & (3.30)\\ -\frac{r_{pp}}{r_{pp}} &= \Theta_{Fp} \approx \theta_{Fp} - i\epsilon_{Fp}. & (3.31) \end{aligned}$$

The relations listed above can be used only for small angles which will be fulfilled for samples we are going to study. In further text, parameter θ is called magneto-optical rotation and ϵ magneto-optical ellipticity.

In the case of normal incidence, symmetry induces $\Theta_{Ks} = \Theta_{Kp} = \Theta_K$. Same applies for transmission (Faraday) magneto-optical angles.

Now we can simplify form Jones matrix describing the sample. Since it is common to normalize Jones vecotrs, we can divide all elements by diagonal element

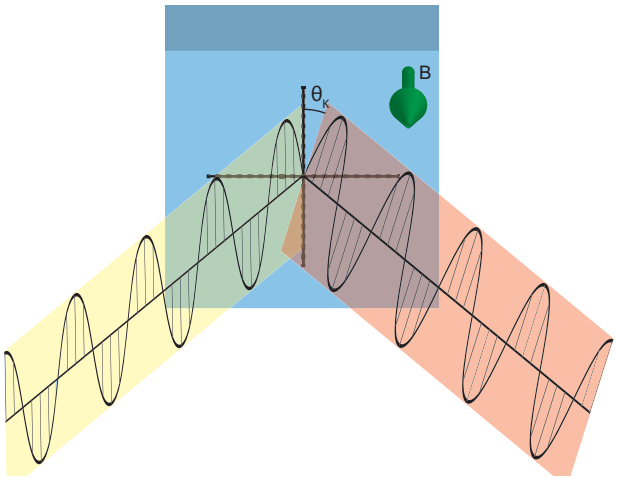

Figure 3.1: Schematic picture of polar Kerr rotation.

from matrix (3.15) and (3.16). After insertion of definitions of magneto-optical angles we obtain

$$\mathbb{S}_R = \begin{pmatrix} 1 & -\Theta_K \\ -\Theta_K & -1 \end{pmatrix}, \tag{3.32}$$

$$\mathbb{S}_T = \begin{pmatrix} 1 & -\Theta_K \\ \Theta_F & 1 \end{pmatrix}. \tag{3.33}$$

From this form we can see that magneto-optical angles describe interaction between s and p waves. This interaction can generally cause two effects. First changes azimuth of polarization. For linearly polarized light it means rotation of plane of polarization (Fig. 3.1). Second causes the change of ellipticity. For linearly polarized light it means that it becomes elliptically polarized. These effects are well separated in our description in real and imaginary part of magneto-optical angles.

4. Light propagation in anisotropic media

In this section, we will describe, how the propagation of light changes if the symmetry of the system is broken. The simplest situation, which we can look at, is the introduction of homogeneous magnetic field, which will induce the optical anisotropy in the system.

Once again, we start with Maxwell's equations for homogeneous system without charges and currents

$$\nabla \times \vec{H} - \frac{\partial \vec{D}}{\partial t} = 0, \tag{4.1}$$

$$\nabla \cdot \vec{D} = 0, \tag{4.2}$$

$$\nabla \times \vec{E} + \frac{\partial \vec{B}}{\partial t} = 0, \tag{4.3}$$

$$\nabla \cdot \vec{B} = 0. \tag{4.4}$$

Since we are working with wavelengths at optical frequencies, we can assume that $\hat{\mu} = \mu_0$. Then we will need permittivity tensor that was introduced in previous chapter

$$\hat{\varepsilon} = \begin{pmatrix} \varepsilon_{11} & \varepsilon_{12} & \varepsilon_{13} \\ \varepsilon_{21} & \varepsilon_{22} & \varepsilon_{23} \\ \varepsilon_{31} & \varepsilon_{32} & \varepsilon_{33} \end{pmatrix}. \tag{4.5}$$

Presence of external magnetic field induces optical anisotropy in our system. We can look at how solution of wave equation looks like in this situation. First, we can insert solution (2.22) into equation (2.7) to obtain

$$\vec{k} \times \vec{k} \times \vec{E} + \omega^2 \hat{\varepsilon} \mu_0 \vec{E} = 0. \tag{4.6}$$

Then we need to define new quantity called reduced wave vector

$$\vec{\bar{N}} = \frac{c}{\omega}\vec{k} = \bar{N}_1 \hat{i} + \bar{N}_2 \hat{j} + \bar{N}_3 \hat{k}. \tag{4.7}$$

For the description of propagation of light, we need to solve equation (4.6). First we will rewrite it to its Cartesian components. With help of Levi-civit antisymmetric tensor we can write[55]

$$\epsilon_{ijk} k_j \epsilon_{klm} k_l E_m + \frac{\omega^2}{c^2} \varepsilon_{ij} E_j = 0. \tag{4.8}$$

After the substitution of identity

$$\epsilon_{ijk}\epsilon_{klm} = \delta_{ij}\delta_{jm} - \delta_{im}\delta_{jl}, \tag{4.9}$$

where δ is Kronecker delta, we get

$$k_i k_j E_j - k_j k_j E_i + \frac{\omega^2}{c^2} \varepsilon_{ij} E_j = 0. \tag{4.10}$$

Now we introduce reduced wave vector (4.7) to get

$$\bar{N}_i\bar{N}_jE_j - \bar{N}_j\bar{N}_jE_i + \varepsilon_{ij}E_j = 0. \tag{4.11}$$

We did not place any conditions on the definition of reduced weve vector. That allows us to choose Cartesian system, where $\bar{N}_1 = 0$. With this choice, we can rewrite equation (4.11) in matrix form

$$\begin{pmatrix} \varepsilon_{11} - \bar{N}_2^2 - \bar{N}_3^2 & \varepsilon_{12} & \varepsilon_{13} \\ \varepsilon_{21} & \varepsilon_{22} - \bar{N}_3^2 & \varepsilon_{23} + \bar{N}_2\bar{N}_3 \\ \varepsilon_{31} & \varepsilon_{32} + \bar{N}_2\bar{N}_3) & \varepsilon_{33} - \bar{N}_2^2 \end{pmatrix} \begin{pmatrix} E_1 \\ E_2 \\ E_3 \end{pmatrix} = 0. \tag{4.12}$$

If we want to get specific solutions of this equation, we need to specify one component of wave vector. In our situation, we know the value $\bar{N}_2$. In order to obtain non-trivial solution of (4.12), the determinant of matrix has to be zero. This condition gives us characteristic equation, which is boundary condition for existence of $\bar{N}_3$

$$\bar{N}_3^4\varepsilon_{33} + \bar{N}_3^3[\bar{N}_2(\varepsilon_{23} + \varepsilon_{32})] \tag{4.13}$$

$$-\bar{N}_3^2[\varepsilon_{22}(\varepsilon_{33} - \bar{N}_2^2) + \varepsilon_{33}(\varepsilon_{11} + \bar{N}_2^2) - \varepsilon_{13}\varepsilon_{31} - \varepsilon_{23}\varepsilon_{32}] \tag{4.14}$$

$$-\bar{N}_3[(\varepsilon_{11} - \bar{N}_2^2)(\varepsilon_{23} + \varepsilon_{32} - \varepsilon_{21}\varepsilon_{31} - \varepsilon_{21}\varepsilon_{13}]\bar{N}_2 \tag{4.15}$$

$$+\varepsilon_{22}[(\varepsilon_{11} - \bar{N}_2^2)(\varepsilon_{33} - \bar{N}_2^2) - \varepsilon_{13}\varepsilon_{31}] \tag{4.16}$$

$$-\varepsilon_{12}\varepsilon_{21}(\varepsilon_{33} - \bar{N}_2^2) - \varepsilon_{23}\varepsilon_{32}(\varepsilon_{11} - \bar{N}_2^2) + \varepsilon_{12}\varepsilon_{31}\varepsilon_{23} + \varepsilon_{21}\varepsilon_{13}\varepsilon_{32} = 0. \tag{4.17}$$

Since it is equation of the fourth order, four roots of this equation give us four solutions[56] of equation (4.12)

$$\vec{e}_j = \begin{pmatrix} -\varepsilon_{12}(\varepsilon_{33} - \bar{N}_2^2) + \varepsilon_{13}(\varepsilon_{32} + \bar{N}_2\bar{N}_{3j}) \\ (\varepsilon_{33} - \bar{N}_2^2)(\varepsilon_{11} - \bar{N}_2^2 - \bar{N}_{3j}^2) - \varepsilon_{13}\varepsilon_{31} \\ -(\varepsilon_{11} - \bar{N}_2^2 = \bar{N}_{3j}^2)(\varepsilon_{32} + \bar{N}_2\bar{N}_{3j}) + \varepsilon_{31}\varepsilon_{12} \end{pmatrix}. \tag{4.18}$$

Equation (4.18) describes eigenmodes of the system. These modes do not change during propagation and form a base that we can use to describe any electric field of the wave in the form of linear combination of these eigenmodes

$$\vec{E} = \sum_{j=1}^{4} E_{0j}\vec{e}_j e^{i(\omega t - \frac{\omega}{c}\bar{N}_j\cdot\vec{r})}. \tag{4.19}$$

The simplest solutions of this equation can be obtained for isotropic material in magnetic field that is parallel or orthogonal to the direction of propagation of light (x_3 axis). The solution of general direction of magnetic field is far more complex and we will not discuss it here.

4.1 Propagation along the magnetization vector

We start with magnetization vector $\vec{M}$ parallel to x_3 axis which is the direction of propagation of light. With respect to axial symmetry, we get reduced form of permittivity tensor

$$\hat{\varepsilon} = \begin{pmatrix} \varepsilon_1 & -i\varepsilon_2 & 0 \\ i\varepsilon_2 & \varepsilon_1 & 0 \\ 0 & 0 & \varepsilon_3 \end{pmatrix}. \tag{4.20}$$

With this simplification equation (4.12) gets to more workable form

$$\begin{pmatrix} \varepsilon_1 - \bar{N}_2^2 - \bar{N}_3^2 & -i\varepsilon_2 & 0 \\ i\varepsilon_2 & \varepsilon_1 - \bar{N}_3^2 & \bar{N}_2\bar{N}_3 \\ 0 & \bar{N}_2\bar{N}_3 & \varepsilon_3 - \bar{N}_2^2 \end{pmatrix} \begin{pmatrix} e_1 \\ e_2 \\ e_3 \end{pmatrix} = 0, \tag{4.21}$$

which leads to characteristic equation

$$\bar{N}_3^4 - \bar{N}_3^2[(\varepsilon_1 - \bar{N}_2^2)\varepsilon_3 + (\varepsilon_3 - \bar{N}_2^2)\varepsilon_1] \tag{4.22}$$

$$+[(\varepsilon_1 - \bar{N}_2^2)\varepsilon_1 - \varepsilon_2^2](\varepsilon_3 - \bar{N}_2^2) = 0. \tag{4.23}$$

Because of our choice of coordinate system we have $\bar{N}_2 = 0$, which reduces this equation to even more simple form

$$\bar{N}_3^4 - 2\varepsilon_1\bar{N}_3^2 + \varepsilon_1^2 - \varepsilon_2^2 = 0. \tag{4.24}$$

This is still equation of fourth order, but this time, the solutions are in form of two pairs which differ only in sign. If we start from

$$\bar{N}_3^2 = \varepsilon_1 \pm \varepsilon_2, \tag{4.25}$$

we can introduce notation

$$N_+ = \sqrt{\varepsilon_1 + \varepsilon_2} \tag{4.26}$$

$$N_- = \sqrt{\varepsilon_1 - \varepsilon_2}. \tag{4.27}$$

Now, if we look at eigenmodes of the system, we find out that their number is reduced to just two

$$\vec{e}_1 = \vec{e}_2 = \begin{pmatrix} 1 \\ i \end{pmatrix}; \vec{e}_3 = \vec{e}_4 = \begin{pmatrix} 1 \\ -i \end{pmatrix}, \tag{4.28}$$

which greatly corresponds to LHCP and RHCP light described in chapter above. Since we usually use description of matter by complex refractive index $N = n - ik$, we can rewrite out findings in the way

$$(n_\pm - ik_\pm)^2 = \varepsilon_1' - i\varepsilon_1'' \pm (\varepsilon_2' - i\varepsilon_2''), \tag{4.29}$$

where

$$\varepsilon_1 = \varepsilon_1' - i\varepsilon_1'', \tag{4.30}$$

$$\varepsilon_2 = \varepsilon_2' - i\varepsilon_2''. \tag{4.31}$$

We can solve equation (4.29) for square roots of real and imaginary parts of complex refractive index

$$n_\pm^2 = \frac{1}{2}\left[\sqrt{(\varepsilon_1' \pm \varepsilon_2')^2 + (\varepsilon_1'' + \varepsilon_2'')^2} + (\varepsilon_1' \pm \varepsilon_2')\right], \tag{4.32}$$

$$k_\pm^2 = \frac{1}{2}\left[\sqrt{(\varepsilon_1' \pm \varepsilon_2')^2 + (\varepsilon_1'' + \varepsilon_2'')^2} - (\varepsilon_1' \pm \varepsilon_2')\right]. \tag{4.33}$$

Difference between N_+ and N_- is small. Thanks to it, we can use linear approximation and use mean value N and deviation ΔN in form

$$N_\pm \approx N \pm \Delta N. \tag{4.34}$$

This leads to equations

$$N_+^2 + N_-^2 = 2\varepsilon_1, \tag{4.35}$$
$$N_+^2 - N_-^2 = 2\varepsilon_2. \tag{4.36}$$

If we sum these equations and neglect terms with higher than second order, we obtain

$$N_+^2 - N_-^2 \approx 4N\Delta N. \tag{4.37}$$

Now we can use the fact that the mean value of refractive index N is really close to value of isotropic state without external magnetic field and insert $\sqrt{\varepsilon_1} \approx N$. That allows us to derive the value of the deviation of refractive index

$$\Delta N \approx \frac{i\varepsilon_{12}}{2\sqrt{\varepsilon_{11}}}, \tag{4.38}$$

giving us relation between difference of refractive index for LHCP and RHCP light and off-diagonal element of permittivity tensor.

4.2 Polar Kerr effect at normal light incidence

With respect to previous chapters, we can derive formula for polar Kerr effect on the surface of a semi-infinite (bulk) magnetic at normal light incidence. We consider an interface between vacuum and medium magnetized out of plane. We already showed that eigenmodes of light propagating parallel to $\vec{M}$ are left and right handed circularly polarized. Propagation of these modes is fully described by complex refractive index N_+ and N_-.

We will use Fresnel equations for normal incidence of light, which can be written for both modes in form

$$r_\pm = -\frac{N_\pm - 1}{N_\pm + 1}. \tag{4.39}$$

If we look at the definition of magneto-optic Kerr quantities (3.31), we can directly input equation above into this definition and obtain

$$\theta_K - i\epsilon_K \approx i\frac{r_+ - r_-}{r_+ + r_-} = i\frac{N_+ - N_-}{N_+N_- - 1}. \tag{4.40}$$

Since the difference between refractive indexes r_+ and r_- is very small, we can neglect second order terms in ΔN. Results of these operations are

$$N_+ - N_- \approx 2\Delta N \approx i\frac{\varepsilon_{12}}{\varepsilon^{1/2}}, \tag{4.41}$$
$$N_+N_- \approx \varepsilon_1. \tag{4.42}$$

That gives us relation for polar Kerr effect in bulk sample at normal incidence

$$\theta_K - i\epsilon_K \approx \frac{i\varepsilon_2}{\sqrt{\varepsilon_1}(\varepsilon_1 - 1)}. \tag{4.43}$$

Now, if we rewrite ε_1 and ε_2 by their real and imaginary parts and use $\sqrt{\varepsilon_1} \approx n - ik$, we can separate real and imaginary parts of Kerr effect into two independent equations

$$\theta_K \approx \frac{\varepsilon_2'' C - \varepsilon_2' D}{C^2 + D^2}, \tag{4.44}$$

$$\epsilon_K \approx -\frac{\varepsilon_2' C + \varepsilon_2'' D}{C^2 + D^2}, \tag{4.45}$$

where

$$C = n(n^2 - 3k^2 - 1), \tag{4.46}$$

$$D = k(3n^2 - k^2 - 1). \tag{4.47}$$

We can reverse these equations to

$$\varepsilon_2'' = -(C\theta_K - D\epsilon_K), \tag{4.48}$$

$$\varepsilon_2' = -(C\epsilon_K + D\theta_K). \tag{4.49}$$

These equations allow us to obtain approximate values of off-diagonal element of permittivity tensor from the knowledge of experimentally measured Kerr effect and optical constants of material, that can be obtained from spectroscopic ellipsometry. Such magneto-optical analysis is really powerful tool, which allows us further simulation of more complex layered structures.

5. 4×4 matrix formalism for magnetic multilayers

In 1980 Yeh introduced matrix formalism for propagation of light in anisotropic non-absorbing layered media. This formalism was enhanced by Višňovský in 1986 for absorbing media and magneto-optical effects[56]. In the multilayer system, each layer is represented by two 4x4 matrices and their multiplication gives us optical response of the multilayer for even very complex systems. This approach is also very useful for numerical modelling and engineering of new structures.

As mentioned before, we consider layered structure containing of m layers. Each layer has its thickness t_i and is characterized by its permittivity tensor $\hat{\varepsilon}^{(i)}$. wave vector of incident light is $\vec{k_0}$. We choose x_3 axis to be perpendicular to layer interfaces and x_2 axis to be in plane of incidence. In previous chapter, we have shown that each layer has four eigenmodes of propagation. Additionally, we have to solve wave equation in two isotropic half-planes. To obtain optical response of system, we have to find the components $\bar{N}_{3j}$ of the reduced wave vector for given value of $\bar{N}_2$ and the corresponding electric field vectors $\vec{e}_j$. We know from Maxwell's equations that tangential components of electric field are continuous at the interface. With our choice of coordinate system with respect to Snell's law, $\bar{N}_2$ component of reduced wave vector is identical for every layer.

Our goal is to obtain reflection and transmission coefficients of our system for both polarizations from which we can calculate magneto-optical angles and other optical quantities. At first we have to calculate eigenmodes for each layer to be able to describe propagation inside these layers. Then we have to apply boundary conditions on this set of equations. That will introduce interaction of light with interface between layers. This condition is mentioned continuity of tangential component of electric and magnetic field components.

Previous chapter was dedicated to finding of eigenmodes for anisotropic material. With respect to its results, we can describe the field in the n-th layer taking into account that $\bar{N}_1 = 0$,

$$\vec{E}^{(n)} = \sum_{j=1}^{4} E_{0j}^{(n)} \vec{e}_j^{(n)} e \left\{ i\omega t - i\frac{\omega}{c}[\bar{N}_2 y + \bar{N}_{3j}^{(n)}(z - z_n)] \right\}, \tag{5.1}$$

where $E_{0j}^{(n)}$ is j-th component of corresponding eigenmode at z_n coordinates of the interface between n-th and *(n+1)*-th layer.

It was mentioned there will be need of use of tangential components of magnetic field at the interfaces. To obtain these vectors, we can use formula, which results from Maxwell's equations.

$$\vec{B} = \frac{1}{c}\bar{N} \times \vec{E}. \tag{5.2}$$

That allows us to introduce eigenmodes of magnetic field in form

$$\vec{b}_j^{(n)} = (\bar{N}_2 \vec{i}_2 + \bar{N}_{3j}^{(n)} \vec{i}_3) \times \vec{e}_j^{(n)}, \tag{5.3}$$

and decompose magnetic field similarly to electric one like

$$c\vec{B}^{(n)} = \sum_{j=1}^{4} E_{0j}^{(n)} \vec{b}_j^{(n)} \exp\left\{ i\omega t - i\frac{\omega}{c}[\bar{N}_y y + \bar{N}_{zj}^{(n)}(z - z_n)] \right\}. \tag{5.4}$$

It is worth noticing, that both decompositions use same set of coefficients. Now if we write continuity requirement of tangential components of electric and magnetic field vectors at the interface between *(n-1)*-th and n-th layer, we obtain

$$\sum_{j=1}^{4} E_{0j}(z_{n-1}) \vec{e}_j^{(n-1)} \cdot \vec{i}_1 = \sum_{j=1}^{4} E_{0j}^{(n)}(z_n) \vec{e}_j^{(n)} \cdot \vec{i}_1 exp\left(i\frac{\omega}{c} \bar{N}_{zj}^{(n)} t_n \right), \tag{5.5}$$

$$\sum_{j=1}^{4} E_{0j}(z_{n-1}) \vec{b}_j^{(n-1)} \cdot \vec{i}_2 = \sum_{j=1}^{4} E_{0j}^{(n)}(z_n) \vec{b}_j^{(n)} \cdot \vec{i}_2 exp\left(i\frac{\omega}{c} \bar{N}_{zj}^{(n)} t_n \right), \tag{5.6}$$

$$\sum_{j=1}^{4} E_{0j}(z_{n-1}) \vec{e}_j^{(n-1)} \cdot \vec{i}_2 = \sum_{j=1}^{4} E_{0j}^{(n)}(z_n) \vec{e}_j^{(n)} \cdot \vec{i}_2 exp\left(i\frac{\omega}{c} \bar{N}_{zj}^{(n)} t_n \right), \tag{5.7}$$

$$\sum_{j=1}^{4} E_{0j}(z_{n-1}) \vec{b}_j^{(n-1)} \cdot \vec{i}_1 = \sum_{j=1}^{4} E_{0j}^{(n)}(z_n) \vec{b}_j^{(n)} \cdot \vec{i}_1 exp\left(i\frac{\omega}{c} \bar{N}_{zj}^{(n)} t_n \right). \tag{5.8}$$

You can see that whole set of these equations is linear. That means we can move from this notation to more comfortable matrix formalism. These equations can be written like

$$\mathbb{D}^{(n-1)} \vec{E}_0^{(n-1)}(z_{n-1}) = \mathbb{D}^{(n)} \mathbb{P}^{(n)} \vec{E}_0^{(n)}(z_n). \tag{5.9}$$

One can see, that all we need are two matrices for each layer. First $\mathbb{P}$ matrix is called propagation matrix and describes propagation of light wave inside layer. It is diagonal matrix and looks like

$$\mathbb{P}_{ij}^{(n)} = \delta_{ij} exp\left(i\frac{\omega}{c} \bar{N}_{3j}^{(n)} t_n \right). \tag{5.10}$$

Second, dynamic matrix $\mathbb{D}$, describes interaction at the interface and its rows can be easily constructed by

$$\mathbb{D}_{1j}^{(n)} = \vec{e}_j^{(n)} \cdot \hat{i}_1, \tag{5.11}$$

$$\mathbb{D}_{2j}^{(n)} = \vec{b}_j^{(n)} \cdot \hat{i}_2, \tag{5.12}$$

$$\mathbb{D}_{3j}^{(n)} = \vec{e}_j^{(n)} \cdot \hat{i}_2, \tag{5.13}$$

$$\mathbb{D}_{4j}^{(n)} = \vec{b}_j^{(n)} \cdot \hat{i}_1. \tag{5.14}$$

We can insert into its definition general solution of the wave equation (4.18), which yields dynamic matrix in its general form

$$\mathbb{D}_{1j}^{(n)} = -\varepsilon_{12}(\varepsilon_{11} - \bar{N}_2^2) + \varepsilon_{11}(\varepsilon_{12} + \bar{N}_2 \bar{N}_{3j}), \tag{5.15}$$

$$\mathbb{D}_{2j}^{(n)} = \bar{N}_{3j}^{(n)}[-\varepsilon_{12}^{(n)}(\varepsilon_{33}^{(n)} - \bar{N}_2^2) + \varepsilon_{13}(\varepsilon_{32}^{(n)} + \bar{N}_2 \bar{N}_{3j}^{(n)}] = \bar{N}_{3j}^{(n)} D_{1j}^{(n)}, \tag{5.16}$$

$$\mathbb{D}_{3j}^{(n)} = (\varepsilon_{33}^{(n)} - \bar{N}_2^2)(\varepsilon_{11}^{(n)} - \bar{N}_2^2 - \bar{N}_{3j}^{(n)^2}) - \varepsilon_{13}^{(n)} \varepsilon_{31}^{(n)}, \tag{5.17}$$

$$\begin{aligned} \mathbb{D}_{4j}^{(n)} = &-(\varepsilon_{11}^{(n)} - \bar{N}_2^2 - \bar{N}_{3j}^{(n)^2})(\bar{N})_2^{(n)} \varepsilon_{12}^{(n)} + \bar{N}_{3j}^{(n)} \varepsilon_{33}^{(n)}) \\ &+ \bar{N}_{3j}^{(n)} \varepsilon_{13}^{(n)} \varepsilon_{31}^{(n)} + \bar{N}_2^{(n)} \varepsilon_{31}^{(n)} \varepsilon_{12}^{(n)}. \end{aligned} \tag{5.18}$$

Since it is possible to inverse dynamic matrix, we can rewrite equation (5.9) as relation of electric field in n-th and *(n-1)*-th layer

$$\vec{E}_0^{(n-1)}(z_{n-1}) = \left[\mathbb{D}^{(n-1)}\right]^{-1} \mathbb{D}^{(n)}\mathbb{P}^{(n)}\vec{E}_0^{(n)}(z_n) = T_{n-1,n}\vec{E}_0^{(n)}(z_n). \tag{5.19}$$

Transfer matrix $\mathbb{T}_{n-1,n}$ is very useful way to shorten notation, especially for complex systems. Relation (5.19) can be further chained to obtain field at the end of the system just from conditions at the beginning of the system and matrix multiplication of dynamic and propagation matrices of layers of system. In short, it can be written like

$$\vec{E}_0^{(0)}(z_0) = \left[\Pi_{n=1}^{m+1}\mathbb{T}_{n-1,n}\right] \vec{E}_0^{(m+1)}(z_m) = \mathbb{M}\vec{E}_0^{(m+1)}(z_m). \tag{5.20}$$

At the end, we introduced matrix $\mathbb{M}$ that represent optical response of system. Derivation of all optical quantities from this matrix will be shown in the following chapter.

Sometimes it is useful to separate optical properties of layers. In notation used above, in transfer matrix, there is mixture of matrices of n-th and *(n-1)*-th layer. Therefore we introduce matrix

$$\mathbb{L}_n = \mathbb{D}^{(n)}\mathbb{P}^{(n)} \left[\mathbb{D}^{(n)}\right]^{-1}. \tag{5.21}$$

Equation (5.19) can be now written as

$$\vec{E}_0^{(0)} = \left[\mathbb{D}^{(0)}\right]^{-1} \left[\Pi_{n=1}^{m}\mathbb{L}_n\right] \mathbb{D}^{(m+1)}\vec{E}_0^{(m+1)}(z_m). \tag{5.22}$$

This approach is extremely useful for computer modelling since each layer is represented by its own matrix, which we can easily manipulate with.

5.1 Isotropic layer

Our sample usually consists not only from anisotropic layers, but also at least one layer that is isotropic. Therefore we must also look at eigenmodes of such material. In isotropic medium the situation is much more simple. Permittivity tensor is diagonal and characterized just by one complex number $\varepsilon_{kk}^{(n)} = \varepsilon_1^{(n)} = N^{(n)^2}$. If we look at eigenmodes we used before, we obtain zeros. Therefore we have to look for another solutions for wave equation. Since $\bar{N}_2 = const$, we obtain just two options of wave vector

$$\vec{k}_{1,2} = \frac{\omega}{c}\left[\bar{N}_2\vec{i}_2 \pm Q^{(n)}\vec{i}_1\right], \tag{5.23}$$

where

$$Q^{(n)} = \sqrt{\varepsilon_1^{(n)} - \bar{N}_2^2} = \sqrt{N^{(n)^2} - \bar{N}_2^2}. \tag{5.24}$$

Since the medium is isotropic, eigenmodes can be chosen arbitrarily. We choose base of linearly polarized light $\vec{e}_{3j}^{(n)}$ and $\vec{b}_{3j}^{(n)}$, because it is more compatible with equations used above. Their notations in Cartesian coordinates are written in table (5.1). You can see that eigenmodes correspond to s and p polarized wave

$\bar{N}_{31}^{(n)} = Q^{(n)}$	$\bar{N}_{32}^{(n)} = -Q^{(n)}$	$\bar{N}_{33}^{(n)} = Q^{(n)}$	$\bar{N}_{34}^{(n)} = -Q^{(n)}$
$e_1^{(n)} = \begin{pmatrix} 1 \\ 0 \\ 0 \end{pmatrix}$	$e_2^{(n)} = \begin{pmatrix} 1 \\ 0 \\ 0 \end{pmatrix}$	$e_3^{(n)} = \begin{pmatrix} 0 \\ Q^{(n)}/N^{(n)} \\ -\bar{N}_2/N^{(n)} \end{pmatrix}$	$e_4^{(n)} = \begin{pmatrix} 0 \\ Q^{(n)}/N^{(n)} \\ \bar{N}_2/N^{(n)} \end{pmatrix}$
$b_1^{(n)} = \begin{pmatrix} 0 \\ Q^{(n)} \\ -\bar{N}_2 \end{pmatrix}$	$b_2^{(n)} = \begin{pmatrix} 0 \\ -Q^{(n)} \\ -\bar{N}_2 \end{pmatrix}$	$b_3^{(n)} = \begin{pmatrix} -N^{(n)} \\ 0 \\ 0 \end{pmatrix}$	$b_4^{(n)} = \begin{pmatrix} N^{(n)} \\ 0 \\ 0 \end{pmatrix}$

Table 5.1: Table of proper modes of anisotropic medium written in Cartesian coordinates.

and odd modes represent propagation forward, while even ones propagation backwards. With the knowledge of proper modes we can construct dynamic matrix

$$\mathbb{D}^{(n)} = \begin{pmatrix} 1 & 1 & 0 & 0 \\ Q^{(n)} & -Q^{(n)} & 0 & 0 \\ 0 & 0 & Q^{(n)}/N^{(n)} & Q^{(n)}/N^{f(n)} \\ 0 & 0 & -N^{(n)} & N^{(n)} \end{pmatrix}. \tag{5.25}$$

Propagation matrix has the same form as in anisotropic media, which was described by equation (5.10).

In our calculation there has not to be isotropic layer but we always have to deal with two isotropic half-spaces corresponding to area in front and behind the sample. While describing these parts, it is useful to introduce angle of incidence $\phi^{(0)}$ instead of component of reduced wave vector $\bar{N}_2$. There is simple relation between them

$$\bar{N}_2 = N^{(0)} \sin \phi^{(0)}. \tag{5.26}$$

It is also worth to mention that in usual optical experiment we have same refractive index in both half-spaces which induces $Q^{(0)} = Q^{(m+1)}$. That ensures normalization of modes allowing the derivation of transmission and reflection coefficients directly from fields $E_{0j}^{(0)}(z_0)$ and $E_{0j}^{(m+1)}(z_m)$.

5.2 Reflection and Transmission coefficients

Now, we would like to derive reflection and transmission coefficients from knowledge of $\mathbb{M}$ matrix of our system. In usual optical experiment, we illuminate the sample only from one side. That means

$$E_{02}^{(m+1)} = E_{04}^{(m+1)} = 0. \tag{5.27}$$

If we rewrite equation (5.20) with this substitution, we obtain

$$\begin{pmatrix} E_{01}^{(0)}(z_0) \\ E_{02}^{(0)}(z_0) \\ E_{03}^{(0)}(z_0) \\ E_{04}^{(0)}(z_0) \end{pmatrix} = \begin{pmatrix} M_{11} & M_{12} & M_{13} & M_{14} \\ M_{21} & M_{22} & M_{23} & M_{24} \\ M_{31} & M_{32} & M_{33} & M_{34} \\ M_{41} & M_{42} & M_{43} & M_{44} \end{pmatrix} \begin{pmatrix} E_{01}^{(m+1)}(z_0) \\ 0 \\ E_{03}^{(m+1)}(z_0) \\ 0 \end{pmatrix}. \tag{5.28}$$

We can decompose it into the set of linear equations. Then we define coefficients r_{ij} and t_{ij} is usual form using equations

$$r_{12} = \left(\frac{E_{02}^{(0)}(z_0)}{E_{01}^{(0)}(z_0)} \right)_{E_{03}^{(0)}(z_0)=0} = \frac{M_{21}M_{33} - M_{23}M_{31}}{M_{11}M_{33} - M_{13}M_{31}}, \tag{5.29}$$

$$r_{14} = \left(\frac{E_{04}^{(0)}(z_0)}{E_{01}^{(0)}(z_0)} \right)_{E_{03}^{(0)}(z_0)=0} = \frac{M_{41}M_{33} - M_{43}M_{31}}{M_{11}M_{33} - M_{13}M_{31}}, \tag{5.30}$$

$$r_{34} = \left(\frac{E_{04}^{(0)}(z_0)}{E_{03}^{(0)}(z_0)} \right)_{E_{01}^{(0)}(z_0)=0} = \frac{M_{11}M_{43} - M_{41}M_{13}}{M_{11}M_{33} - M_{13}M_{31}}, \tag{5.31}$$

$$r_{32} = \left(\frac{E_{02}^{(0)}(z_0)}{E_{03}^{(0)}(z_0)} \right)_{E_{01}^{(0)}(z_0)=0} = \frac{M_{11}M_{23} - M_{21}M_{13}}{M_{11}M_{33} - M_{13}M_{31}}. \tag{5.32}$$

These coefficients are also related to reflection coefficients used in Jones formalism via[55]

$$\begin{pmatrix} r_{ss} & r_{sp} \\ r_{ps} & r_{pp} \end{pmatrix} = \begin{pmatrix} r_{12} & r_{32} \\ -r_{14} & -r_{34} \end{pmatrix}. \tag{5.33}$$

Similar process can be done for transmission coefficients

$$t_{11} = \left(\frac{E_{01}^{(m+1)}(z_m)}{E_{01}^{(0)}(z_0)} \right)_{E_{03}^{(0)}(z_0)=0} = \frac{M_{33}}{M_{11}M_{33} - M_{13}M_{31}}, \tag{5.34}$$

$$t_{13} = \left(\frac{E_{03}^{(m+1)}(z_m)}{E_{01}^{(0)}(z_0)} \right)_{E_{03}^{(0)}(z_0)=0} = \frac{-M_{31}}{M_{11}M_{33} - M_{13}M_{31}}, \tag{5.35}$$

$$t_{33} = \left(\frac{E_{03}^{(m+1)}(z_m)}{E_{03}^{(0)}(z_0)} \right)_{E_{01}^{(0)}(z_0)=0} = \frac{M_{11}}{M_{11}M_{33} - M_{13}M_{31}}, \tag{5.36}$$

$$t_{31} = \left(\frac{E_{01}^{(m+1)}(z_m)}{E_{03}^{(0)}(z_0)} \right)_{E_{01}^{(0)}(z_0)=0} = \frac{-M_{13}}{M_{11}M_{33} - M_{13}M_{31}}, \tag{5.37}$$

and relation with Jones formalism looks like

$$\begin{pmatrix} t_{ss} & t_{sp} \\ t_{ps} & t_{pp} \end{pmatrix} = \begin{pmatrix} t_{11} & t_{31} \\ t_{13} & t_{33} \end{pmatrix}. \tag{5.38}$$

Now, when we have connection to Jones formalism, we can compare results of Yeh formalism with experimentally obtained data. We can also directly calculate magneto-optical effects just from the knowledge of permittivity tensor of studied structure.

6. Experimental methods

6.1 Spectroscopic ellipsometry

Spectroscopic ellipsometry is an experimental technique measuring a change in polarization as light reflects or transmits from a material structure. The measured response depends on optical properties and thickness of individual materials. Thus, ellipsometry is primarily used to determine film thickness and optical constants ($\hat{\varepsilon}$). However, it is also applied to characterize composition, crystallinity, roughness, doping concentration, and other material properties associated with a change in optical response.

Measured change in polarization is characterized by two ellipsometric parameters Ψ and Δ, that are defined as

$$\rho = \frac{r_{pp}}{r_{ss}} = \tan \Psi e^{i\Delta}, \tag{6.1}$$

where r_{pp} and r_{ss} are reflection coefficients of s- and p-polarized incident wave respectively. Thickness, optical constants, and other properties are derived from these angles via advanced mathematical modelling using phenomenological description of interaction of light with matter, which will be more described below.

There are two main formalisms used to describe ellipsometric data. First, already explained in Chapter 3.1, is the Jones formalism. The other, more powerful, Muller formalism adds depolarization of the sample as an additional parameter. For description of light it uses Stokes vectros and will not be further described in this thesis. One can seek proper literature, for example [53].

Figure 6.1: RC2 Woolam ellipsometer.

In our measurements we use Muller matrix ellipsometer Woollam RC2 with dual rotating compensators (Fig. 6.1) and multichannel detection working in photon energy range from 1.24 to 6.5 eV. To describe basic functionality of the ellipsometric setup we will employ simplified model. It contains only rotating polarizer with frequency ω, sample and analyzer (Scheme in Fig. 6.2). If we

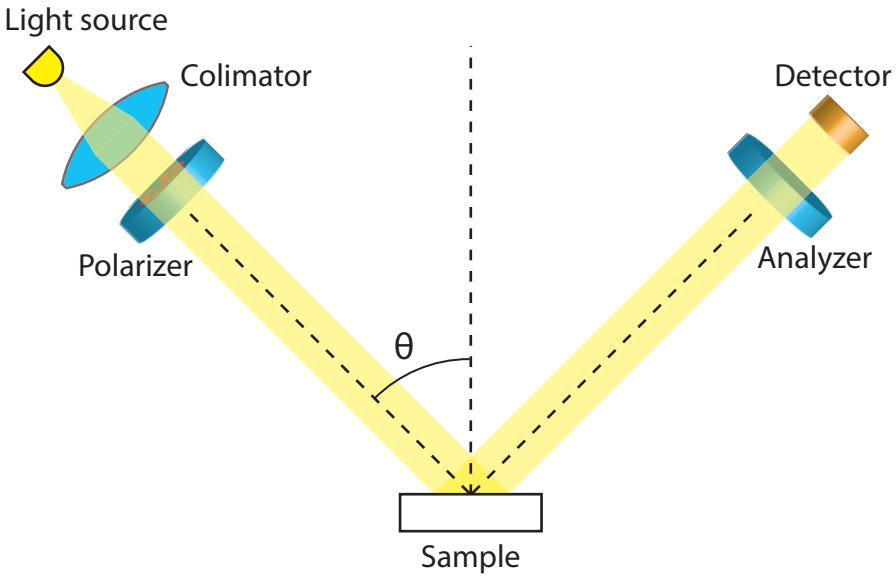

Figure 6.2: Scheme of basic ellipsometric setup.

multiply Jones matrices of these components we obtain

$$\begin{pmatrix} 1 & 0 \\ 0 & 0 \end{pmatrix} \begin{pmatrix} r_{ss} & 0 \\ 0 & r_{pp} \end{pmatrix} \begin{pmatrix} \sin(\omega t) \\ \cos(\omega t) \end{pmatrix} = \begin{pmatrix} r_{ss} \sin(\omega t) \\ 0 \end{pmatrix}. \tag{6.2}$$

The Jones vector is related to the intensity via

$$I = \frac{1}{2} J^{+} J. \tag{6.3}$$

Therefore the intensity at the detector is related to

$$I = \frac{|r_{ss}|^2}{2} \sin^2(\omega t). \tag{6.4}$$

One can see that the intensity is oscillating with frequency ω and amplitude proportional $|r_{ss}|^2$. Lock-in amplifier can separate this term from time dependent intensity. Now we can turn the analyzer by 90 degrees to obtain $|r_{pp}|^2$. Their ratio gives $\tan \Psi$. For measurement of Δ one has to put phase plate between the sample and the analyzer. Experimental setup for our measurements works with crossed polarizers and two rotating compensators on both sides of the sample. Such setup can obtain both ellipsometric parameters and complete Muller matrix from one measurement.

Now we can look at the theoretical modelling of ellipsometric parameters. We mentioned above pseudo-optical constants that are defined as

$$< \varepsilon >= \sin^2 \theta \left[1 + \tan^2 \theta \left(\frac{1-\rho}{1+\rho} \right)^2 \right], \tag{6.5}$$

where ρ was defined by Eq. (6.1) and θ in angle of incidence.

If we study just bulk sample without any layer on the surface, it actually corresponds to diagonal element of permittivity tensor. For the real sample, there

is almost always at least thin oxide layer, that may change optical response of studied material. Therefore we have to use more advanced theory of light propagation through multilayered system. This is usually done by proper software, which requires only description of studied structure. More we know about the sample, better is the fitting, because there are many free parameters, which can provide non-physical results. After the model structure is defined in the software, it calculates its optical response giving the theoretical values Ψ and Δ. If the initial values are not known, an estimate is given for the purpose of the preliminary calculation. The calculated values are compared with experimental data and the least square minimization method is used. If there is a good agreement between experimental and theoretical fit, and the results have physical meaning, we can assume they are reasonably correct. Some of parameters can be obtained before analysis from another measurements, for example roughness from atomic force microscopy.

6.2 Magneto-optical spectroscopy

Magneto-optical spectroscopy is an effective, non-destructive method for probing magnetic properties of magnetic materials and nanostructures. The spectral dependence of magneto-optical effects carries an important information about the electronic structure in magnetic material. There are various geometries that allow probing magneto-optical effects. We can study transmission (Faraday effect) or reflection (Kerr effects). We usually focus on effects linear in magnetization. That can be described by magneto-optical angle Θ, which was already defined in section 3.1.4. Considering polar Kerr effect, rotation as small as a few millidegrees have to be resolved.

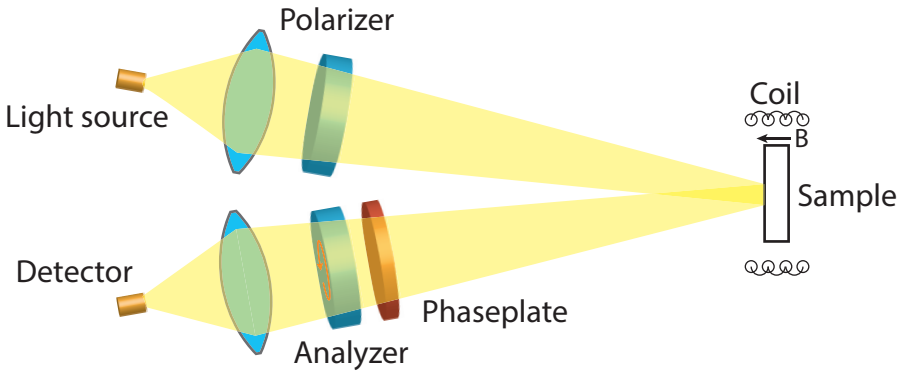

Figure 6.3: Scheme of magneto-optical spectrometer with rotating analyzer.

Our measurement setup is based on a method with nearly crossed polarizators. Basic scheme of this setup is shown in Fig. 6.3. Light of broad spectral range is brought to the setup from the lamp via optical fibre. This light is collimated by first lens. Since the light from the lamp is not polarized, there is a polarizer, that gives us linearly polarized light. Angle between the plane of polarization and the plane of incidence can be arbitrarily chosen by its rotation, but we generally use p-polarization. After interaction with the sample, which is placed in magnetic field

generated by electromagnet, light impacts the second polarizer. This polarizer is rotated by an angle α from crossed position with the first polarizer. Finally, the light is focused to the second fibre that brings it to CCD spectrometer, which gives us spectrally dependent light intensity.

We can derive the dependence of the light intensity at the detector with respect to the analyzer rotation using Jones formalism. We start with multiplication of Jones matrices of all optical components, neglecting those having no influence on polarization state of light and starting with the polarization state after the transmission through the first polarizer

$$\mathbb{M} = \begin{pmatrix} \sin^2\alpha & \sin\alpha\cos\alpha \\ \sin\alpha\cos\alpha & \cos^2\alpha \end{pmatrix} \begin{pmatrix} e^{i\frac{\delta}{2}} & 0 \\ 0 & e^{-i\frac{\delta}{2}} \end{pmatrix} \begin{pmatrix} 1 & -\Theta_K \\ -\Theta_K & -1 \end{pmatrix}. \tag{6.6}$$

Multiplication of these matrices yields

$$\mathbb{M} = \begin{pmatrix} e^{i\frac{\delta}{2}}\sin^2\alpha - \Theta_K e^{-i\frac{\delta}{2}}\cos\alpha\sin\alpha & -\Theta_K e^{\frac{\delta}{2}}\sin^2\alpha - e^{-i\frac{\delta}{2}}\cos\alpha\sin\alpha \\ -\Theta_K e^{-i\frac{\delta}{2}}\cos^2\alpha + e^{i\frac{\delta}{2}}\cos\alpha\sin\alpha & e^{-i\frac{\delta}{2}}\cos^2\alpha - \Theta_K e^{i\frac{\delta}{2}}\cos\alpha\sin\alpha \end{pmatrix}. \tag{6.7}$$

Now, if we set the incident light as s-polarized (Jones vector $\begin{pmatrix} 1 \\ 0 \end{pmatrix}$) at first polarizer, we get Jones vector of detected light in the form

$$J = \begin{pmatrix} e^{i\frac{\delta}{2}}\sin^2\alpha - \Theta_K e^{-i\frac{\delta}{2}}\cos\alpha\sin\alpha \\ -\Theta_K e^{-i\frac{\delta}{2}}\cos^2\alpha + e^{i\frac{\delta}{2}}\cos\alpha\sin\alpha \end{pmatrix}. \tag{6.8}$$

As before, the intensity is obtained using equation (6.3). Insertion of (6.8) into this relation yields

$$I \approx (\cos^2\alpha + |\Theta_K|^2\sin^2\alpha + \sin(2\alpha)\Re(\Theta_K e^{i\delta})). \tag{6.9}$$

Now we can make few simple approximations. Kerr effect is usually very small. Therefore we can neglect terms quadratic in Θ_K. We can also use equation (3.31). Finally, we will add constant term corresponding to dark current in CCD. Resulting dependence of detected intensity on the angle of analyzer is

$$I \approx \cos^2\alpha + (\theta_K\cos\delta + \epsilon_K\sin\delta)\sin(2\alpha) + C. \tag{6.10}$$

With knowledge of this relation we can measure the intensity for several angles and fit this dependence to measured data. Because fitting both rotation and ellipticity into one set of data, would be complicated, we separate these measurements. This is done by removing phase plate, which means that in such measurement δ is equal to zero and we obtain pure magneto-optical rotation. To extract magneto-optical ellipticity we combine experiments with and without phase plate.

In our calculations we did not include any misalignment of polarizers. To ensure it does not contribute to our data, we use the fact that linear magneto-optical effects are odd in magnetization. Since misalignment does not have such symmetry in magnetic field, simple subtraction of measurements of opposite field directions terminates this effect. Of course we have to divide result of this process by two to get actual value of Kerr effect.

Other Kerr geometries and even measurement of Faraday effect could be derived by similar procedure. Results of that yield same formulas with just one possible change in sign of term with magneto-optical effect.

Figure 6.4: Picture of magneto-optical spectrometer with rotating analyzer.

6.2.1 Technical details

A picture of magneto-optical spectrometer we use for experimental measurements is shown in Fig. 6.4.

As a light source we use high power Xe lamp made by Hamamatsu Photonics or DH-2000-BAL lamp from Ocean Optics, which combines halogen and deuterium lamps. Both lamps give good intensity over whole measured spectral range which is ranging from 1.2 to 5.5 eV. However despite its better intensity in UV region, Xe lamp suffers for higher intensity fluctuations which results in higher noise in Kerr signal.

We use α-BBO Roshon polarizers. These polarizers have high deviation angle, which allows use of shorter optical path from the source to the detector. This greatly improves the setup performance when we need to focus the beam into a small area on the sample. All lenses in setup are fabricated from quartz.

We use two different CCD spectrometers. First is Ocean optics Usb 2000+. This CCD detector operates from 200 to 900 nm with the chip of 2048 pixels. That gives us resolution about 0.35 nm. This device is more compact than the second one, but due to worse control over CCD chip it cannot measure higher intensities and makes measurements with Xe lamp impossible due to its spectral peaks. Second device is Shamrock SR-303i. This newer spectrometer allows to cool the chip down to -90°C, which results in significant reduction of noise coming

from dark current and way better signal-noise ratio. Since this spectrometer is equipped with 3 different movable gratings, we can measure in the spectral range from 190 nm to 1100nm with resolution better than 0.3 nm. Limitation in UV region comes from the spectral performance of the light source. This spectrometer, unlike the first one, allows control of the slit width and exposure time, which allows handling the intensity deviation among light sources. This spectrometer is also equipped with light guide that contains of sixteen separate optical fibres, which gives better transmission than simple optical fibre used with Ocean Optics spectrometer.

7. Experimental results

In this chapter we will describe and discuss experimental and theoretical results obtained on three different Heusler alloys. Each of these alloys undergoes a structural transformation induced by different mechanism.

Measurements of ellipsometric angles Ψ and Δ were done in spectral range from 1.24 to 6.5 eV. To ensure good fitting, five angles of incidence ranging from 55 to 70 degrees by 5 degrees were measured. All samples were cleaned prior measurements in isopropanol to remove dust and organical layers on top of samples.

Magneto-optical measurements were done in polar configuration with nearly normal angel of incidence. Measured spectral range was ranging from 1.2 to 5.4 eV. Samples were measured in magnetic field of 1.2 T.

All measurements except Ni-Mn-Ga were done at room temperature.

7.1 $Co_{(2-x)}Fe_{(1+x)}Si$

A set of five samples of $Co_{(2-x)}$ $Fe_{(1+x)}Si$ with x ranging from 0 to 1 was studied. These alloys are members of bigger group called Co-based Heusler alloys. These half-metallic alloys exhibit high Curie temperatures (up to 1100K) and the highest magnetic moment among Heusler alloys.

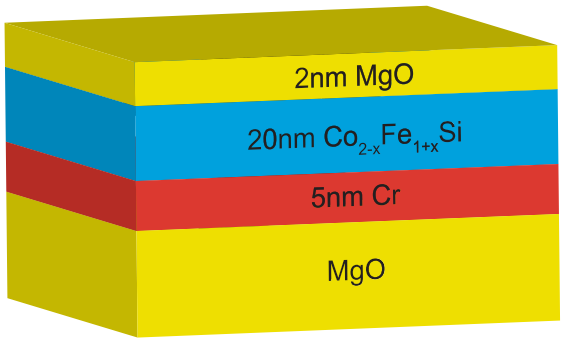

Figure 7.1: Scheme of structure samples with Co-Fe-Si alloys.

A structure of the samples is shown in Fig. 7.1. All samples were grown by co-sputtering system with typical base pressure of 10^{-9} mbar. Ar pressure of 2×10^{-3} mbar was kept during the sample deposition. The substrate is MgO with orientation (001) (lattice parameter: 4.21 Å). A buffer layer consisting 5 nm Cr and 5 nm of MgO was deposited onto MgO substrate prior to Heusler alloy layer to ensure ideal growth. To obtain smooth surface, the seed layers were in situ annealed at 700°C. 20 nm thick $Co_{(2-x)}Fe_{(1+x)}Si$ layers were grown by co-sputtering from elemental targets at room temperature. The layer stack was insitu post-annealed at 500°C to obtain good crystallinity. At the end of the process, the samples were covered by 2 nm thick MgO films to protect the Heusler layer from oxidation.

x	a[Å]	σ_a[Å]	c[Å]	σ_c[Å]
0	5.642	0.004	5.650	0.003
0.25	5.655	0.005	5.654	0.002
0.50	5.665	0.008	5.654	0.002
0.75	5.642	0.003	5.660	0.003
1.00	5.667	0.009	5.658	0.002

Table 7.1: Lattice parameters of $Co_{(2-x)}Fe_{(1+x)}Si$ alloys.

7.1.1 Structural properties

X-ray measurements on whole series of samples provided lattice parameters of grown Heusler alloys that are summarized in table 7.1.

It is obvious that all alloys are cubic with only small extension. This is in agreement with expected smooth transformation of alloy from Full-Heusler (Co_2FeSi) to Inverse-Heusler ($CoFe_2Si$), which both have cubic symmetry. Since there is only small difference in lattice constants, we can assume, that there is only negligible difference in strain that has no effect on band structure.

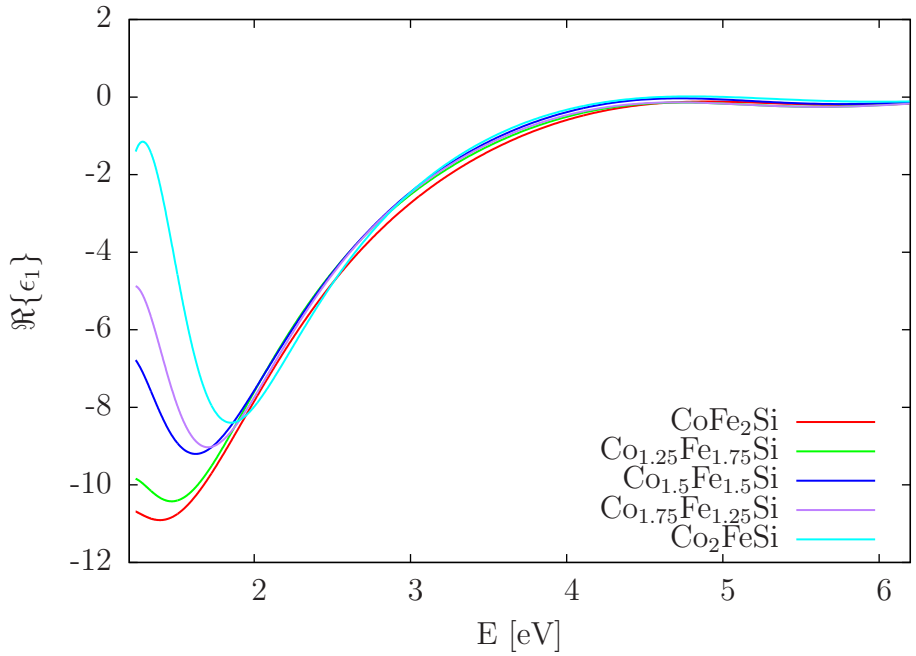

Figure 7.2: Optical properties of Co-Fe-Si alloys. The spectra of real part of diagonal element of permittivity tensor.

7.1.2 Optical properties

Obtained optical properties of Co-Fe-Si alloys are shown in Figs. 7.2 and 7.3. Optical properties and approximate thickness of buffer layers were acquired from separate set of samples with these layers deposited separately. For modelling of Heusler-alloy layer we started theoretical fitting of the experimental spectra of Ψ and Δ with point by point fitting which was afterwards parametrized by generic

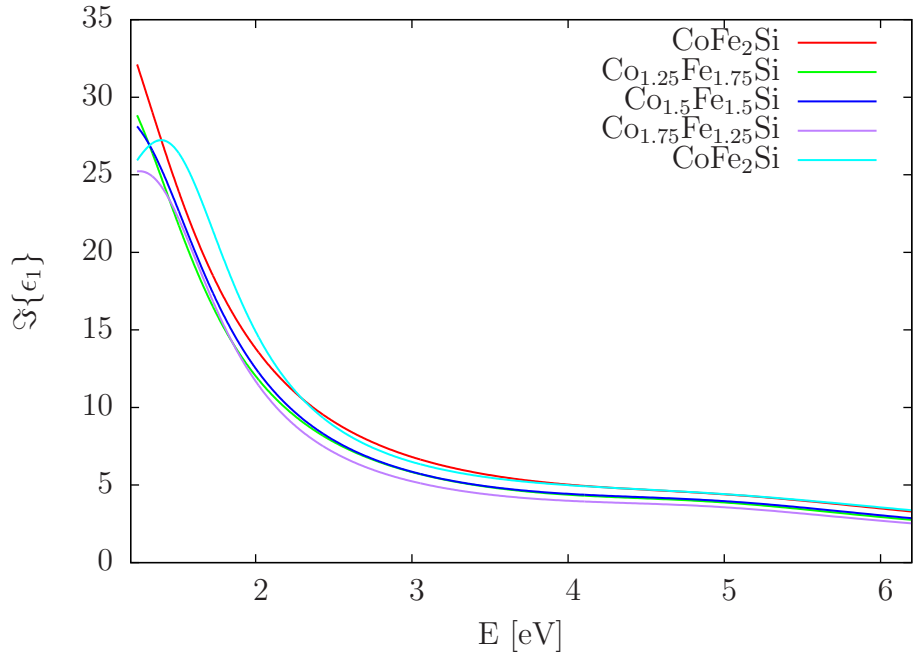

Figure 7.3: Optical properties of Co-Fe-Si alloys. The spectra of imaginary part of diagonal element of permittivity tensor.

oscillators. Positions of oscillators were selected with respect to DOS of Co_2FeSi (see Fig. 7.4).

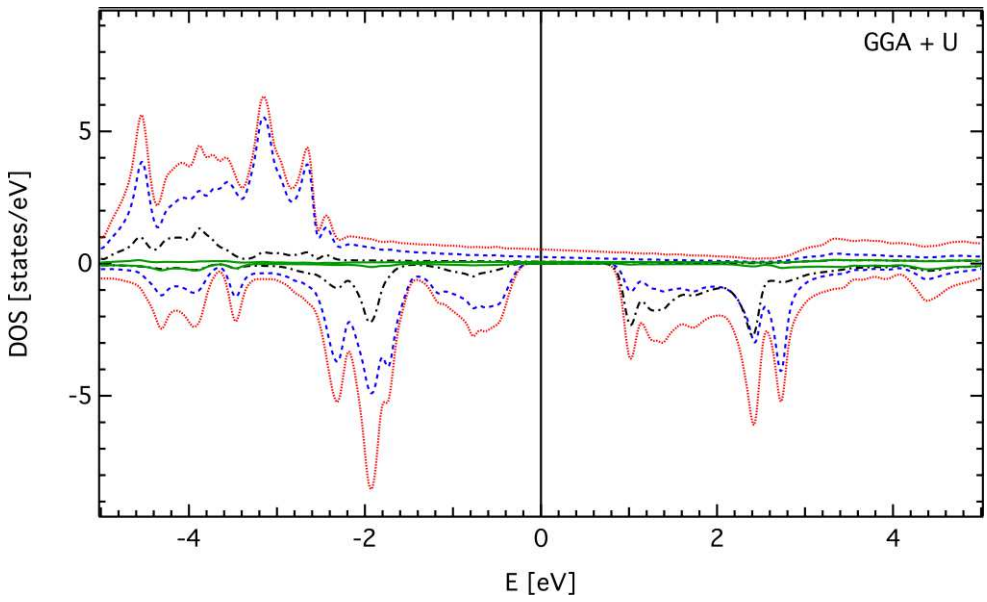

Figure 7.4: Calculated density of states of Co_2FeSi by GGA+U[58].

In the model there are five optical transitions described by Lorentz oscillators and free electron contribution described by Drude term that define optical properties of investigated samples. Resistivity in Drude term slightly increases with higher concentration of iron, but stays at same level of magnitude. The strongest transition is situated out of measured energies in infrared (IR) region at around 0.7 eV. The energy of this transition is shifting towards smaller energy

side with increasing concentration of iron as well as it is broadening. Energy of this transition is comparable with energy of the gap in the minority spin states. These observations are in agreement with *ab initio* calculations[58], which predict narrowing of the gap and small shifting of the Fermi level. Another significant change is in UV region between 5 and 6 eV. There are two transitions moving towards deeper UV and becoming stronger with increase of iron content. The last transition in measured spectral range is at about 1.5 eV and its amplitude has the strongest dependence on iron concentration. Therefore we can assume it corresponds to Co-Fe charge transition, which is in agreement with DOS calculations. The fifth transition is in deep UV far from measured energies. Therefore its values suffer to hight fitting error and we will not note them here.

In literature[57], there is usually used GGA model for *ab inito* calcualtions. However our observations have better agreement with models calculated by GGA+U[58].

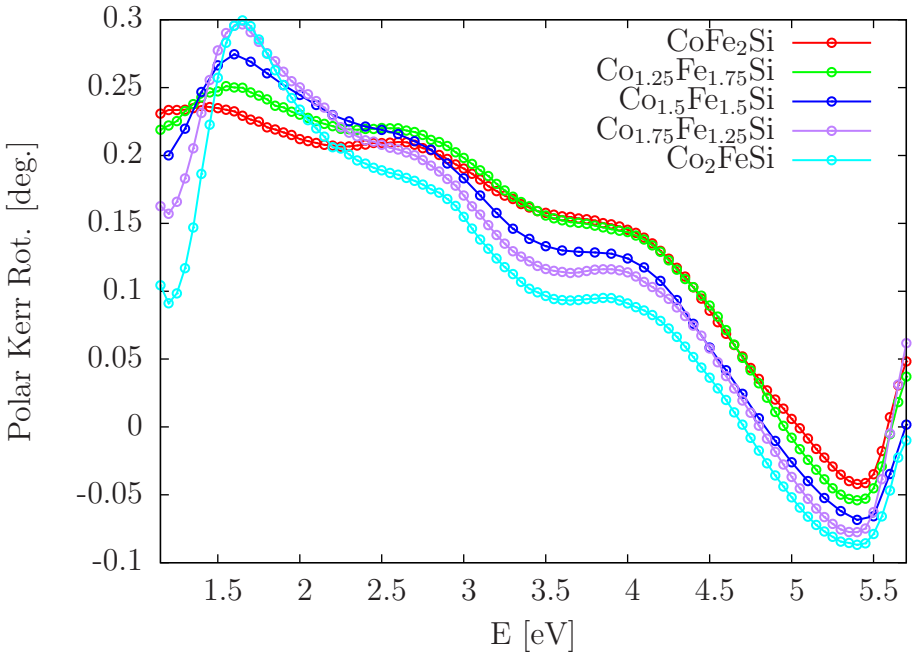

Figure 7.5: Polar Kerr rotation of Co-Fe-Si alloys.

7.1.3 Magneto-optical properties

Spectra of polar Kerr rotation and ellipticity are shown in Figs. 7.5 and 7.6. As in the case of optical properties, there is obvious contribution of free carriers, resulting in a smooth and almost monotonic spectral behavior. In addition there are visible three energy transitions at 1.6, 2.7 and 4.1 eV. There would probably be another transition in deep UV, but we are limited by spectral range of our setup. Ellipticity data are in agreement with Kramers-Krönig (KK) relations[52], which means that Kerr rotation has as inflex point where Kerr ellipticity has maximum. Two alloys with the lowest concentration of cobalt have similar MO properties whereas the other ones show significant difference, especially in UV region of ellipticity.

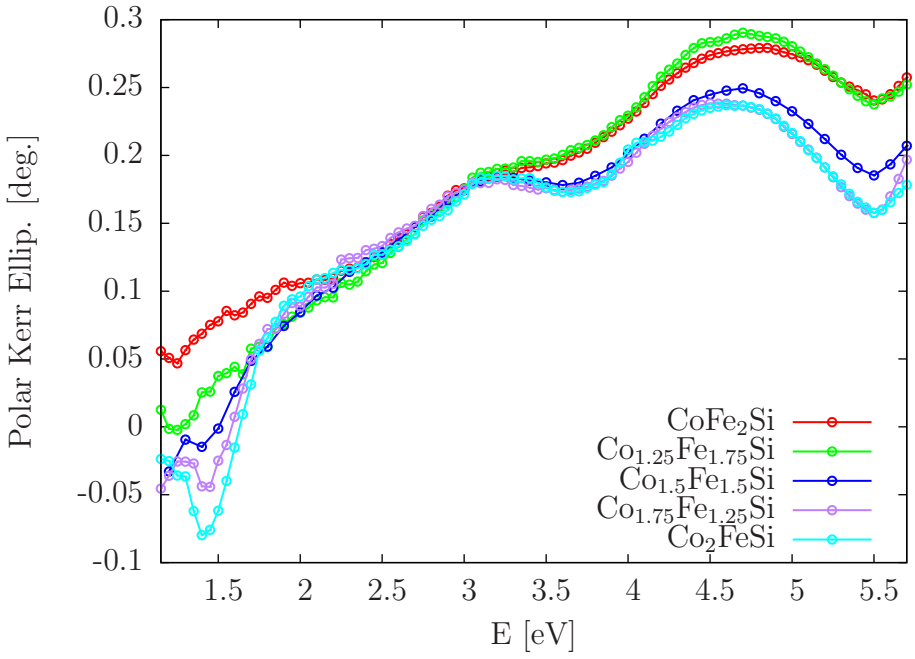

Figure 7.6: Polar Kerr ellipticity of Co-Fe-Si alloys.

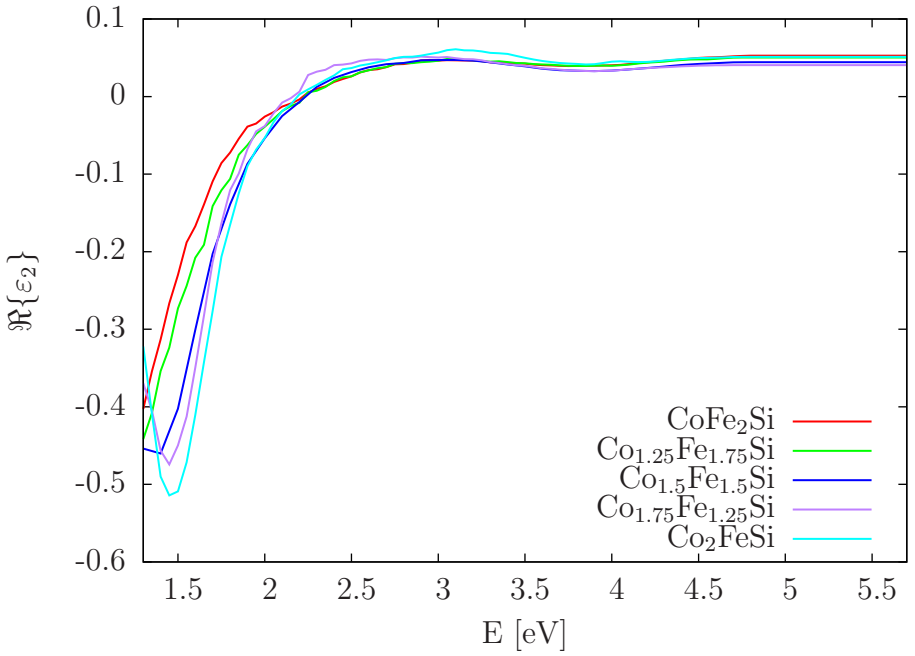

Figure 7.7: Calculated real part of off-diagonal component of permittivity tensor of Co-Fe-Si alloys.

7.1.4 Off-diagonal elements

With use of Yeh formalism and knowledge of the sample structure acquired from ellipsometry, we made point-by-point calculations of off-diagonal elements of permittivity tensor. The results are shown in Figs. 7.7 and 7.8. These data are in agreement with transitions observed in magneto-optical and ellipsometric measurements. In VIS and UV regions, real parts of off-diagonal elements of

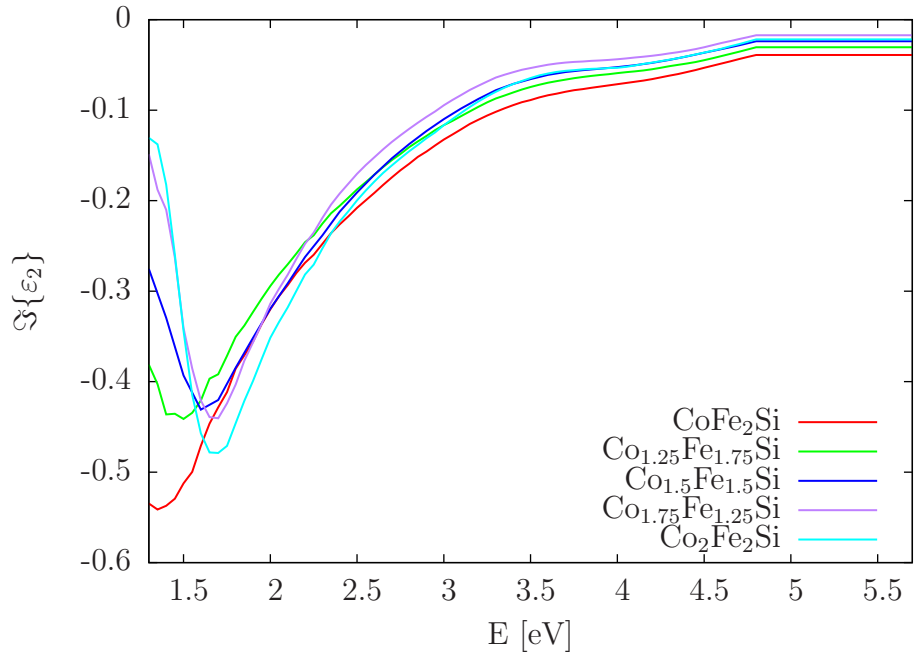

Figure 7.8: Calculated imaginary part of off-diagonal component of permittivity tensor of Co-Fe-Si alloys.

permittivity tensor are similar for all alloys. That means changes in magneto-optical spectra in this spectral range are caused mostly by change of optical properties. Changes in IR region are in agreement with our suggestion that the gap in the minority states is narrowing and the Fermi level is slightly shifting.

Imaginary part is in agreement with KK relations and we can observe smooth change with concentration of iron in area above 2 eV, which is in agreement with change of conductivity of studied samples.

7.1.5 Full-Heulser to Inverse-Heusler transformation

Change of optical and mangeto-optical properties of this set of samples is mostly due to continuous transformation from Full-Heusler in case of Co_2FeSi to Inverse-Heusler in case of $CoFe_2Si$. Fig. 7.9 shows the dependence of polar Kerr effect as a function of cobalt content. It is notable that MO Kerr effect is increasing in area around 1.6 eV while it decreases around 2.7 and 4.1 eV. It was already mentioned that decrease in IR region can be explained by the shift of the Fermi level and narrowing of the gap in the minority spin states.

Change of magneto-optical Kerr effect in the rest of spectra can be addressed to changes of concentration of free carriers.

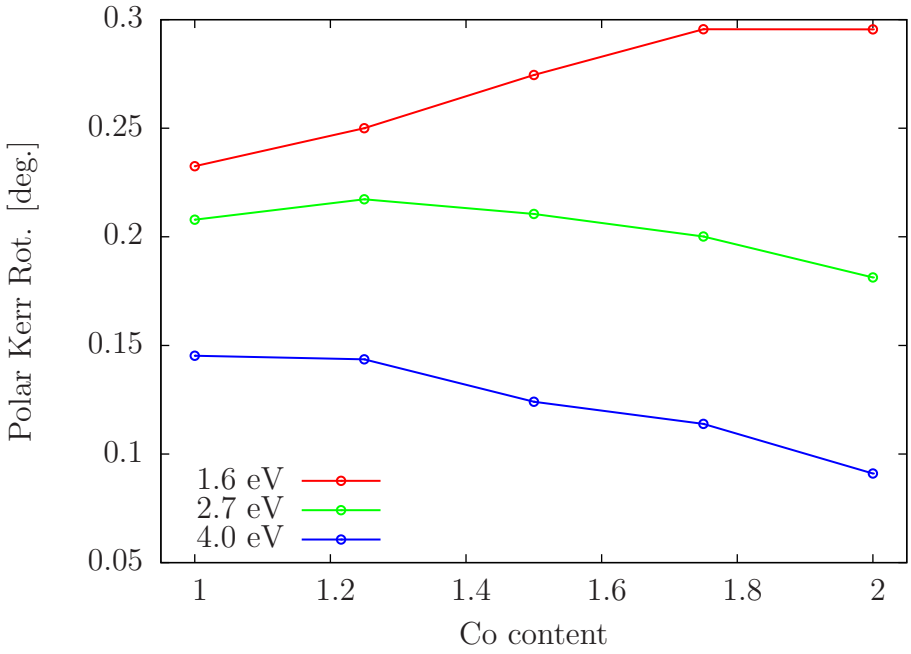

Figure 7.9: Dependence of polar Kerr rotation on Co content in Co-Fe-Si alloys.

7.2 NiMnGa

The second material, Ni-Mn-Ga, was studied because it undergoes temperature induced martensitic transformation. It was a Ni-Mn-Ga alloy bulk monocrystal. This material exhibits large (up to 12%) and relatively fast straining in a moderate magnetic field less than 1 T. The macroscopic deformation is due to magnetically induced structural reorientation (MIR) of martensite. Propagation of twin boundaries reorients the non-cubic lattice by about 90° that is driven by stress or magnetic field. This results in macroscopic strain. This ability is highly affected by mobility of twin boundaries as the magnetic energy is limited.

The single-crystal $Ni_{50.1}Mn_{28.4}Ga_{21.5}$ was cut approximately along the (100) planes of parent cubic austenite. The size of crystal was 0.9 x 2.4 x 20 mm^3. Surface was first mechanically polished and then electropolished to remove the layer affected by mechanical polishing, resulting in high-quality surface. During cooling, austenite phase transforms to martensite at 318 K. Backward transformation occurs at 330K. Ferromagnetic Curie temperature is about 373 K. At ambient temperature the structure of the material is modulated 10M martensite. For optical and magneto-optical measurements the lattice can be considered pseudo-tetragonal with c<a. The short c-axis is easy axis of magnetization.

7.2.1 X-ray diffraction

X-ray diffraction experiments have been done by the method of reciprocal space mapping using the CuKα line. The configuration was following: 1/4 divergence slit, soller slit 0.02 and the Bartels monochromator on the primary beam and detector on secondary beam[59].

On this sample, nine reciprocal space maps were measured. One on them is depicted in Fig. 7.10. One can see that there are more maxima present. It cor-

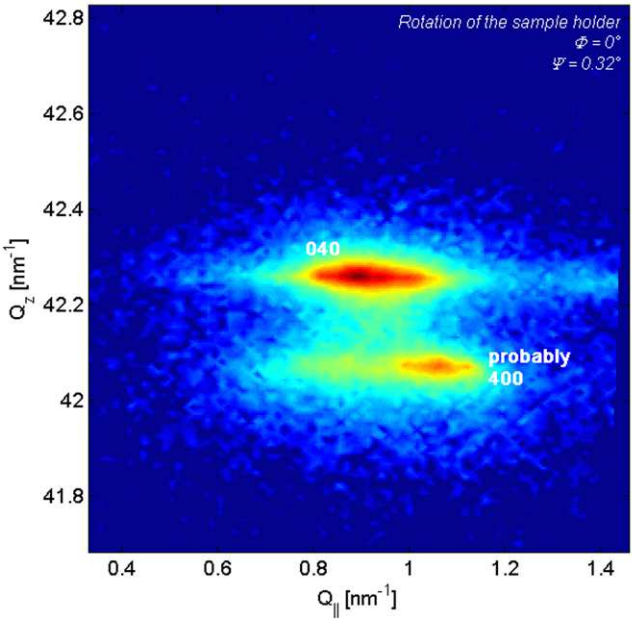

Figure 7.10: Reciprocal space map of Ni-Mn-Ga in area around one of major peaks.

responds to twinning structure of this sample. Lattice parameters of martensite structure at room temperature were obtained

$$a = (5.971 \pm 0.002)\text{Å}, \tag{7.1}$$
$$b = (5.9467 \pm 0.0007)\text{Å}, \tag{7.2}$$
$$c = (5.586 \pm 0.002)\text{Å}, \tag{7.3}$$
$$\alpha = \beta = 90°, \tag{7.4}$$
$$\gamma = (90.35 \pm 0.01)°. \tag{7.5}$$

As noted above, it corresponds to monoclinic structure that can be seen as pseudo-tetragonal. Austenite lattice parameters were

$$a = b = c = (5.963 \pm 0.002)\text{Å}, \tag{7.6}$$
$$\alpha = \beta = \gamma = 90°. \tag{7.7}$$

7.2.2 Domain structure

Magnetic domain structure was studied by two different methods. Fig. 7.11 displays their simple imaging by magneto-optical indicator. Observed labyrinth domain structure demonstrates high magnetic anisotropy with magnetization out of plane, perpendicular to the surface and parallel to crystallographic orientation of tetragonal short c-axis. This method gives only core features of the domain structure, because magneto-optical indicator is affected by the stray field above the sample in relatively large distance. Therefore magnetic force microscopy (MFM) measurement was done in approximately same area of the sample (Fig. 7.11). This measurement revealed more details in the structure of magnetic domains, however labyrinth-like structure remains.

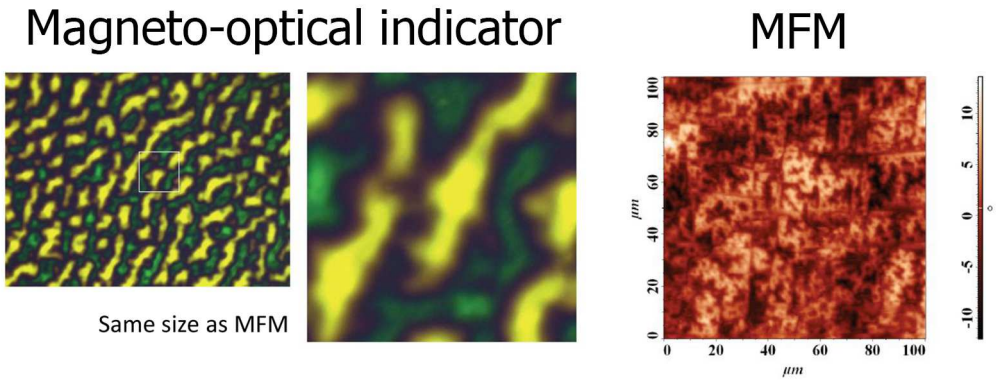

Figure 7.11: Domain structure of Ni-Mn-Ga measured by optical indicator and MFM.

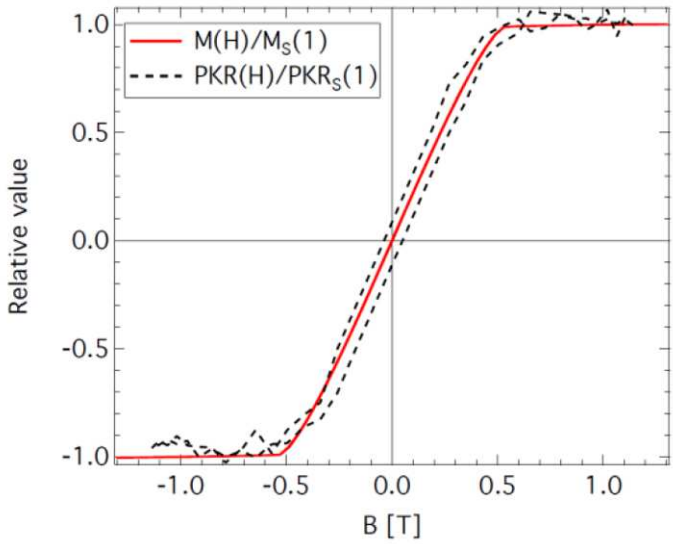

Figure 7.12: Magnetization loops of Ni-Mn-Ga measured by VSM and MO.

7.2.3 Magnetization loops

We have obtained magnetization loops by both, vibrating sample magnetometer (VSM) and polar Kerr MO mesurements (Fig. 7.12). They both confirmed that magnetization easy-axis is out of plane and the sample contains single variant with single magnetization, as the curves are measured along shortest sample dimension. From smoothness of curves we can conclude that there are no microstructural changes and thus no reorientation takes place during measurement. This also supports that our sample contains only single martensite variant with easy axis along the magnetic field. MO measurements in polar geometry shows same slope of magnetization. However we observed higher coercivity, which can be explained by higher concentration of impurities at the surface, since MO is more surface sensitive.

Temperature dependent VSM measurement of magnetization were also done on the sample. These results are shown in Fig. 7.13. On this Fig. one can see effect of martensitic transformation on magnetic properties. Significant step in magnetic properties occurs when alloy transform from martensite to austenite

and vice versa. One can also notice hysteresis of almost 20°C.

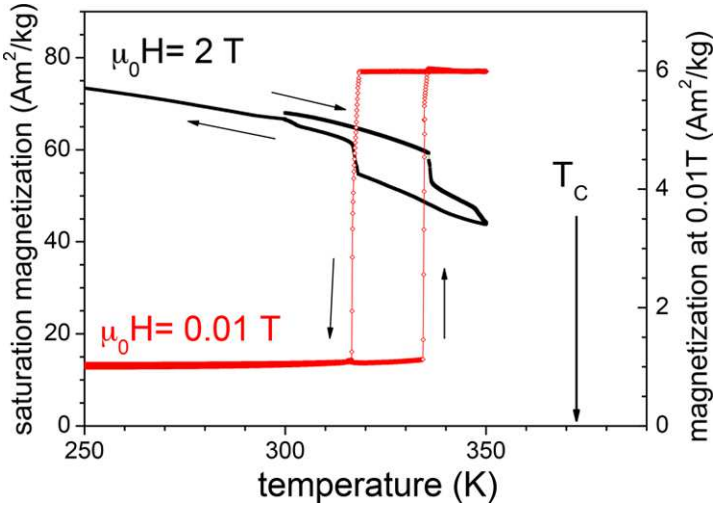

Figure 7.13: Temperature dependencies of magnetic properties of Ni-Mn-Ga alloy.

7.2.4 Spectroscopic ellipsometry

We have measured ellipsometric parameters Ψ and Δ at different temperatures. From them we derived values of diagonal element of permittivity tensor which are shown on figures 7.14 and 7.15. These measurements revealed two peaks at energies 1.8 eV and 3.2 eV. Fig. 7.16 shows temperature dependence of optical constants for energy 3.5 eV. Huge jump in this dependence is due to the martensitic transformation.

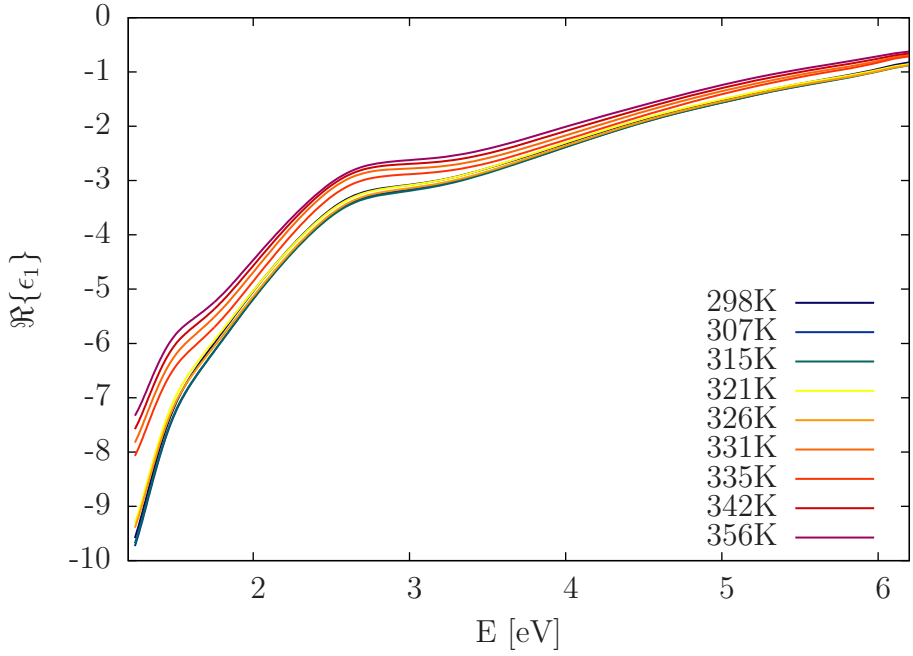

Figure 7.14: Real part of diagonal element of permittivity tensor of Ni-Mn-Ga during heating up.

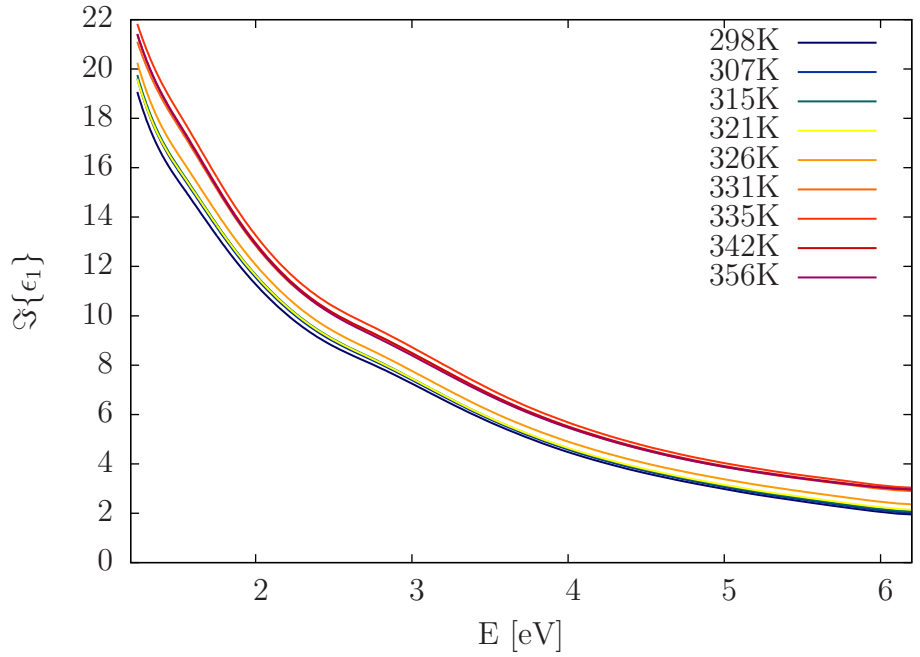

Figure 7.15: Imaginary part of diagonal element of permittivity tensor of Ni-Mn-Ga during heating up.

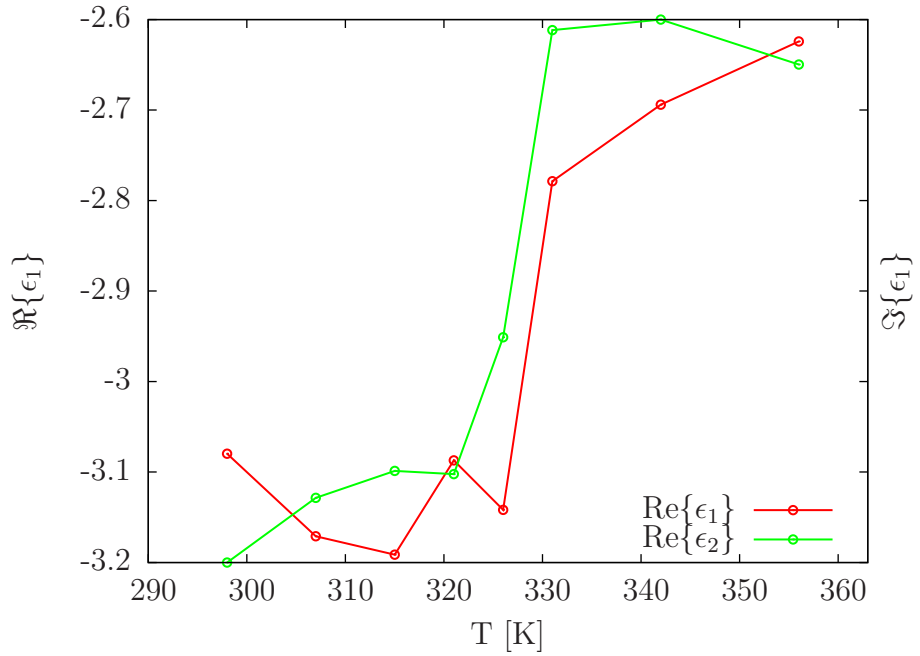

Figure 7.16: Temperature dependence of diagonal element of permittivity tensor of Ni-Mn-Ga at 3.5 eV.

7.2.5 Magneto-optical properties

Room temperature polar Kerr rotation spectrum measured at nearly normal incidence is displayed in Fig. 7.17. The spectrum exhibits features typical for Mn-containing materials[26]. Low level of noise in whole spectral range indicates good quality of the surface and high reflectivity. Most significant features of Kerr

rotation spectrum are two bands with opposite signs located near 1.6 eV and 3.8 eV. We also observe smaller broadening in IR region than in UV. These results are also consistent with previous reports on polycrystalline bulk samples.[61, 62] Slight shift of band in UV region can be caused by Mn excess. This excess of Mn atoms, which occupy non-stoichiometric positions can also explain observed broadening of UV band.

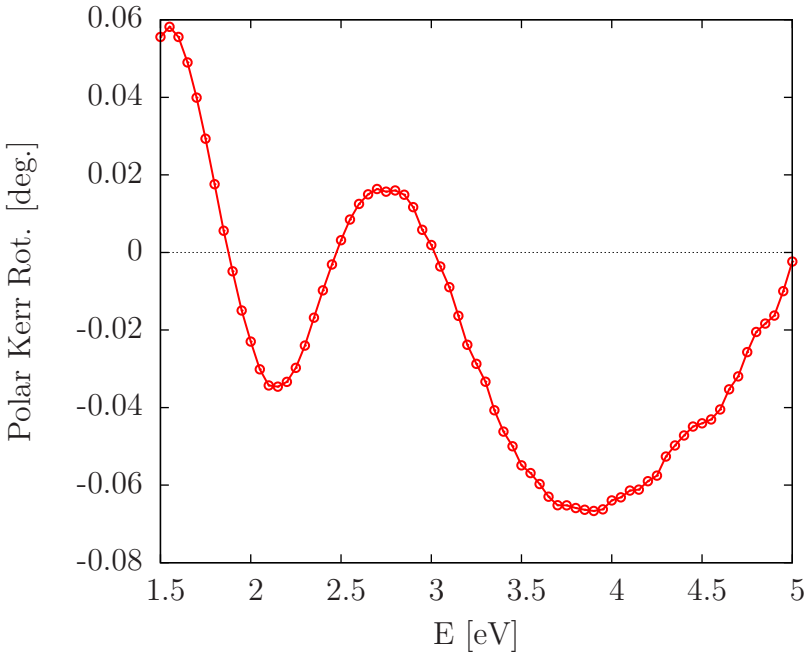

Figure 7.17: Polar Kerr rotation of Ni-Mn-Ga alloy at room temperature.

In cubic Ni_2MnGa the Fermi energy lies in a valley of antibonding minority-spin *3d* states[59]. That is not energetically advantageous. Therefore system undergoes a martensitic transformation to the tetragonal phase. This structure is stabilized by forming of the gap in the minority-spin *3d* states of Ni around Fermi energy (band Jahn-teller effect). According to *ab-initio* calculations, the gap-like formation in the t_{2g} minority-spin density of states for the tetragonal structure has the energy about 1.6 eV. The antibonding t_{2g} states lies about 0.3 eV above the Fermi energy, while the bonding Ni t_{2g} states along with Ni e_g states lie about 1.3 eV below the Fermi energy. This gives a gap of 1.6 eV, which corresponds to the position of spectroscopic band in our data. That would point to Ni *3d* states to be responsible for magneto-optics in infra-red region.

On the other hand, Mn *3d* states are localized at about 1.3 eV above the Fermi energy, white Ni t_{2g} states are broadly located within 1.3 to 3.5 eV below the Fermi energy, respectively. That means magneto-optical effect in UV region could be caused by Ni-Mn transitions. This molecular orbital picture is just an rough approximation and a more sophisticated theoretical models are needed to validate our assignments.

7.2.6 Martensitic transformation

Results of measurements of temperature dependence of polar Kerr effect are shown in Fig. 7.18. There is clearly visible effect of martensitic transformation.

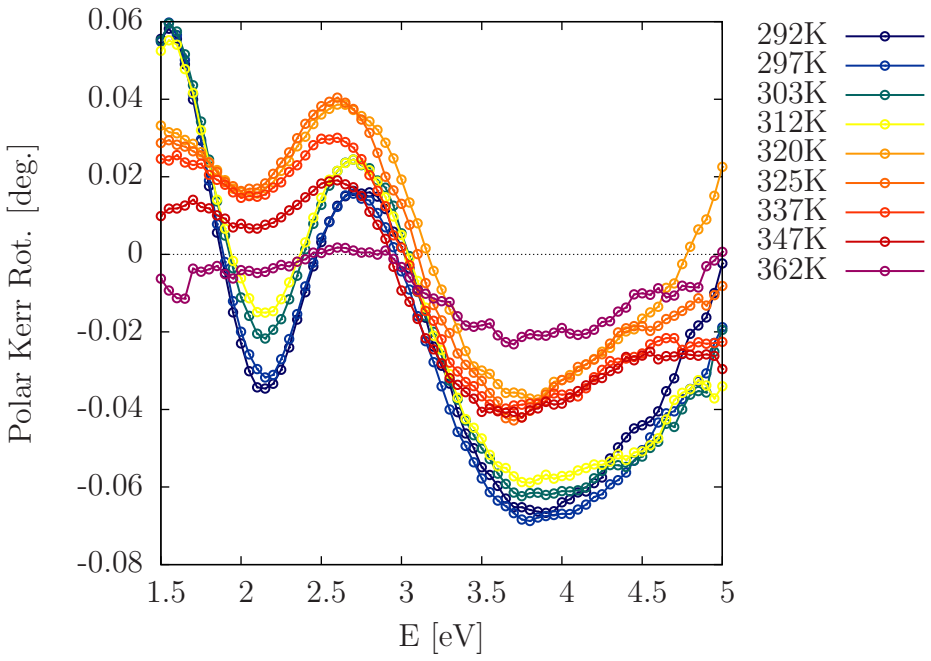

Figure 7.18: Polar Kerr rotation evolution of Ni-Mn-Ga during heating up.

The most significant is the change of sign of magento-optical effect in area between 2 and 3 eV. This change is even more visible in Fig. 7.19 where one can see temperature dependent polar Kerr rotation at various energies. The change in the sign of the real part of dielectric function in Ni_2MnGa was also observed in this energy range [63].

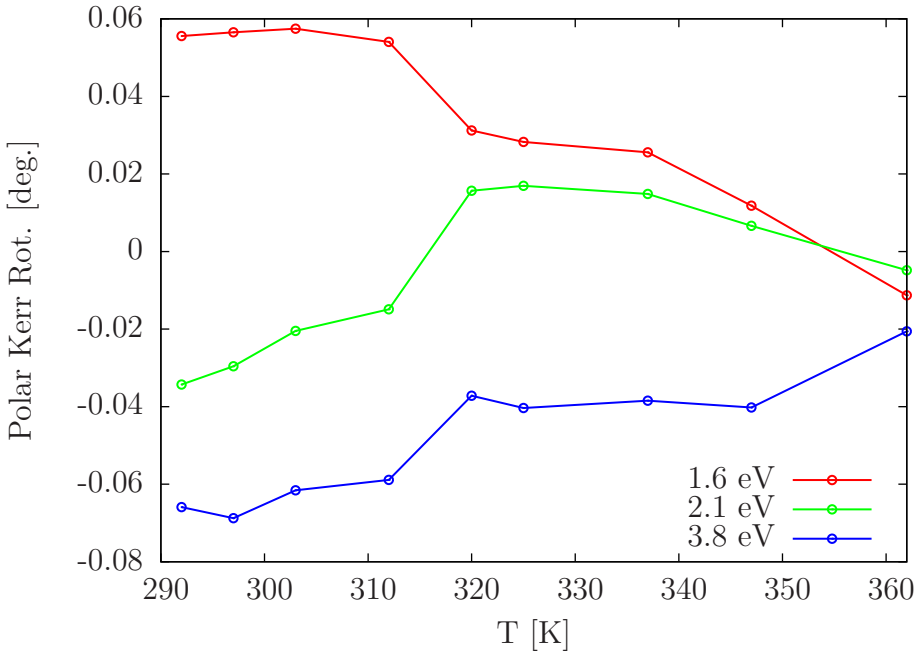

Figure 7.19: Temperature dependence of polar Kerr rotation at various energies.

In austenite phase, both Ni t_{2g} and e_g states are shifted to higher energies, resulting in a valley of antibonding minority-spin *3d* states at the Fermi energy.

However, the energy gap between different Ni *3d* states remains approximately the same as well as the energy of localized Mn *3d* states. This suggests that change of the sign of polar Kerr rotation is most likely due to change of optical properties, because the magneto-optical signal is dominated not only by the spectrum and bulk content of the ferromagnetic component, but by the optical properties of the alloy as well. At higher temperatures we can see decrease of amplitude that is most likely due to approaching ferromagnetic Curie temperature.

7.3 $Mn_2Rh_xCo_{1-x}Sn$

Ternary compounds $Mn_2Rh_xCo_{1-x}Sn$ are ferromagnets, whose magnetism origins from interaction of Mn with Y elements. Structural transformation in these alloys occurs when concentration of Rh decreases bellow the value of 0.5. In that situation cubic Full-Heusler transforms into tetragonal compound. Schemes of these alloys can be seen in Fig. 7.20. This transformation points to presence of strain, which is stronger in tetragonal alloys. Concentration of Rh has great influence on other properties like ferromagnetic Curie temperature which can be seen in Fig. 7.21.

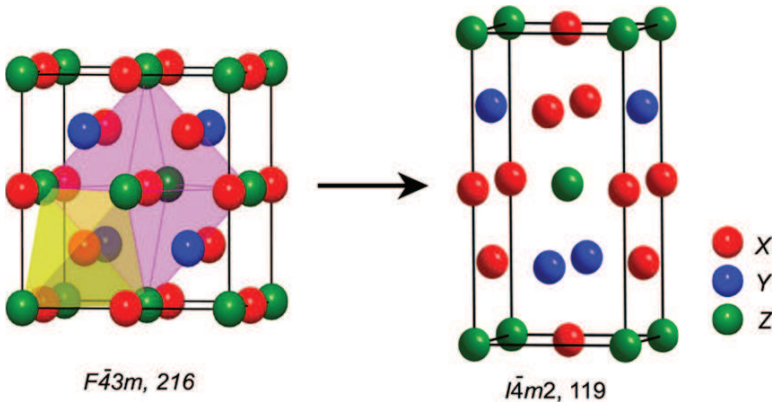

Figure 7.20: Scheme of structural transformation occuring in $Mn_2Rh_xCo_{1-x}Sn$.

Studied samples were prepared by arc-melting of stoichiometric volumes of present elements. Afterwards, the samples were annealed in argon atmosphere at 700 °C. After the preparation, the samples we sliced and polished for optical measurements. Due to the strain in these compounds, we were not able to obtain hight quality surface. Resulting amount of roughness caused high depolarization in optical measurements, especially in the UV region. Therefore measurements in this spectral range suffer for high measurement error and high level of noise.

7.3.1 XRD measurements

Powder diffraction was used to obtain crystallographic structure and lattice parameters of these alloys. These measurements confirmed the transformation from tetragonal to cubic structure with increase of Rh content.

Energy-dispersive X-ray spectroscopy (EDAX) measurements were done to determine exact relative concentrations of the elements in studied samples. The

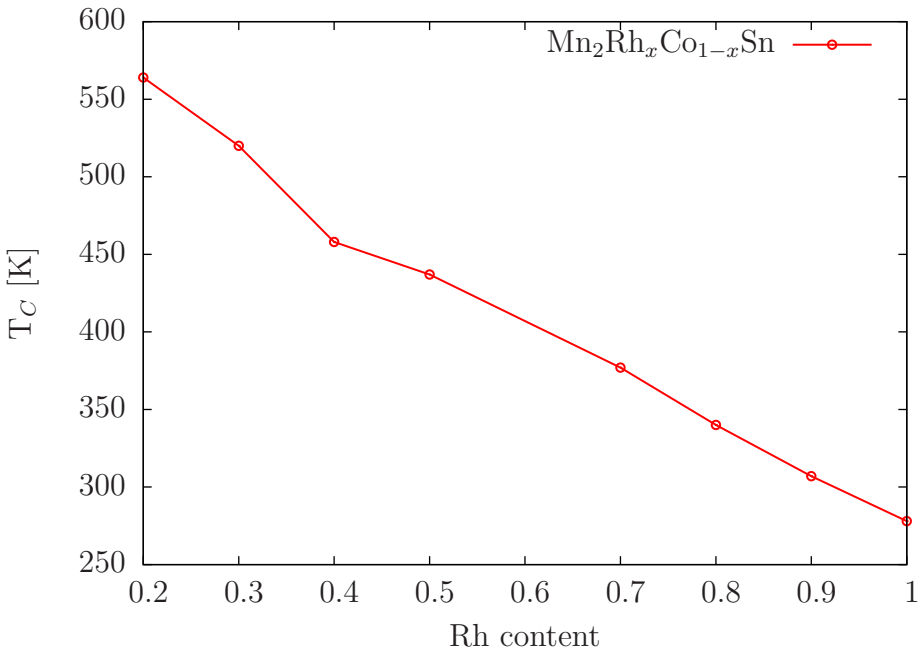

Figure 7.21: Dependence of Curie temperature of $Mn_2Rh_xCo_{1-x}Sn$ on Rh content.

results are listed in table 7.2. There was also trace amount of Oxygen and Silicon in all samples.

As it was mentioned, the origin of magnetism in these alloys is connected with Mn atoms. That is good to keep in mind for further magneto-optical studies, because there will be visible correlation between MO effect and amount of Mn in the alloy.

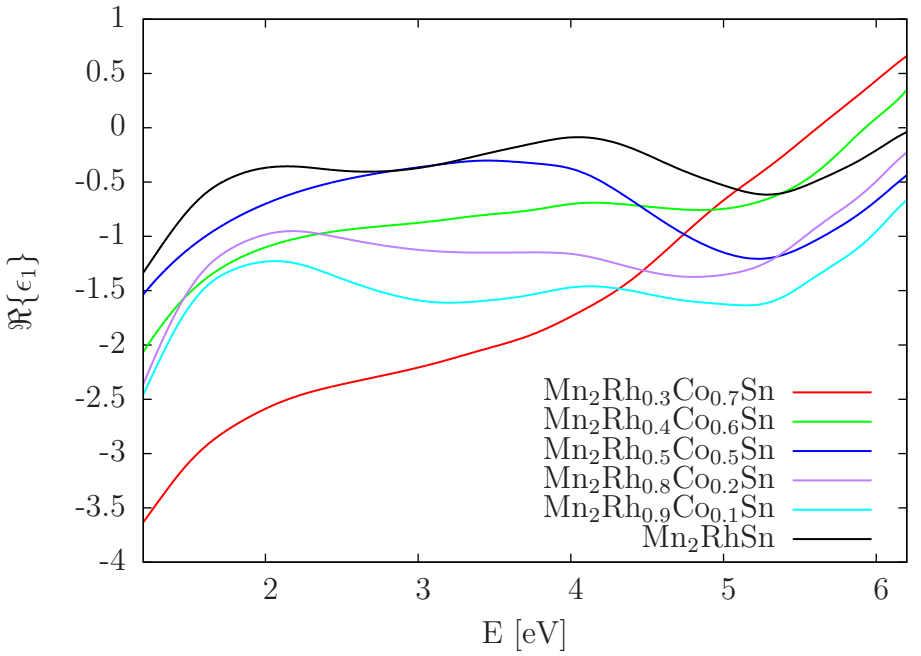

Figure 7.22: Real part of diagonal element of permittivity tensor of $Mn_2Rh_xCo_{1-x}Sn$ alloys.

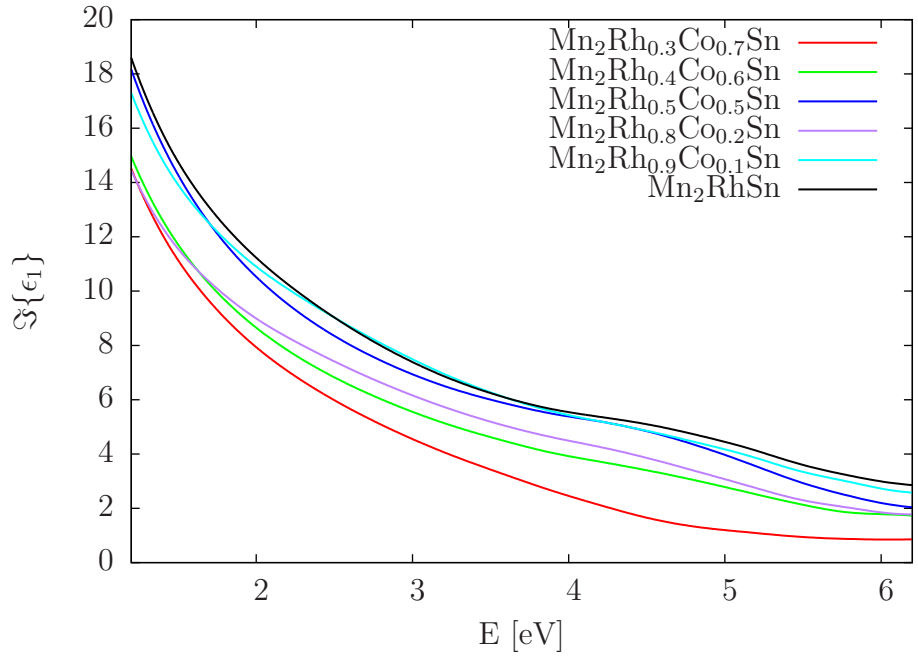

Figure 7.23: Imaginary part of diagonal element of permittivity tensor of $Mn_2Rh_xCo_{1-x}Sn$ alloys.

7.3.2 Optical properties

Obtained spectral dependences of optical properties are shown in Figs. 7.22 and 7.23. Model used for fitting of ellipsometric data was bulk structure with thin Mn oxide on top. There seems to be no notable dependence in optical properties connected just to stoichiometry of samples. That is probably due to the large difference in strains, which has much more significant influence on optical properties than Rh to Co ratio. There are three noticeable bands around 1.8, 4.2 and 7 eV in addition to contribution of free electrons. Transition in UV region seems to be way stronger at tetragonal alloys.

Interesting fact is that for the tetragonal alloys the real part of permittivity goes above zero in UV region. This property might have great use in area of plasmonics, but could be also caused by high noise in this spectral range.

7.3.3 Magneto-optical properties

Measured magneto-optical spectra are shown in Figs. 7.24 and 7.25. We can observe decrease of MO Kerr rotation with increase of Rh content. This influence seems to saturate around the concentration of Rh at 0.7. Ellipticity does not seem to follow this dependence, however there is still obvious correlation due to similar change of monotony of rotation and ellipticity. The dependence of polar Kerr effect on Rh content at 2.5 eV is shown in Fig. 7.26. This observation is in agreement with higher Kerr effect in Co-based alloys connected with higher spin-orbital interaction, but more effects seems to be in play. We can observe a correlation between the amplitude of the Kerr effect and Mn content as well as the decrease of the amplitude when reaching ferromagnetic Curie temperature. A contribution to deformation of band structure connected to the lattice strain

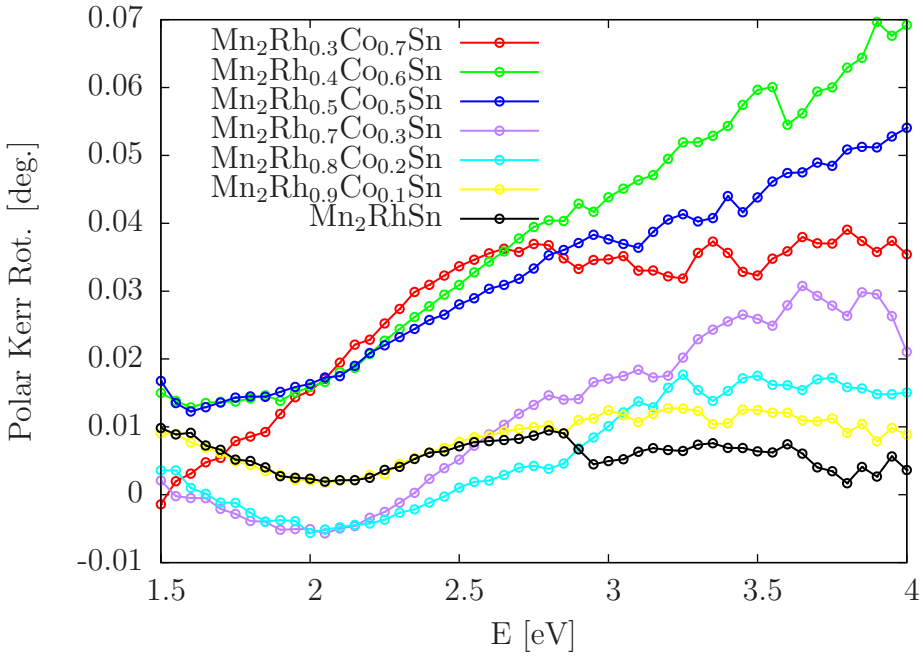

Figure 7.24: Polar Kerr rotation of $Mn_2Rh_xCo_{1-x}Sn$ alloys.

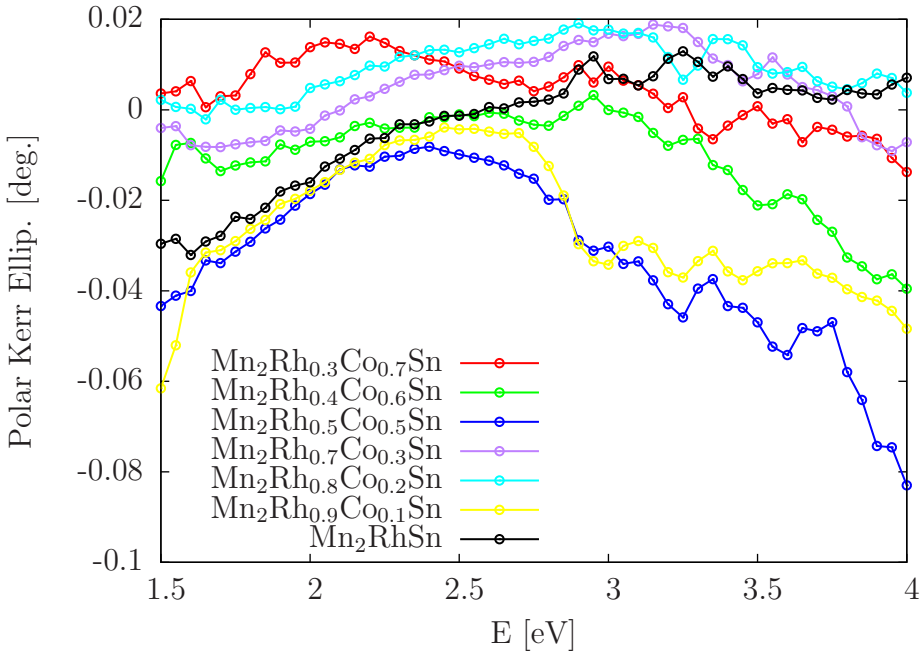

Figure 7.25: Polar Kerr ellipticity of $Mn_2Rh_xCo_{1-x}Sn$ alloys.

cannot be neglected.

7.3.4 Off-diagonal elements of permittivity tensor

We used measured MO Kerr spectra and acquired optical constants to calculate off-diagonal elements of the permittivity tensor. Results of this procedure are shown in Figs. 7.27 and 7.28. Since these values are calculated from previous

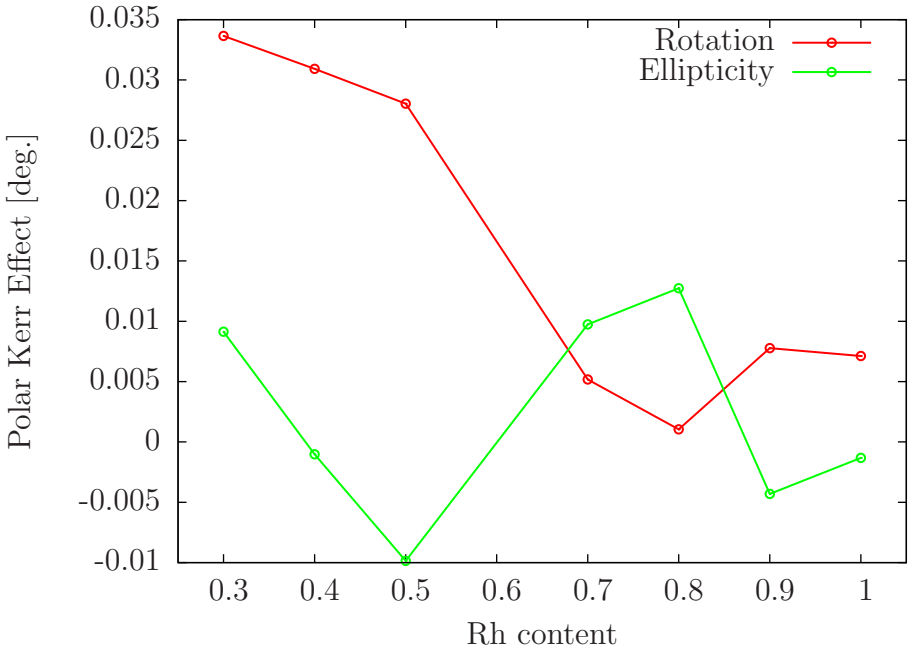

Figure 7.26: Dependence of Kerr Effects of $Mn_2Rh_xCo_{1-x}Sn$ on Rh content at 2.5 eV.

data, they have same character. Once again there is no obvious dependence on stoichiometry.

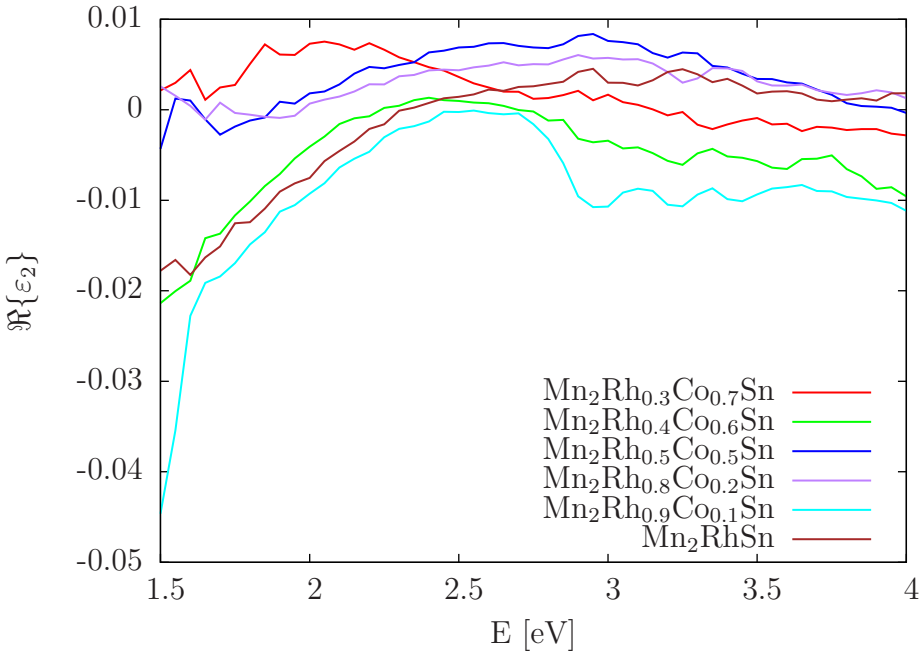

Figure 7.27: Calculated real part of off-diagonal element of permittivity tensor of $Mn_2Rh_xCo_{1-x}Sn$.

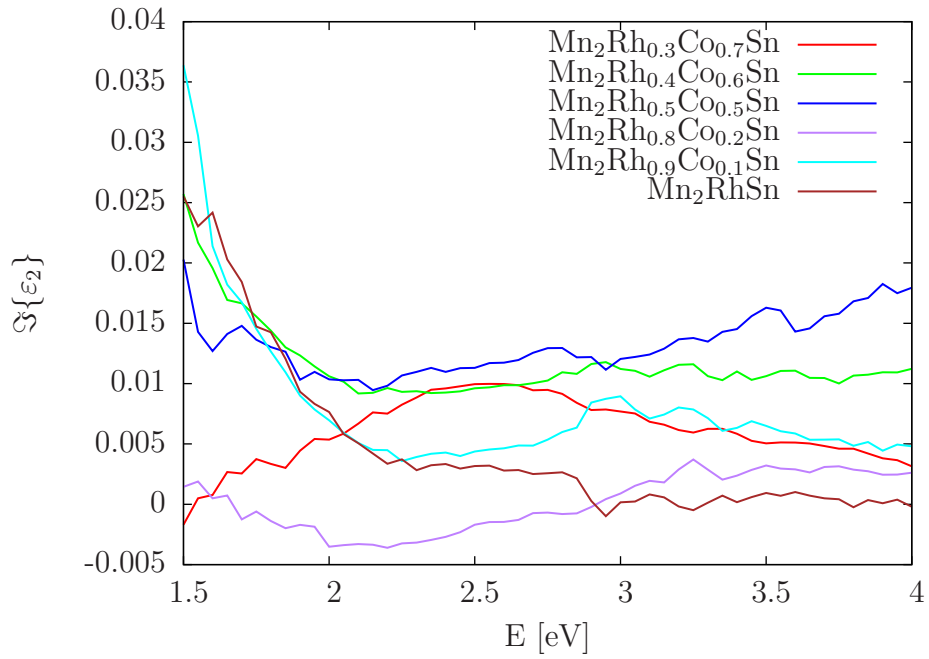

Figure 7.28: Calculated imaginary part of off-diagonal component of permittivity tensor of $Mn_2Rh_xCo_{1-x}Sn$.

x	3	4	5	7	8	9	10
Co	14.11	12.04	9.20	5.56	3.93	1.85	0.01
Mn	34.94	34.59	32.70	32.01	33.13	32.26	32.74
Rh	10.15	13.01	16.90	22.15	24.96	27.66	28.93
Sn	40.23	39.69	39.70	38.60	37.45	36.76	37.56

Table 7.2: Compositions of Co-Mn-Rh-Sn alloys obtained from EDAX.

7.3.5 Effect of structural transformation

We have observed features on spectra pointing to change of these properties due to structural transformation. However due to many stronger effects in play, we cannot come with any conclusion in this matter. Elimination of disturbing effects would require samples with higher quality. That could be achieved by additional post-deposition treatment of the samples.

Conclusion

The aim of this thesis was systematic study of physical properties of various Heusler alloys. We focused especially on changes in their optical and magneto-optical properties due to structural transformations in these alloys. At the beginning we introduced general properties of Heusler alloys, described progress in study of these materials and noted some of their applications.

In theoretical chapters we introduced various ways how to describe the interaction of light with matter and formalism used for the description of propagation of light through various systems. These formalism were used later for theoretical calculations of optical and magneto-optical response of studied samples, which were confronted with experimental results to obtain important information about changes in electronic structure of material, which undergoes the structural transformation. At the end, we explained concepts of experimental methods used for study of our samples.

In experimental part, we studied physical properties of three different types of Heusler alloys.

First studied compounds were Co-Fe-Si alloys which draw our interest because of their half-metallic character, large magnetic moment and hight Curie temperatures way above room temperature. These compounds exhibited structural transformation with change of Fe-Co ratio from Full-Heusler in case of Co_2FeSi to Inverse-Heusler in case of $CoFe_2Si$. We managed to address changes in optical properties to changes in DOSs. Optical properties of these alloys were determined mostly by concentration of free carriers and by size of the bang gap in the minority spin states. Increase of conductivity and narrowing of the gap was observer not only in optical measurements, but in the magneto-optical measurements as well. At the end we compared our conclusions with *ab initio* calculations where we found good agreement, especially with GGA+U model.

The second studied alloy was Ni-Mn-Ga. This alloy was interesting for its martensitic transformation from high temperature cubic austenite to low temperature tetragonal martensite. We started with probing of stuctural properties of our monocrystallic sample, which confirmed presence of variants in martensitic structure. Magnetic measurements confirmed magnetic anisotropy of the compound and were in agreement with observed domain structure at the surface of the sample. Temperature dependent measurements of optical and magneto-optical properties exhibited significant step within of the transformation, which was explained by changes of the band structure in the vicinity of the Fermi energy that occur during the transformation. Changes of magneto-optical Kerr effect were addressed to changes of optical properties. Finally, approximative picture of mechanism behind martensitic transformation was proposed.

The last studied sets of samples were Mn-Rh-Co-Sn. X-ray measurements confirmed structural transformation from cubic to tetragonal symmetry with change of Rh content. However, no visible dependences in optical and magneto-optical properties were observed. These results were explained by large amount of strain that differs among alloys and had significant effect on optical and magneto-optical properties of studied samples.

Bibliography

[1] Heusler, F, Starck W, Haupt E
Verh DPG, **5** (1903), pp. 220-223

[2] Felser C, Fecher GH, Balke B
Spintrocnics: A challenge for materials science and solid-state chemistry
Angew Chem IntEd, **46** (2007), pp. 668-699

[3] Spina L, Jia YZ, Ducourant B, Tillard M, Belin C
Compositional and structural variantions in the ternary system Li-Al-Si
ZKristallogr, **218** (2003), pp. 740-746

[4] Chadov S, Qi X, Kübler J, Fecher GH, Felser C, Zhang SC
Tunable multifunctional topological insulators in teranry Heusler compounds
Nature Materials **9**, 541-545 (2010)

[5] Klimczuk T, Wang CH, Gofryk K, Ronning F, Winterlik J, Fecher GH, Griveau JC, Colineau E, Felser C, Thompson JD, Safarik DJ, and Cava RJ
Superconductivity in the Heusler family of intemetallics
Phys Rev B **85**, 174505

[6] Puselj M, Ban Z
The Crystal Structure of $TiCuHg_2$
Croat Chem Acta, **41** (1969), pp. 79-83

[7] Villars P., Calvert LD.
Pearson's handbook of crystallographic data for intermetallic phases.
American Society of Metals; 1991.

[8] Bradley AJ, Rodgers JW.
Crystal Structure of the Heusler Alloys.
Proc Roy Soc A, **144** (1934), pp. 340-359

[9] Butler WH, Mewes CKA, Liu C, Xu T.
arXiv:1103.3855v1.

[10] Bacon GE, Plant JS.
Chemical ordering in heusler alloys with the general formula A_2BC or ABC
J Phys F Met Phys, **1** (1971), pp. 524-532

[11] Miura Y, Nagao K, Shirai M
Atomic disorder effects on half-metallicity of the full-Heusler alloys $Co_2(Cr_{1-x}Fe_x)Al$: A first-principles study. Phys Rev B **69**, 144413 (2004)

[12] Wurmehl S, Kandpal HC, Fecher GH, Felser C
Valence electron rules for prediction of half-metalllic compensated-ferrimagnetic behaviour of Heusler compounds with complete spin polarization
J Phys Condens Matter, **18** (2006), pp. 6171-6181

[13] Özdogan K, Aktas B, Sasnoglu E, Galanakis I
Doping and disorder in the Co_2Mnal and Co_2MnGa half-metallic Heusler alloys
Phys Rev B **74**, 172412

[14] de Groot RA, Mueller FM, van Engen PG, Buschow KHJ,
New class of materials: Half-metallic ferromagnets
Phys Rev Lett, **50** (1983), p. 2024

[15] Ishida S, Akazawa S, Kubo Y, Ishida J
Band theory of Co_2MnSn, Co_2TiSn and Co_2TiAl
J Phys F: Met Phys **12**, 1111 (1982)

[16] Min-guang Z, Gui-ru B, Huei-chang J
d-orbital theory for Mn^{3+}-complex ions in crystals
J Phys C: Solid State Phys. **15**, 5959

[17] Ksenofontov V, Herbort C, Jourdan M, Felser C
Conversion electron Mössbauer spectroscopy of epitacial $Co_2Cr_{0.6}Fe_{0.4}Al$ thin films
Appl Phys Lett, **92** (2008), p. 262501

[18] Helmholdt RB, de Groot RA, Mueller FM, van Engen PG, Buschow KHJ,
Magnetic and crystallographic properties of several $C1_b$ type Heusler compounds
J Magn Magn Mater, **43** (1984), pp. 249-255

[19] Kübler J,
First principle theory of metallic magnetism
Physica B, **127** (1984), pp. 257-263

[20] Youn SJ, Min BI.
Effects of the spin-orbit interaction in Heusler compounds: Electronic structures and Fermi surfaces of NiMnSb abd PtMnSb
Phys Rev B, **51** (1995), pp. 10436-10442

[21] Galanakis I, Ostanin S, Alouani M, Dreysse H, Wills JM.
Ab initio ground state and $L_{2,3}$ x-ray magnetic circular dichroism of Mn-based Heusler alloys
Phys Rev B, **61** (2000), pp. 4093-4102

[22] Chadov S, Qi X, Kübler J, Fecher GH, Felser C, Zhang SC.
Tunable multifunctional topological insulators in ternary Heusler compounds
Nat. Mat, **9** (2010), pp. 541-545

[23] Kisker E, Carbone C, Flipse CF, Wassermann EF.
Photoemission of intermetallics
J Magn Magn Mater, **70** (1987), p.21

[24] Webster PJ, Ziebeck KRA
Alloys and Compounds of d-Elements with Main Group elements
New Series, Group III, Vol. 19/c
Springer, Berlin, 1988; 75-184

[25] Hanssen KEM, Mijnarends PE, Rabou LPLM, Buschow KHJ.
Positron-annihilation study of the half-metallic ferromagnet NiMnSb: Experiment
Phys Rev B, **42** (1990), pp. 1533-1540

[26] Antonov VN, Oppeneer PM, Yaresko AN, Perlov AY, Kraft T.
Computationally based explanation of the peculiar magneto-optical properties of PtMnSb and related ternary compounds
Phys Rev B, **56** (1997), pp 13012-13025

[27] Antonov VN, Yatesko AN, Ya Perlov A, Nemoshakalenko VV, Oppeneer PM, Eschring H.
Magneto-optical spectroscopy of d- and f-ferromagnetic materials: recent theoretical progress
Low Temp Phys, **25** (1999), p. 387

[28] Kumar M, Nautiyal T, Auluck S.
Full potential results on the magneto-optical properties of the Heusler compounds Co_2FeX (X = Al, Ga, Si and Ge)
J Phys Condens Matter, **21** (2009), p. 196003

[29] Webster J, Ziebeck KEA, Town SL, Peak MS.
Philos Mag B, **49** (1984), p. 295

[30] Baibich MN, Broto JM, Fert A, Nguyen Van Dau F, Petroff F, Etienne P, Creuzet G, Friederich A, Chazelas J
Gian Magnetoresistance of (001)Fe/(001)Cr Magnetic Supertlattices
Phys Rev Lett **61**, 2472 (1988)

[31] Tsunegi S, Sakuraba Y, Oogane M, Takanashi K, Ando Y
Large tunnel magnetoresistance in magnetic tunnel junctions using a Co_2MnSi Heusler alloy electrode and a MgO barrier
Appl Phys Lett **93**, 112506 (2008)

[32] Bowen M, Bibes M, Barthélémy A, Contour J-P, Anane A, Lemaite Y, Fert A
Nearly total spin polarization in $La_{2/3}Sr_{1/3}MnO_3$ from tunneling experiments
Appl Phys Lett **82**, 223 (2003)

[33] Sakuraba Y, Hattori M, Oogane M, Ando Y, Kato H, Sakuma A, et al.
Giant tunneling magnetoresistance in Co_2MnSi/Al-O/Co_2MnSi magnetic tunnel junctions
Appl Phys Lett, **88** (2006), p. 192508

[34] Marukame T, Ishikawa T, Hakamata S, Matsuda K-i, Uemura T, Arita M.
High spin-polarized tunneling in fully epitaxial $Co_2Cr_{0.6}Fe_{0.4}Al$ /MgO/$Co_{50}Fe_{50}$ magnetic tunnel junctions with exchange biasing
Appl Phys Lett, **90** (2007), p.012508

[35] Tsunegi S, Sakuraba Y, Oogane M, Takanashi K, Ando Y.
Large tunnel magnetoresistance in magnetic tunnel junctions using a Co_2MnSi Heusler alloy electrode and a MgO barrier
Appl Phys Lett, **93** (2008), p. 112506

[36] Yakushiji K, Saito K, Mitani S, Takanashi K, Takahashi YK, Hono K
Current-perpendicular-to-plane magnetoresistance in epitaxial Co_2MnSi/Cr/ Co_2Mnsi trilayers
Appl Phys Lett **88**, 222504 (2006)

[37] Nikolaev K, Anderson P, Kolbo P, Dimitrov D, Xue S, Peng X, Pokhil T, Cho H, Chen Y
Heusler alloy based current-perpendicular-to-the-plane giant magnetoresisitance heads for high density magnetic recording
J Appl Phys **103**, 07F533 (2008)

[38] Hernando A, Crespo P, Garcia MA, Pinel EF, de la Venta J, Fernandez A, Penades S
Giant magnetic anisotropy at the nanoscale: Overcoming the superparamegnetic limit
Phys Rev B **74**, 052403 (2006)

[39] Wu F, Mizukami S, Watanabe D, Naganuma H, Oogane M, Ando Y, et al.
Epitacial $Mn_{2.5}Ga$ thin films with giant perpendicular magnetic anisotropy for spintronic devices.
Appl Phys Lett, **94** (2009), p. 122503

[40] Ambrose T, Krebs JJ, Prinz GA.
Epitacial growth and magnetic properties of single-crystal Co_2MnGe Heusler alloy films on GaAs (001)
Appl Phys Lett, **76** (2000), p. 3280

[41] Hirohata A, Kurebayashi H, Okamura S, Kikuchi M, Masaki T, Nozaki T, Tezuka N, Inomata K
Structural and magnetic properties of epitacial $L2_1$-structured Co_2(Cr,Fe)Al films grown on GaAs(001) substrates J Appl Phys **97**, 103714 (2005)

[42] Nagao K, Shirai M, Miura Y
Ab initio calculations of spin polarizaation at Co_2CrAl/GaAs interfaces
J Phys: Confens Matter **16**, S5725

[43] Hickey MC, Damsgaard CD, Farrer I, Holmes SN, Husmann A, Hansen JB, Jacobsen CS, Ritchie DA, Lee RF, Jones C, Pepper

M
spin injection between epitaxial $Co_{2.4}Mn_{1.6}Ga$ and as InGaAs quantum well
Appl Phys Lett **86**, 252106 (2005)

[44] Dong C, Adelmann XY, Xie JQ, Palmstrøm CJ, Strand LXJ, Crowell PA, et al.
Spin injection from the Heusler alloy Co_2MnGe into $Al_{0.1}Ga_{0.9}As$/GaAs heterostructures
Appl Phys Lett, **86** (2005), p. 102107

[45] Sozinov A, Likhachev AA, Lanska N, Ullakko K.
Giant magnetic-field-induced strain in NiMnGa seven-layered martensitic phase
Appl Phys Lett, **80** (2002), p. 1746

[46] Kanomata T, Fukushima K, Nishihara H, Kainuma R, Itoh W, Oikawa K, et al.
Magnetic adn Crystallographic Properties of Shape Memory Alloys $Ni_2Mn_{1+x}Si_{1-x}$
Mater Sci Forum, **583** (2008), p. 119

[47] Brown PJ, Crangle J, Kanomata T, Matsumoto M, Neumann K-U, Ouladdiaf B, et al.
The crystal structure and phase transitions of the magnetic shape memory compound Ni_2MnGa
J Phys Condens Matter, **14** (2002), p. 10159

[48] Marcos J, Manosa L, Planes A, Casanova F, Batlle X, Labarta A.
Mutliscale origin of the magnetocaloric effect in Ni-Mn-Ga shape-memory alloys
Phys Rev B, **68** (2003), p.094401

[49] Takeuchi I, Famodu OO, Read JC, Aronova MA, Chang K-S, Craciunescu C, et al.
Identification of novel compositions of ferromagnetic shape-memory alloys using composition spreads
Nat Mater, **2** (2003), pp. 180-184

[50] Pötschke M, Gaitzsch U, Roth S, Rellinghaus B, Schultz L
Training, constraints, and high-cycle magneto-mechanical properties of Ni-Mn-Ga magnetic shape-memory alloys Eur Phys J Special Topics, **158** (2008), pp. 79-85

[51] Graf T, Felser C, Parkin SSP
Simple rules for the understanding of Heuler compounds
Prog Solid St Chem, **39** (2011), pp. 1-50

[52] Peatross J, Ware M,
Physics of Light and Optics
2015 Edition
http://optics.byu.edu/BYUOpticsBook_2015.pdf

[53] Guo LQ, Connelly MJ
A Muller-Matrix Formalism for Modeling Polarization Azimuth and Ellipticity Abgle in Semiconductor Optical amplifiers in a Pump-Probe Scheme
J. Lightwave Technol, **25** (2007), pp 410-420

[54] Šmíd D.
Lineární algebra pro fyziky.
http://www.karlin.mff.cuni.cz/ smid/

[55] Nývlt M.
Optical interactions in ultrathin magnetic film structures
Dimploma thesis, Charles university,
Pague, 1996

[56] Višňovksý Š.
Optics in Magnetic Multialyers and Nanostructures.
Taylor & Frencis Group,
Boca Raton, 2006
ISBN 0-8493-3686-4.

[57] Shreder EI, Svyazhin AD, Belozerova KA
Optical Properties of Heusler Alloys Co_2FeSi, Co_2FeAl, Co_2CrAl, and Co_2CrGa
Phys Met Metallog, **11** (2013), pp. 904-909

[58] Veis M, Beran L, Antos R, Legut D, Hamrle J, Pistora J, Sterwerf Ch, Meinert M, Shmalhorst JM, Kuschel T, Reiss G,
Magneto-optical spectroscopy of Co_2FeSi Heusler compound
J. Appl. Phys. **115**, 17A927 (2014)

[59] Veis M, Beran L, Zahradnik M, Antos R, Straka L, Kopecek J, Fekete L, Heczko O,
Magneto-optical spectroscopy of ferromagnetic shape-memory Ni-Mn-Ga alloy
J. Appl. Phys. **115**, 17A936 (2014)

[60] Beran L, Cejpek P, Kulda M, Antos R, Holy V, Veis M, Straka L, Heczko O
Optical and mangeto-optical studies of martensitic transformation in Ni-Mn-Ga magnetic shape memory alloys
J. Appl. Phys. **117**, 17A919 (2015)

[61] Lee SJ, Lee YP, Hyun YH, Kudryavtsev,
Magnetic, magneto-optical, and transport properties of ferroamgnetic shape-memory Ni_2MnGa alloy J Appl Phys **93**, 6975 (2003)

[62] Gan'shina E, Novikov A, Zykov G, Mettus D, Kazakov A, Kainuma R, Khovailo V, Prudnikov V, Granocsky A,
Magneto-optical spectroscopy of the martensitic transformation in $Fe48Mn24Ga28$ Heusler alloys
Phys Solid State **55**, 1866 (2013).

[63] Zhou Y, Jin X, Xu H, Kudryavtsev YV, Kee YP, Rhee JY,
Influence of structural transition of transport and optical properties of Ni_2MnGa alloy J. Appl. Phys. **91**, 9894 (2002)